RATE ANALYSIS OF THE θ_{13} NEUTRINO MIXING ANGLE FOR THE DAYA BAY REACTOR NEUTRINO EXPERIMENT

BY

SETH R. ELY

DISSERTATION

Submitted in partial fulfillment of the requirements
for the degree of Doctor of Philosophy in Physics
in the Graduate College of the
University of Illinois at Urbana-Champaign, 2013

Urbana, Illinois

Doctoral Committee:

Assistant Professor Mark Neubauer, Chair
Professor Jen-Chieh Peng, Director of Research
Professor Scott S. Willenbrock
Associate Professor Alfred Wilhelm Hubler

Abstract

We perform a rate analysis of the neutrino mixing angle θ_{13} for the Daya Bay Reactor Neutrino Experiment. The data were collected from December 24, 2011, to May 11, 2012, during a period of data acquisition when six antineutrino detectors were deployed. After accounting for backgrounds and detector efficiencies and comparing measured rates to those predicted, we estimate $\sin^2 2\theta_{13} = 0.0926 \pm 0.0109$.

To my grandparents.

Acknowledgments

This dissertation is not the one I would have liked to have written. One who has never run the gauntlet of graduate school supposes it to be an intellectual odyssey, a romantic vision of the most learned people in the world sitting around in coffee shops discussing the Fate of Man and the Meaning of the Universe. (I would have added to this description the wafts of smoke emanating from the pipes of graying professors in tweed jackets, but that caricature was before my time.) It is a monastic vision where all worldly concerns are sacrificed for the pursuit of Truth. In its structure, graduate school comes straight out of the guilds of the Middle Ages.

One might suppose even well into the graduate school experience that it all ends with a magnificent treatise overflowing with new additions to civilization's accumulated corpus of knowledge. A dissertation is taken to be the intellectual and even moral culmination to one's vow of poverty in pursuit of higher learning. But alas, the dissertation in practice is rarely novel and seldom read. It is certainly not a gift to Mankind, and I would hesitate a great deal even to call it a book. In the final analysis, the dissertation is really just The Final Lab Report.

Back in the days when I did not fully appreciate this point, I had an outline of many things that I thought I would include in my thesis. Some of them made it; most of them did not. I also had an outline for the preface, but it was lost. It is just as well. There is no point trying to make any grandiose statements, in moralizing, or trying to express some list of lessons learned. Even if anyone read them, I suppose the very fact that I spent eight and a half years in graduate school must diminish my credibility. I will get to the point, then,

which is to thank those who have contributed so much to my graduate school experience.

First, I must thank all of my fellow researchers in the Daya Bay Collaboration. One benefit of working on a large particle physics experiment is that one gets exposed to many aspects of science from the proposal of an experiment, to its design and construction, to the analysis of its data. Work is shared among many people, and the fate of the experiment does not rest on any single person. On the other hand, the researcher must forgo the independence and passion that comes with greater ownership of one's program of research. For better or worse, this thesis is an exposition of the pooled labors of many other researchers, and I cannot claim more than a sliver of contribution to an experiment that resulted in arguably the second-most important particle physics result in 2012 (after the discovery of the Higgs boson).

I must express my appreciation, not directed at anyone in particular, for the serendipitous benefits of graduate school. I have gotten to travel to China six times and spent about a year and a half there in total. I have developed a fondness for the people, the culture, the food, and the language, an interest that will not wane after the end of my time on the Daya Bay Experiment. Also, I have come to better understand my academic interests, to know my talents and limitations, and to discover new areas of intellectual pursuit. I am lucky that I am able to continue pursuing my relatively new interest in data science while parlaying it into a career.

I must thank my labmates: Mat Muether and Pinghan Chu, who made the office a friendly place for a new graduate student; Youcai Wang, with whom I shared many interesting conversations about economics and political philosophy (although I did more listening than speaking); and En-Chuan Huang, who listened patiently (if curiously) to the exhortations of this more senior graduate student to finish sooner rather than later. "The world can be your laboratory, and learning is a lifelong experience"—but I promised not to moralize. And of course, I must express my gratitude to Daniel Wah Kai Ngai, my coworker on Daya Bay. Our graduate careers ran nearly parallel trajectories. Among other things, he helped

me get settled when I was stationed in China. We would have hot pot at the Sichuan restaurant in Dapeng even in the middle of summer, an experience I would not mind repeating someday (although perhaps Stateside next time).

My greatest success in graduate school had little to do with the institution. It was not my research and certainly not the classes I took. What I gained of the greatest value were the friends I made there. I cannot even begin to enumerate them, and so I will name just a few: Mohammad Sahrapour, Jason Crnkovic, and Mike Bednarz. You guys transformed the way I feel about—well, nearly everything. You are brilliant, good, and honest people, and I don't know what more you could ask of a person. I am very blessed to have you as my friends. We must have had thousands of conversations about every area of human activity, working our way backwards from the normal progression of social development, starting with fiscal policy and quantum theory and aesthetics and eventually working our way up to more important conversations about relationships, the weird weather, and complaining about grad school.

My acknowledgements wouldn't be complete without a nod to all the teachers who have been a part of my education since my first day of Kindergarten more than 25 years ago. I will name only one: Mrs. Norman, my third grade teacher at Worthington Elementary School. I clearly remember reading Madeleine L'Engle's *A Wrinkle in Time* in her class. It was many times larger than any book I had read up until that time, but any trepidation was soon vanquished by Mrs. Norman's passion for literature and her confidence in us. I think my literary and scientific interests both spring in large part from that period, and I'm certain that reading that book was partly responsible for my pursuing a PhD in physics. Alas, I still cannot *tesseract*.

I thank my advisor, who set a prime example of scientific research and espoused a philosophy of independence in research that I appreciated, even if I could not always find opportunities to put it into practice. Prof. Peng's depth of knowledge in the field of particle physics is intimidating, but his patience and personality always encouraged one to ask more

and probe more deeply.

I must thank my family for their support over many years. Most of all, I want to thank my grandparents, to whom this dissertation is dedicated. Their influence pervades my very identity, and I could not be more fortunate than to have gotten the opportunity to be close to all of them. To my living grandfather and my three deceased grandparents, I hope I may do honor to your memory.

Table of Contents

Chapter 1

Theory

1.1 An Overview of Neutrino Physics

1.1.1 Highlights in the early history of neutrino physics

The birth of quantum mechanics was in many ways motivated by the discrete nature of certain physical processes, e.g. spectral lines due to quantized energy levels in the atom. This theory of the quantum extended to nuclear processes such as alpha and gamma decays. It was a surprise, then, when the electrons emitted from nuclear beta decay were observed to have a continuous energy spectrum. Since beta decay was assumed to be a binary decay, kinematics dictate that the outgoing electron should be monoenergetic. In fact, the outgoing electron (beta) was able to assume a range of energies.

The discovery of the continuous beta decay spectrum threatened to undermine one of the most fundamental laws of physics, conservation of energy. To spare the untarnished reputation of this principle, Wolfgang Pauli suggested in 1930 that a new particle, very light and electrically neutral, might be involved in the beta decay interaction. The hypothetical particle would share the nuclear decay energy with the electron and allow energy to be conserved on the whole. Pauli's proposed particle is, of course, what we now call the neutrino.

Following Pauli's idea, Enrico Fermi incorporated the neutrino in his theory of the weak interaction, a four-particle point interaction that mediates nuclear decays. Reasoning by analogy with quantum electrodynamics (QED), Fermi developed a theory of the weak interactions coupling two "weak currents". Fermi's theory is today regarded as a low-energy

limit of the broader class of electroweak interactions, described by the GSW model we shall discuss later.

With a successful theory depending on the neutrino's existence, it became important to conduct experiments to detect this elusive particle. Pauli himself at one time doubted that such a particle could ever be detected. Frederick Reines and Clyde Cowan set up liquid scintillator detectors near nuclear reactor at Hanford and later at Savannah River. They succeeded in detecting the neutrinos released in the fission process, confirming and publishing their discovery in 1956 [3]. The detection mechanism based on the inverse beta decay reaction, used by Reines and Cowan to detect the neutrinos, is essentially the same as that used at Daya Bay over 50 years later.

The possibility of parity nonconservation in the weak interaction had been explored on the theoretical side by C.N. Yang and T.D. Lee [4]. Just a year after the neutrino's discovery, C.S. Wu published evidence of parity violation in beta decay [5]. By using polarized ^{60}Co nuclei and measuring an isotropy in the emitted electrons, Wu showed conclusively that parity is not a symmetry of the weak force. This was the first time parity violation had been discovered in any area of physics.

In 1962 Lederman, Schwartz, and Steinberger used a beam of neutrinos coming from the decay of pions ($\pi^- \rightarrow \mu^- + \bar{\nu}$ and $\pi^+ \rightarrow \mu^+ + \nu$) to study the scattering of high-energy neutrinos with matter. They found that the neutrinos produced in association with muons had different properties than the neutrinos from beta decay. In particular, when they interacted, they produced more muons than expected [6]. The implication was that neutrinos came in two flavors, the electron neutrino ν_e and the muon neutrino ν_μ. Much later, after the τ lepton had been discovered, it too was found to be associated with a third neutrino flavor, ν_τ.

The existence of multiple neutrino flavors is a key ingredient in the study of neutrino oscillations. The Daya Bay experiment studies transitions between neutrino flavors. The other key ingredient is neutrino mass.

1.1.2 Theory of the electroweak interaction and neutrino mass

The theory of electroweak interactions illustrates many of the fundamental ideas underlying the Standard Model of particle physics. It would be out of place to delve into the full formalism of this theory here, but it is worth mentioning a few key ideas in its development.

The known elementary fermions form a set of left-handed doublets and right-handed singlets in three generations, as follows:

$$\left.\begin{array}{cccccc} \begin{pmatrix} u \\ d' \end{pmatrix}_L & & \begin{pmatrix} c \\ s' \end{pmatrix}_L & & \begin{pmatrix} t \\ b' \end{pmatrix}_L & \\ u_R & d_R & c_R & s_R & t_R & b_R \end{array}\right\} \text{quarks}$$

$$\left.\begin{array}{ccc} \begin{pmatrix} \nu_e \\ e \end{pmatrix}_L & \begin{pmatrix} \nu_\mu \\ \mu \end{pmatrix}_L & \begin{pmatrix} \nu_\tau \\ \tau \end{pmatrix}_L \\ e_R & \mu_R & \tau_R \end{array}\right\} \text{leptons}$$

along with the corresponding antiparticles. "Handedness" refers to the chirality of the particle spinors, which in the relativistic limit just corresponds to helicity ($\frac{1}{2}\sigma \cdot \hat{p}$). The Goldhaber experiment showed that neutrinos are found only with left-handed helicities (and hence antineutrinos with right-handed helicities) [7].

The modern electroweak theory unifies QED and flavordynamics (the theory of weak interactions) as consequences of certain symmetries. The Glashow-Weinberg-Salam (GWS) model of electroweak interactions is based on an $SU(2)_L \otimes U(1)$ symmetry. The $SU(2)_L$ (weak isospin) symmetry couples only the left-handed currents, while the $U(1)$ (hypercharge) symmetry connects currents of all chiralities. Proceeding as for the development of QED, the symmetry requirements can only be met if we introduce several new terms (gauge fields) into the Lagrangian. These fields are associated with the photon, $W^{\pm}$, and Z bosons. In fact, a notable success of the GWS model was its prediction of weak neutral currents before the experimental discovery of its mediator, the Z boson.

Masses arise in the theory through the introduction of another field, namely the Higgs boson. The underlying symmetry of the vacuum is said to be "spontaneously broken"; in other words, out of an infinity of equivalent ground states for the Higgs field, one of them is arbitrarily selected by nature. This permits the appearance in the Lagrangian of mass terms that would otherwise render the theory nonrenormalizable. As an aside, the announcement of the experimental discovery of the Higgs boson occurred just a few months after the release of Daya Bay's first results.

Since gauge theories do not predict particle masses, neutrino masses are appended to the Standard Model through a Yukawa term coupling a right-handed singlet state and a left-handed doublet with the Higgs field, resulting in Dirac masses of the form $-m\overline{\nu}\nu$. If there is no right-handed neutrino then the Dirac mass is zero. Alternatively we may consider Majorana mass terms of the form $-\frac{m}{2}\nu_L^T C\nu_L$, where C is the charge conjugation operator. To preserve the $U(1)$ symmetry, the Majorana particles must be neutral; therefore, the neutrino is the only lepton that can be Majorana. The tradeoff for using Majorana mass terms is that lepton number is no longer conserved.

Direct neutrino mass searches estimate the neutrino mass from the spectrum of beta decays. These experiments have so far succeeded only in setting upper bounds for the neutrino mass. Considerations from cosmology have also been used to set limits on the sum of the neutrino masses based on their impact to structure formation in the universe. The only positive indications that neutrinos are indeed massive particles presently come from oscillation experiments.

1.1.3 Neutrinos in other areas of physics

In addition to their impact on the formation of large-scale structure, neutrinos are important to cosmology in many other contexts. Neutrinos have been considered as candidates for dark matter, for example. Also, cosmic rays bombarding the earth's atmosphere regularly create

showers of short-lived particles that decay and give rise to atmospheric neutrinos. These are about two-thirds $\nu_\mu, \bar{\nu}_\mu$ and one-third $\nu_e, \bar{\nu}_e$. The charged interstellar protons and nuclei that comprise cosmic rays interact with the cosmic microwave background (CMB), a uniform photon background that limits the energies of charged interstellar particles. As the energy of these particles increases, so does its cross section for scattering off CMB photons. This energy loss mechanism suppresses the flux of high-energy particles, leading to a sort of cosmic speed limit called the GZK cutoff. High-energy neutrinos traveling from distant sources could on occasion interact locally to produce very high energy particles with energies above the GZK cutoff, thus explaining the results of some experiments observing unexpectedly energetic cosmic rays. Cosmological sources of neutrinos range from supernovae to active galactic nuclei, not to mention the as-yet unobserved cosmic neutrino background left over from the Big Bang. These relic neutrinos would provide a window to the earliest moments of the universe, even before the creation of the CMB.

Closer to home, the sun is another natural source of neutrinos. The study of solar neutrinos can help probe models of the sun. Geoneutrinos arise from radioactive decays within the earth itself. Nuclear reactors and neutrino beams are man-made neutrino sources. Fig. 1.1 shows that the man-made neutrino background is concentrated in few hot spots in the eastern U.S., Europe, and Japan.

A number of experiments involving neutrinos have given hints of some exotic physics, though so far the Standard Model has continued to prevail. The so-called GSI anomaly was an experimental result indicating a possible periodicity in the decay rates of highly ionized nuclei [8]. Neutrino mixing was put forward in attempt to explain this surprising result. Famously, the OPERA experiment briefly claimed to have measured superluminal velocities for neutrinos. This turned out to be a measurement error due to faulty cable connections. As the Standard Model becomes ever more established, it remains to be seen whether the neutrino sector will provide evidence of physics beyond the Standard Model, stimulating a new round of research and discovery, or whether our current understanding of the neutrino

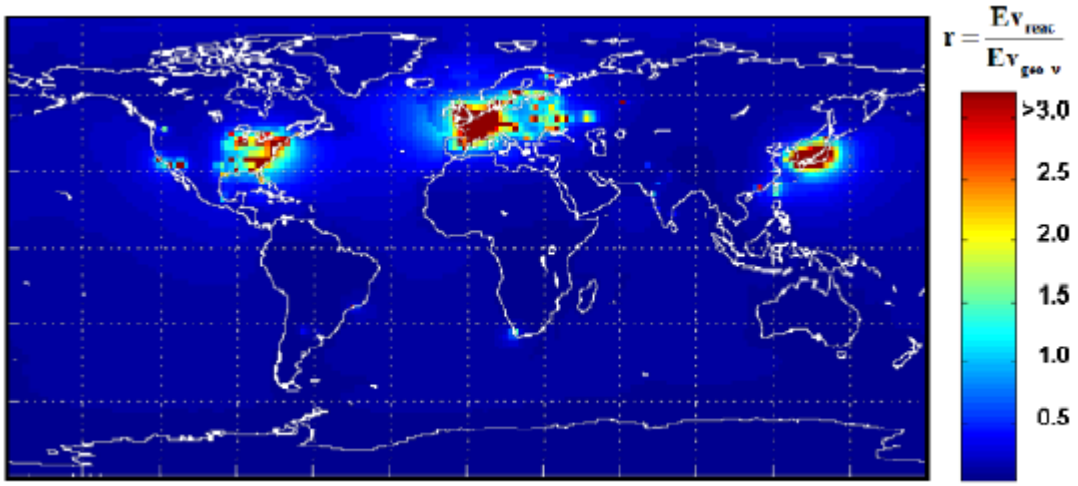

Figure 1.1: Ratio of reactor neutrino flux to geoneutrino background. (From a talk by the BOREXINO collaboration.)

will turn out to be, after all, correct.

1.2 Neutrino Oscillations

The neutrino has two parallel descriptions. On the one hand, a neutrino of given flavor is an eigenstate of the weak force Hamiltonian. On the other, the neutrino may be described in terms of its mass eigenstates, which are eigenstates of the free Hamiltonian. The interaction terms do not commute with the free Hamiltonian, and so these eigenstates are not in a one-to-one correspondence. Since the mass eigenstates travel at different velocities (for fixed energy), the neutrino flavor wavefunctions develop phase differences and the flavor composition is modified.

The neutrino mixing matrix (also called the PMNS matrix after Pontecorvo, Maki, Nak-

agawa, and Sakata) expresses the relationship between the mass states and the flavor states:

$$\begin{pmatrix} \nu_e \\ \nu_\mu \\ \nu_\tau \end{pmatrix} = \begin{pmatrix} U_{e1}^* & U_{e2}^* & U_{e3}^* \\ U_{\mu 1}^* & U_{\mu 2}^* & U_{\mu 3}^* \\ U_{\tau 1}^* & U_{\tau 2}^* & U_{\tau 3}^* \end{pmatrix} \begin{pmatrix} \nu_1 \\ \nu_2 \\ \nu_3 \end{pmatrix} \tag{1.1}$$

With $\nu^T = (\nu_e, \nu_\mu, \nu_\tau)$ and $\mu^T = (\nu_1, \nu_2, \nu_3)$ we write this more compactly as

$$\nu_\alpha = \sum_i U_{\alpha i}^* \mu_i \tag{1.2}$$

It is customary to use Greek indices for flavors and Roman indices for masses. More simply, we can write $\nu = U^* \mu$ or $\mu = U^T \nu$ since U is unitary. Throughout the following discussion we use the vector notation $a^\dagger b$ instead of the bra-ket notation $\langle a|b\rangle$, but integration over internal variables should be understood from the context. In this notation the PMNS matrix is just given by $U = \nu^* \mu^T$, due to the orthogonality of the neutrino wavefunctions.

The time evolution of mass states in their rest frame is achieved by multiplying the vector of mass eigenstates by

$$T^* = \mathrm{diag}(e^{-im_i \tau_i}) \tag{1.3}$$

so that

$$\nu^\tau = U^* \mu^\tau = U^* T^* \mu^0 = U^* T^* U^T \nu^0 \tag{1.4}$$

This expresses the flavor evolution starting with initial composition ν^0. The oscillation amplitude of transition from initial state ν_α^0 to final state ν_β^τ is $(\nu_\beta^\tau)^* \nu_\alpha^0$. (Again, integration is implicit.) In matrix form, that is

$$(\nu^\tau)^* (\nu^0)^T = U T U^\dagger \nu_0^* \nu_0^T = U T U^\dagger \tag{1.5}$$

where we have used $\nu_0^* \nu_0^T = I$, the identity matrix. This means that the probability of a

neutrino born in flavor α oscillating into a neutrino of flavor β is given by

$$p_{\alpha\beta}(\tau) = \left|\left[\nu^{\tau}(\nu^{0})^{\dagger}\right]_{\alpha\beta}\right|^{2} = \left|\left(UTU^{\dagger}\right)_{\alpha\beta}\right|^{2} = \left|\sum_{k} T_k U_{\alpha k} U^{*}_{\beta k}\right|^{2} = \sum_{k,l} T_k T^{*}_{l} U_{\alpha k} U^{*}_{\alpha l} U^{*}_{\beta k} U_{\beta l} \quad (1.6)$$

Now $|T_k|^2 = T_k T_k^* = 1$, so

$$p_{\alpha\beta}(\tau) = \sum_{k} |U_{\alpha k}|^2 |U_{\beta k}|^2 + \sum_{k\neq l} T_k T^{*}_{l} U_{\alpha k} U^{*}_{\alpha l} U^{*}_{\beta k} U_{\beta l} \quad (1.7)$$

From the unitary nature of U, we have $\sum_k U_{\alpha k} U^*_{\beta k} = \delta_{\alpha\beta}$. Using this relation, we observe

$$\begin{aligned} \delta_{\alpha\beta} &= \delta_{\alpha\beta}\delta^{*}_{\alpha\beta} \\ &= \sum_{k,l} U_{\alpha k} U^{*}_{\beta k} U^{*}_{\alpha l} U_{\beta l} \\ &= \sum_{k} |U_{\alpha k}|^2 |U_{\beta k}|^2 + \sum_{k\neq l} U_{\alpha k} U^{*}_{\beta k} U^{*}_{\alpha l} U_{\beta l} \end{aligned} \quad (1.8)$$

Combining Eqs. 1.7 and 1.8, we obtain

$$p_{\alpha\beta}(\tau) = \delta_{\alpha\beta} + \sum_{k\neq l} (T_k T^{*}_{l} - 1) U_{\alpha k} U^{*}_{\alpha l} U^{*}_{\beta k} U_{\beta l} \quad (1.9)$$

Observing that the sum in Eq. 1.9 consists of pairs of terms that are complex conjugates of each other (i.e. terms with l and k interchanged), we can write the manifestly real oscillation probability

$$p_{\alpha\beta}(\tau) = \delta_{\alpha\beta} + 2\sum_{k<l} \mathrm{Re}\left[(T_k T^{*}_{l} - 1) U_{\alpha k} U^{*}_{\alpha l} U^{*}_{\beta k} U_{\beta l}\right] \quad (1.10)$$

We now look at the time evolution component. For $m_i \ll p$, we have $E_i = \sqrt{m_i^2 + p^2} \approx p + m_i^2/2p$. Boosting to the lab frame, $\tau_i = \gamma t - \beta x = (E_i t - px)/m_i \approx m_i x/2p$, where in

the last step we have used $x = t$ since the neutrino is relativistic. It is easy to show that

$$T_k T_l^* = e^{i(m_k^2 - m_l^2)x/2p} \tag{1.11}$$

We typically use the notation $\Delta m_{kl}^2 = m_k^2 - m_l^2$ to represent the difference in the squared neutrino masses. Sometimes one sees the definition $\Delta m_{kl}^2 = |m_k^2 - m_l^2|$ since it is the magnitude and not the sign that is measured by many oscillation experiments. The distance x from the neutrino source to the point of detection is called the baseline.

In the text preceding Eq. 1.11 we took the neutrino mass states to have fixed momentum but different energies. In fact, had we made the reverse assumption, the oscillation probability would be the same since we take $E \approx p \gg m_\nu$. A more correct treatment incorporating the Heisenberg uncertainty relations takes the neutrino to be a wavepacket with distributed momentum, and once again the same oscillation probability is obtained [9, 10]. This is true even when the oscillation is deduced from a field theoretic treatment [11].

When $\alpha = \beta$, the oscillation probability takes the form $p_{\alpha\alpha} = 1 - (\cdot)$ and is said to be the ν_α *survival* probability. When $\alpha \neq \beta$, the expression is called a *appearance* probability. So far we have not discussed antineutrinos. The oscillation probabilities for antineutrinos are obtained using CPT invariance: $p(\bar{\nu}_\alpha \to \bar{\nu}_\beta) = p(\nu_\beta \to \nu_\alpha)$. However, if U is complex, it does not follow that $p(\bar{\nu}_\alpha \to \bar{\nu}_\beta) = p(\nu_\alpha \to \nu_\beta)$.

It is of interest to ask how many independent parameters are in the mixing matrix U. In general, an $n \times n$ unitary matrix has $n(n-1)$ independent parameters. (Start with $2n^2$ free parameters for a general complex matrix, subtract $n(n-1)$ due to column orthogonality, and then subtract $2n$ due to column normalization.) These independent parameters may be interpreted as $\frac{1}{2}n(n-1)$ real rotation angles and $\frac{1}{2}n(n-1)$ complex phases. This most general situation holds true if the neutrino is Majorana. However, if the neutrino is a Dirac particle, only $\frac{1}{2}(n-1)(n-2)$ phases are physical, for $(n-1)^2$ total parameters.

We now derive explicit formulae for a couple of important cases. Consider a two-neutrino

framework, where there is only a single real rotation angle. We may parametrize the matrix as

$$U = \begin{pmatrix} \cos\theta & \sin\theta \\ -\sin\theta & \cos\theta \end{pmatrix} \tag{1.12}$$

The oscillation probability becomes

$$\begin{aligned} p_{\alpha\beta} &= \delta_{\alpha\beta} \pm 2\left[1 - \cos\left(\frac{\Delta m^2 x}{2p}\right)\right]\sin^2\theta\cos^2\theta \\ &= \delta_{\alpha\beta} \pm \sin^2\left(\frac{\Delta m^2 x}{4p}\right)\sin^2 2\theta \end{aligned} \tag{1.13}$$

where we have put $\Delta m^2_{21} = \Delta m^2$ without ambiguity. The $-$ sign corresponds to the survival probability $\alpha = \beta$, and the $+$ sign corresponds to the appearance probability $\alpha \neq \beta$. Restoring factors of $\hbar$ and c, the survival probability can be written

$$\begin{aligned} p_{\text{sur}} &= 1 - \sin^2\left(\frac{\Delta m^2 x}{4p}\right)\sin^2 2\theta \\ &= 1 - \sin^2\left(\frac{1}{\hbar c}\,\frac{\text{eV}^2\,\text{m}}{\text{MeV}}\,\frac{\Delta m^2 x}{4p}\right)\sin^2 2\theta \\ &= 1 - \sin^2\left(1.26693\,\frac{\Delta m^2 x}{p}\right)\sin^2 2\theta \end{aligned} \tag{1.14}$$

where the units are clear from the second line. It is actually this two-neutrino formula that is commonly used in the analysis of neutrino oscillation experiments.

Since this is the first time we have calculated a physically observable quantity, it is worthwhile to make a couple of observations regarding Eq. 1.14. First, the magnitude of the oscillation is governed by the mixing angle θ. As θ approaches 45° the oscillation becomes maximal. Whether in fact one should infer from oscillation experiments a value of $2\theta \in [0, \frac{\pi}{2}]$ or $2\theta \in [\frac{\pi}{2}, \pi]$ is a question that seems to have tripped up many workers in the field. In the three-neutrino framework there are terms proportional to the first power of $\sin\theta$ and $\cos\theta$. However, the sign difference in these terms under $\theta \to \pi - \theta$ can be absorbed by the CP

phase, δ. For this reason it is conventional to take $\theta \leq \frac{\pi}{4}$. The other observation we wish to make is that neutrino oscillations depend on nonzero neutrino masses, or more precisely on a nonzero mass splitting. (Technically the observation of oscillation does not preclude the possibility that the lightest neutrino is massless.) This is why the first observation of oscillation at Super-Kamiokande implied physics beyond the Standard Model, although neutrino masses are a relatively minor addition to the theory.

The three-neutrino oscillation formulae are rather more complicated. With three angles and one phase (assuming Dirac neutrinos), the PMNS matrix is usually parametrized as

$$\begin{pmatrix} U_{e1} & U_{e2} & U_{e3} \\ U_{\mu 1} & U_{\mu 2} & U_{\mu 3} \\ U_{\tau 1} & U_{\tau 2} & U_{\tau 3} \end{pmatrix} =$$

$$\underbrace{\begin{pmatrix} 1 & 0 & 0 \\ 0 & \cos\theta_{23} & \sin\theta_{23} \\ 0 & -\sin\theta_{23} & \cos\theta_{23} \end{pmatrix}}_{\text{atmospheric}} \underbrace{\begin{pmatrix} \cos\theta_{13} & 0 & e^{-i\delta}\sin\theta_{13} \\ 0 & 1 & 0 \\ -e^{i\delta}\sin\theta_{13} & 0 & \cos\theta_{13} \end{pmatrix}}_{\text{reactor}} \underbrace{\begin{pmatrix} \cos\theta_{12} & \sin\theta_{12} & 0 \\ -\sin\theta_{12} & \cos\theta_{12} & 0 \\ 0 & 0 & 1 \end{pmatrix}}_{\text{solar}} \tag{1.15}$$

The labels "atmospheric", "reactor", and "solar" refer to the type of experiments that are generally sensitive to the given mixing angles. For example, the current limits on θ_{12} are largely determined by the results from the Sudbury Neutrino Observatory (SNO) measuring solar neutrino oscillation. The complex phase δ, called the CP phase, is responsible for potential CP violation in the oscillation pattern; i.e. differences in the probabilities $p(\nu_\alpha \to \nu_\beta)$ and $p(\bar{\nu}_\alpha \to \bar{\nu}_\beta) = p(\nu_\beta \to \nu_\alpha)$, assuming CPT invariance. The value has not been measured and has no effect on reactor neutrino disappearance experiments, which measure $p(\bar{\nu}_e \to \bar{\nu}_e)$.

The best present values of the mixing angles and mass splittings, as given by the Particle

Data Group [12], are

$$\sin^2 2\theta_{12} = 0.861^{+0.026}_{-0.022}$$

$$\sin^2 2\theta_{23} > 0.92$$

$$\Delta m^2_{21} = (7.59 \pm 0.21) \times 10^{-5}\ \text{eV}^2$$

$$|\Delta m^2_{32}| = (2.43 \pm 0.13) \times 10^{-3}\ \text{eV}^2$$

At the inception of the Daya Bay experiment, θ_{13} remained the only undetermined mixing angle. Unlike the other angles, the reactor mixing angle is small, with the CHOOZ experiment setting a 90%-C.L. upper bound of $\sin^2 2\theta_{13} < 0.15$.

The unknown sign of Δm^2_{32} leaves open two possibilities for the mass ordering: $m_1 \approx m_2 \ll m_3$ (normal hierarchy) or $m_3 \ll m_1 \approx m_2$ (inverted hierarchy). This is illustrated in Fig. 1.2. The true mass hierarchy is unknown, but future long-baseline accelerator experiments may be able to resolve this ambiguity.

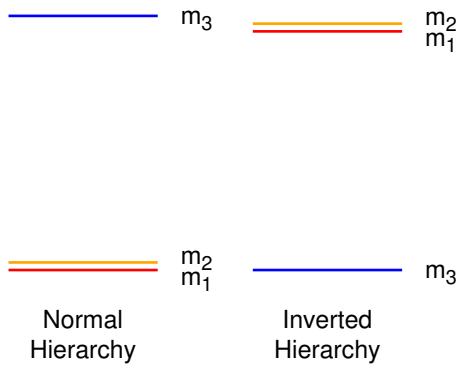

Figure 1.2: Experimental data are consistent with two possible orderings for the neutrino masses. Mass *differences* are shown to scale.

We note that the particular parametrization above is not unique. One can consider different permutations of the rotation matrices with the CP phase appropriately applied to

the central matrix [13]. This leads to different mixing angles; of the six possibilities, three have small θ_{13} and three have large θ_{13}. This just reminds us that the physical quantities are not the mixing angles, but rather the PMNS matrix elements.

Working out the survival probability for the electron neutrino, we obtain

$$\begin{aligned} p_{ee} =& 2s_{12}^2 c_{12}^2 c_{13}^4 \cos\Delta_{21} + 2c_{12}^2 s_{13}^2 c_{13}^2 \cos\Delta_{31} + 2s_{12}^2 s_{13}^2 c_{13}^2 \cos\Delta_{32} \\ & - 2c_{12}^2 s_{13}^2 c_{13}^2 - 2s_{12}^2 s_{13}^2 c_{13}^2 - 2s_{12}^2 c_{12}^2 c_{13}^4 + 1 \end{aligned} \tag{1.16}$$

where $s_{ij}(c_{ij}) = \sin(\cos)\theta_{ij}$ and $\Delta_{ij} = \Delta m_{ij}^2/2p$. Using several trigonometric identities, one can obtain the simplified survival probability

$$p_{ee} = 1 - c_{13}^4 \sin^2\frac{\Delta_{21}}{2}\sin^2 2\theta_{12} - c_{12}^2 \sin^2\frac{\Delta_{31}}{2}\sin^2 2\theta_{13} - s_{12}^2 \sin^2\frac{\Delta_{32}}{2}\sin^2 2\theta_{13} \tag{1.17}$$

Since it is known that $|\Delta m_{21}^2| \ll |\Delta m_{32}^2|$, we may take $\Delta m_{31}^2 \approx \Delta m_{32}^2$, and the expression simplifies to:

$$p_{ee} \approx 1 - c_{13}^4 \sin^2\frac{\Delta_{21}}{2}\sin^2 2\theta_{12} - \sin^2\frac{\Delta_{32}}{2}\sin^2 2\theta_{13} \tag{1.18}$$

At short baselines (i.e. $\Delta m_{12}^2 x/E_\nu \ll 1$) the second term on the right is negligible, and the oscillation is approximated by the two-neutrino formula

$$p_{ee} \approx 1 - \sin^2\left(1.27\,\Delta m_{32}^2\,\frac{x}{p}\right)\sin^2 2\theta_{13} \tag{1.19}$$

The exact oscillation probabilities for ν_e transitions are plotted in Fig. 1.3.

At small baselines the oscillation probability is determined by Δm_{32}^2. At longer distances (or lower energies), the term modulated by the solar mixing angle begins to play an important role. Since a realistic neutrino source is not monoenergetic, the value of x/p is actually distributed with some width. By a simple back-of-the-envelope calculation one can show that the phase difference between neutrinos of momentum p and neutrinos of momentum

$p + \delta$ causes destructive interference when

$$x\left(1 - \frac{p}{p+\delta}\right) = \frac{\lambda}{2} \tag{1.20}$$

where $\lambda \propto 2\pi p/\Delta m^2$ is the oscillation wavelength. When $\delta \ll p$, this condition shows that the oscillation pattern becomes washed out at a distance of about $x = \lambda p/2\delta$. This is illustrated in Fig. 1.4. Characteristic oscillation wavelengths for reactor neutrinos with $p \approx 4$ MeV are $\lambda_{\text{solar}} = 261$ km and $\lambda_{\text{reactor}} = 8.2$ km.

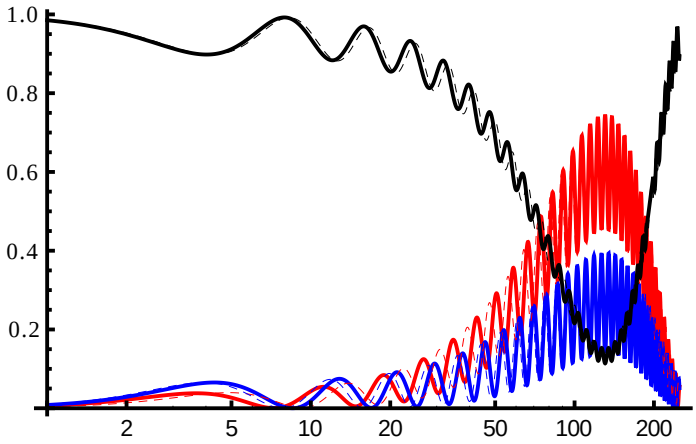

Figure 1.3: Oscillation probability for p_{ee} survival (black), $p_{e\mu}$ appearance (red), and $p_{e\tau}$ appearance (blue) as a function of baseline (in kilometers). The thick solid curves correspond to the normal mass hierarchy, while the dashed curves correspond to an inverted hierarchy. We have set $\delta_{CP} = 0$. The neutrino energy is fixed at 4 MeV.

Up to this point we have considered vacuum oscillations, i.e. neutrinos oscillation with no environmental influence. Wolfenstein [14] showed that $\nu_e, \bar{\nu}_e$ scattering of electrons in matter could modify the oscillation wavelengths. This effect is particularly important in the study of solar neutrinos, where the neutrinos have a large path length within the sun's interior. This is why the sign of the Δm^2_{12} mass splitting is known. Due to the short path length of neutrinos through matter at Daya Bay, the MSW effect is not important for this experiment.

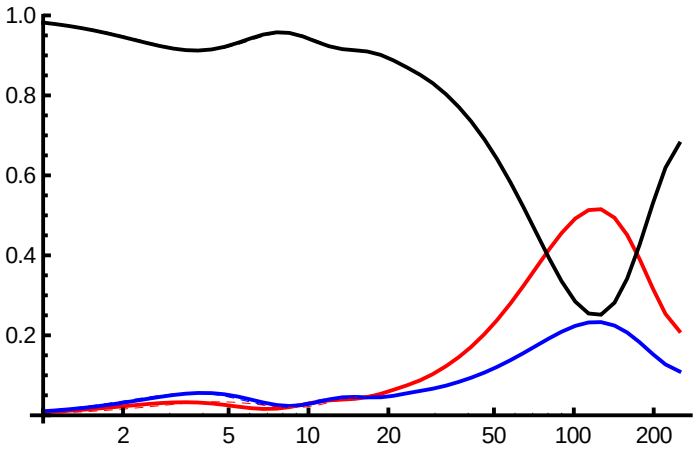

Figure 1.4: Oscillation probability versus baseline (in km) when the neutrino energy is normally distributed; i.e. $E_\nu \sim N(4\text{ MeV}, 1\text{ MeV})$. See Fig. 1.3 and the main text for details.

We have assumed in our discussion that the neutrinos are born with the same energy. It is equally possible to assume that the neutrinos have equal momentum, or better yet, to treat the neutrino as a wave packet. In all cases the resulting oscillation expression is the same. We also note that a number of neutrino experiments (NuTeV and LSND, to name a couple) have observed neutrino disappearance that cannot be reconciled with simple three-neutrino oscillations. Of course, this may be due to an incomplete understanding of the systematic errors in those experiments, but these anomalies have suggested that there may exist sterile neutrinos, i.e. neutrinos that do not interact according to any of the forces in the Standard Model. The simplest example of such a sterile neutrino is a right-handed neutrino that does not couple to the weak force. Such a 3+1 scheme (or schemes with multiple sterile neutrinos) would create additional oscillation channels. Fits to data yield large mass splittings on the order of ~ 20 eV^2, suggesting that the sterile neutrino would be much heavier than the three known neutrinos. The so-called "see-saw mechanism" right-handed neutrino that is heavier still, along with a light left-handed neutrino. The see-saw mechanism assumes the neutrino is Majorana.

1.3 A Short History of Neutrino Mixing

Long before mixing was observed in the neutrino sector, it was observed in the quark sector that the currents in the weak interaction do not couple the (left-handed) strong eigenstates u with d and s, for example, but rather u couples to some linear combination $d' = d\cos\theta_c + s\sin\theta_c$ and $s' = -d\sin\theta_c + s\cos\theta_c$, where θ_c is the Cabibbo angle. Extending this mixing to three generations of quarks, the translation from the weak eigenstates to the strong eigenstates is formalized in the Cabibbo–Kobayashi–Maskawa (CKM) matrix. A comparison of the relative textures of the PMNS and CKM matrices is shown in Fig. 1.5.

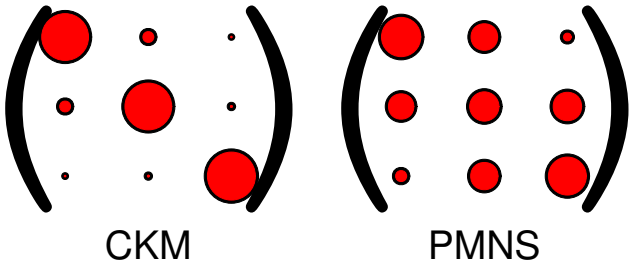

Figure 1.5: Graphical illustration of the magnitude of the CKM matrix elements and the PMNS matrix elements. The quark mixing matrix is largely diagonal, while mixing in the neutrino sector is more pronounced.

Mixing phenomena were first observed in the study of neutral kaons. The K^0 and the $\overline{K}^0$ are strong eigenstates with quark content $d\bar{s}$ and $s\bar{d}$, which mix with one another as they evolve in time. Such mixing has also been observed in $B^0 - \overline{B}^0$ and $D^0 - \overline{D}^0$ systems.

Neutrino oscillation was put forward by Bruno Pontecorvo as mixing between the neutrino and the antineutrino, but the same formalism is used today to describe flavor mixing, as in the quark sector. The history of oscillation measurements must mention Davis' Homestake Experiment, which was the first to detect neutrinos from the sun, and in the process identified a rate deficit that came to be known as the solar neutrino problem. Decades later the Super-Kamiokande experiment, whose detector was sensitive to neutrino directionality, detected an assymetry in the flux of atmospheric neutrinos that they attributed to flavor oscillations.

Further evidence for neutrino oscillations came from the Sudbury Neutrino Observatory, which showed that oscillations were indeed the explanation for the solar neutrino deficit.

Since these experiments (and others) have measured the solar and atmospheric mixing angles, the reactor mixing angle θ_{13} naturally became a focus of interest. The CHOOZ collaboration in France, until recently, had set only an upper bound on the size of the mixing angle. This situation changed rapidly in late 2011 and early 2012 as several experiments began to produce positive results. T2K, an accelerator experiment in Japan that had been damaged by the Tohoku Earthquake, analyzed the fraction of the data they had been able to obtain and found a nonzero θ_{13} at 2.5σ significance. Their 90% confidence interval put $\sin^2 2\theta_{13}$ between 0.03 and 0.28 assuming a normal mass hierarchy [15]. Later, the Double CHOOZ collaboration came out with their results, placing $\sin^2 2\theta_{13}$ in (0.017,0.16) at 90% C.L. In 2012, Daya Bay and RENO released their own first results. All evidence now points toward nonzero θ_{13}.

Since the flurry of activity as T2K, Double CHOOZ, Daya Bay, and RENO announced first results, phenomenologists have been busy working out the implications of nonzero θ_{13}. A systematic study of 76 group symmetries undertaken by Wingerter and Parratu [16] found that 44 could accomodate the experimental mixing angles following T2K at the 3σ level. Alternatively, anarchy models assume that the neutrino mixing matrix is random. With the oscillation angles now known, attention is beginning to turn to the remaining parameter in the mixing matrix, δ_{CP}. Precise knowledge of θ_{13} will help to optimize the design of these experiments.

Chapter 2

Experiment

2.1 Overview of the Experiment

The Daya Bay experiment was conceived for the singular purpose of measuring the last unknown neutrino mixing angle, θ_{13}. Following the null results of the CHOOZ collaboration, several proposed experiments vied to be the first to measure this input to the Standard Model. When the ill-fated experiment at Braidwood in the United States did not come to pass (due in part to environmental concerns related to a tritium leak at the Braidwood Generating Station), many U.S. and Chinese scientists joined together to propose the experiment at Daya Bay, a precision measurement with a design sensitivity of
$\sin^2 2\theta_{13} = 0.01$. Today, the Daya Bay Collaboration collaboration consists of over 200 researchers from insitutions in the US, China, Hong Kong, Taiwan, the Czech Republic, and Russia. There are individuals within the collaboration also hail from Armenia, Ecuador, Germany, Great Britain, Japan, Mexico, Spain, and other countries, making it truly a global collaboration.

The Daya Bay nuclear power complex is situated at 22.6° N, 114.5°E in an inlet of the South China Sea. It provides a substantial fraction of Hong Kong's electricity needs, but the reactors are located on the Chinese mainland in the Shenzhen Special Economic Zone. Although the power plant is just 40 km from either of these thriving metropolises, the site is relatively rural, on the coast of the Dàpéng (大鵬) Peninsula. The mountainous topography of the site conveniently enables large detector overburdens with horizontal tunneling; there is no need to drill down or construct artificial overburdens for the detectors. The rock

surrounding the Daya Bay detectors is primarily sandstone, granite, and hornfels. Bore-hole samples have been taken and analyzed for chemical composition and mechanical properties. The rock density ranges from 2.3 to 2.7 g/cm^3 [47].

The six currently operational reactors (more are planned) of the Daya Bay nuclear power station are arranged in three pairs that we will call "Daya Bay", "Ling Ao", and "Ling Ao II". In the final configuration eight antineutrino detectors will be divided among three sites. Two detectors will be near the Daya Bay cores (the "Daya Bay near site" or "Engineering Hall 1/EH1"), two will be midway between the Ling Ao and Ling Ao II cores (the "Ling Ao near site" or "EH2"), and four will be at a longer distance from all cores (the "far site" or "EH3"). Tunnels in the mountain connect the three detector sites. For the period of data collection we will discuss, six detectors were deployed in a 2-1-3 configuration as shown in Fig. 2.1. The final two detectors will be deployed in the summer of 2012.

The following salient features of the Daya Bay Experiment were employed to obtain its nominal sensitivity (and funding):

1. *Large target mass.* While CHOOZ used a single five-ton detector, Daya Bay employs eight 20-ton detector modules, with a far site target mass of $4 \times 20 = 80$ metric tons. The target mass is proportional to the number of neutrinos an experiment is able to observe, and hence a larger target implies better statistics.

2. *High reactor power.* At CHOOZ, the nuclear reactors had a combined thermal power output of 8.5 GWth (thermal gigawatts). This is the raw energy output before conversion to electricity. At Daya Bay there are six reactor cores each producing 2.9 GWth, for a total power of 17.4 GWth. Thus the neutrino flux is about twice as large at Daya Bay.

3. *Optimized baseline.* When the earlier CHOOZ experiment was being designed, the Δm^2_{23} mass splitting was not well known, and so a baseline of about 1 km was used in that experiment. Improved knowledge of this parameter allowed Daya Bay to situate

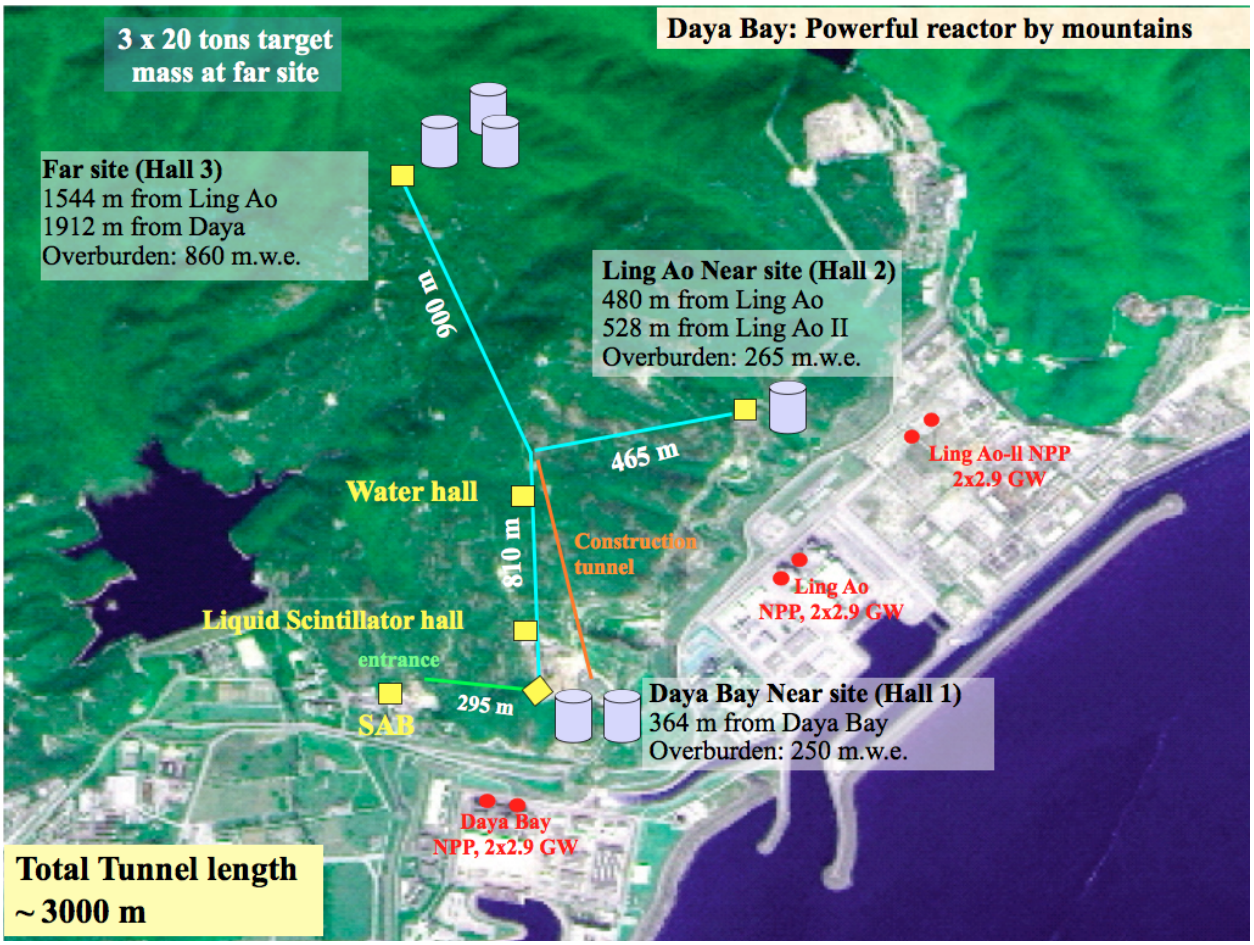

Figure 2.1: Configuration of the current deployment of Daya Bay detectors. Six detectors are distributed among three sites. The reactor core pairs are shown as red dots. In addition to the three detector sites are the liquid scintillator hall where detectors are filled with liquid scintillator and a central water processing hall. The Surface Assembly Building (SAB) is the site of above-ground construction and assembly.

its detectors nearer the first oscillation minimum, increasing the sensitivity of the measurement by studying the effect of oscillation where it is greatest.

4. *Nearly identical detectors.* Multiple detectors allow for a relative measurement, as discussed below, and additionally help control any systematic errors related to the detection efficiency. The neutrino detector modules are constructed so as to be "nearly identical", meaning that many of the detector-related uncertainties will cancel in a rate-only analysis because they are highly correlated. However, in a typical shape analysis, i.e. an oscillation analysis incorporating the measured energy spectrum of the neutrinos, these detector-correlated errors can be magnified [17].

5. *Relative measurement.* CHOOZ was an *absolute* measurement in the sense that their measurement of θ_{13} depended upon an estimate of the absolute reactor flux. This was necessary since they had only a single detector. Daya Bay's use of multiple detector modules allows for a *relative* measurement by comparing the flux at multiple baselines. This reduces any systematic uncertainty in the expected neutrino rate due to the limitations of the specific reactor model.

6. *Large overburden.* In neutrino experiments, downward-going muons produced by cosmic ray particles bombarding the atmosphere are the greatest single source of background noise. The muons themselves generate Čerenkov and scintillation light, and in addition they produce many secondary particles. This is less important at the Daya Bay near site, where the neutrino flux is relatively high, but at the far site, where precise counting of the neutrino events really matters, it is crucial to minimize the muon flux. Other experiments often create an artificial overburden (basically a pile of dirt) over the detector site, but at Daya Bay the far detectors are actually placed in the interior of a small mountain that shields the far site detectors from cosmic-ray-induced backgrounds by 880 m.w.e. (meters of water equivalent) of rock.

7. *Detector swapping.* The modularity of the detectors was also intended to allow them to be shuffled from site to site in several intervals of data collection. This would further reduce the systematic uncertainties associated with the detectors. In practice, it remains to be determined whether detector swapping will be employed.

The baselines of the six currently deployed detectors were obtained by a GPS survey and are presented in Table 3.12. Of course the detectors and reactors are extended objects whose location is only approximated by a point. A study of this "finite size effect" estimated a reduction of the neutrino flux on the order of $\sim 10^{-5}$ and concluded that the error in assuming point sources and detection at a point is negligible [48]. It is in this sense that the baseline uncertainty of a few centimeters is meaningful.

	DB1	DB2	LA1	LA2	LA3	LA4
AD1	362.4	371.8	903.5	817.2	1353.6	1265.3
AD2	357.9	368.4	903.4	816.9	1354.2	1265.9
AD3	1332.5	1358.1	467.6	489.6	557.6	499.2
AD4	1919.6	1894.3	1533.2	1533.6	1551.4	1524.9
AD5	1917.5	1892.0	1534.9	1535.0	1554.8	1528.0
AD6	1925.3	1899.9	1538.9	1539.5	1556.3	1530.1

Table 2.1: Baselines of all detectors from all reactor cores to the nearest tenth of a meter [40]. The uncertainty is estimated to be 2.8 cm.

2.2 The Neutrino Signal

2.2.1 Beta Decay

The term beta decay usualy refers to nuclear decays in which a neutron decomposes into a proton and an electron ($n \rightarrow p + e^- + \overline{\nu}_e$). The electron and positron were historically called the β^- and β^+. A semiclassical derivation of the e^- β-decay spectrum starts with the

density of states for the outgoing electron and neutrino:

$$D(p_e, p_{\overline{\nu}_e})\, dp_e dp_{\overline{\nu}_e} \propto 4\pi p_e^2 dp_e \times 4\pi p_{\overline{\nu}_e}^2 dp_{\overline{\nu}_e} \tag{2.1}$$

The proton recoil is neglected because of the relatively high nucleon mass. Letting $Q = T_e + T_{\overline{\nu}_e}$ be the kinetic energy shared between the final particles and assuming that the neutrino is massless, we have $p_{\overline{\nu}_e} = T_{\overline{\nu}_e} = Q - T_e$. With the relativistic energy-momentum relation $p_e^2 = (T_e + m_e)^2 - m_e^2$, we see that the outgoing momenta are both functions of T_e. The change of variable $p_{\overline{\nu}_e} \to T_e$ is trivial, and the Jacobian for the change $p_e \to T_e$ is just

$$J = \frac{T_e + m}{p_e} \tag{2.2}$$

In terms of the kinetic energy of the electron, the density of state is just proportional to

$$D(T_e)\, dT_e \propto p_e(T_e)^2\, p_{\overline{\nu}_e}(T_e)^2\, J\, dT_e = \sqrt{T_e^2 + 2T_e m_e}(T_e + m_e)(Q - T_e)^2\, dT_e \tag{2.3}$$

This is the beta spectrum at lowest order, which extends from $T_e = 0$ to $T_e = m_n - m_p - m_e$. Higher-order corrections account for the proton recoil, the nuclear matrix element incorporating information about nuclear structure, the Fermi factor accounting for the Coulomb interaction between the escaping electron and the daughter nucleus, and the finite mass of the neutrino.

Measurements of the shape of the beta spectrum near its endpoint ($T_e \to Q$) have been used to set the upper limits of the neutrino mass. Since we previously treated the neutrino as massless, we should in this limit include a correction factor of $\sqrt{1 - m_\nu^2/(Q - T_e)^2}$ to the shape of the beta spectrum [18]. This decreases the amount of energy available to the electron and brings down the endpoint of the spectrum. The smallness of the neutrino mass means that the effect of the correction term is only discernible far into the tail of the distribution (see Fig. 2.2), and so experiments using beta decay to measure the neutrino

mass require very high statistics in order to make any positive measurement. As described in the previous chapter, the electron antineutrino is actually a superposition of mass states, and so the quantity being measured in tritrium beta decay experiments, for example, is actually $m_{\nu_e} = |U_{1e}|^2 m_1 + |U_{2e}|^2 m_2 + |U_{3e}|^2 m_3$.

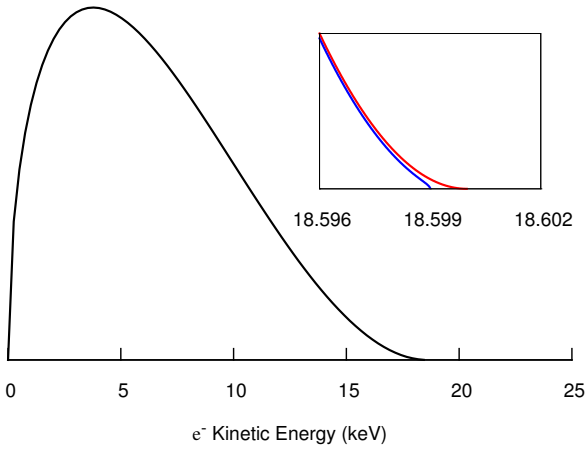

Figure 2.2: Shape of the beta decay spectrum with Q=18.6 keV (approximate endpoint of tritium beta decay). Inset shows a comparison of the spectrum with (blue) and without (red) consideration of the neutrino mass, assuming $m_\nu = 1$ eV.

2.2.2 Inverse Beta Decay and the Coincidence Signature

Inverse beta decay (IBD) is neutrino capture on a proton: $\overline{\nu}_e + p \rightarrow e^+ + n$. Conservation of energy gives $E_{\overline{\nu}} = E_{e^+} + E_n - m_p$ in the lab frame, in which the proton is at rest. Because the neutron is much heavier than the positron, we again neglect its recoil energy. To a good approximation the positron carries away all of the available energy, which is the incoming neutrino energy minus the nucleon mass difference: $E_{e^+} = E_{\overline{\nu}} - (m_n - m_p) = E_{\overline{\nu}} - 1.29$ MeV. Thus we may reconstruct the neutrino energy spectrum by measuring the energy of the outgoing positron, which is essential for shape tests of neutrino oscillation. The threshold

for this reaction to occur, i.e. the minimum neutrino energy, is $m_n - m_p + m_e = 1.804$ MeV.

The final state positron may directly annihilate with an electron or first form a short-lived positronium state. The precise fraction of positrons forming para-positronium (spin-singlet state) versus ortho-positronium (spin-triplet state), as well as the lifetimes of these states, depends on the specific chemical environment. *p*-Positronium has a lifetime of only 125 ps, while *o*-positronium has a mean life of 140 ns in vacuum and about 3 ns in liquid scintillator [19]. *p*-Ps and *o*-Ps decay into two and three photons, respectively. The visible energy is the total energy measured by a detector. It is the total (rest + kinetic) energy of the positron plus the energy due to electron annihilation: $E_{\text{vis}} = E_{e^+} + m_e = E_{\overline{\nu}} - 0.78$ MeV.

The final state neutron of the IBD reaction typically reaches thermal equilibrium with its environment before it is captured on a nucleus. A neutron scattering off carbon requires on average about ∼125 collisions to thermalize, a number which increases with the mass of the target. Thermalization and capture in the target zone of the Daya Bay antineutrino detectors occurs on a timescale of tens of microseconds. In the target region of the Daya Bay antineutrino detectors neutron capture occurs primarily on hydrogen and gadolinium. Capture on hydrogen releases 2.22 MeV of energy (the binding energy of the deuteron). This low-energy signal is obscured by many other low-energy backgrounds. At higher energy, Gd-captured neutrons are the focus of our analysis. To estimate the energy of capture on gadolinium, we use the data in Table 2.2. The mean mass of the six stable isotopes of gadolinium, weighted by their natural abundances, is 157.26 u. The cross sections are given at room temperature, corresponding to 2200 m/s neutrons. With this we obtain an average energy of 8.047 MeV, mostly due to capture on ^{155}Gd and ^{157}Gd.

Prompt positron energy loss and annihilation followed by a delayed neutron capture is the signature by which we identify the inverse beta decay signal. This two-fold coincidence allows rejection of most backgrounds, which occur singly and uncorrelated in time. Though the probability of two random triggers occurring in a very short time interval is quite small, such accidental coincidences form an important systematic background that must be accounted

Isotope	Abundance	Cross Section (b) [20]	Contribution	Q (MeV)
^{154}Gd	0.0218	85	3.737×10^{-5}	6.435
^{155}Gd	0.1480	61100	1.824×10^{-1}	8.536
^{156}Gd	0.2047	1.5	6.193×10^{-6}	6.360
^{157}Gd	0.1565	259000	8.176×10^{-1}	7.937
^{158}Gd	0.2484	2.2	1.102×10^{-5}	5.943
^{160}Gd	0.2186	0.77	3.395×10^{-6}	5.635

Table 2.2: The six stable isotopes of gadolinium and their relative importance for neutron capture. The weighted average Q-value is 8.047 MeV.

for in the data analysis. Once a coincidence has been identified, the energy of the prompt signal can be used to reconstruct the neutrino spectrum.

Cross Section of Inverse Beta Decay

At tree level, inverse beta decay is simply a charged current interaction between an incoming antineutrino and an up quark in the proton. The Feynman diagram for this process is shown in Fig. 2.3. The total cross section at this order is given by [21]:

$$\sigma(E_{e^+}) = (9.52 \times 10^{-44}\ \mathrm{cm}^2) \left(\frac{E_{e^+} p_{e^+}}{\mathrm{MeV}^2} \right) \tag{2.4}$$

where the positron energy is measured in the lab frame. Vogel and Beacom extended the calculation of the cross section to include corrections for weak magnetism and nuclear recoil. A plot of the zeroth-order cross section obtained from this formula is shown in Fig. 2.4.

We now illustrate the calculation of the tree-level differential IBD cross section. The usual expression [22] in the lab frame is

$$\frac{d\sigma}{d\cos\theta} = \frac{G^2 \cos^2\theta_C}{2\pi} E_e p_e \left[(g_V^2 + 3g_A^2) + (g_V^2 - g_A^2) v_e \cos\theta \right] \tag{2.5}$$

where G is the Fermi coupling constant, θ_C is the Cabibbo angle, and $g_{V,A}$ are the vector

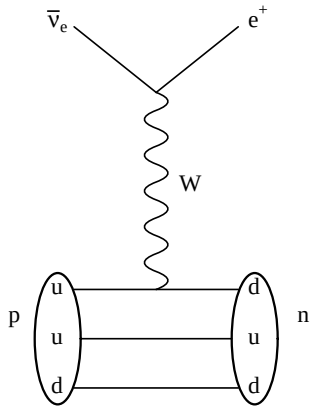

Figure 2.3: Feynman diagram for inverse beta decay.

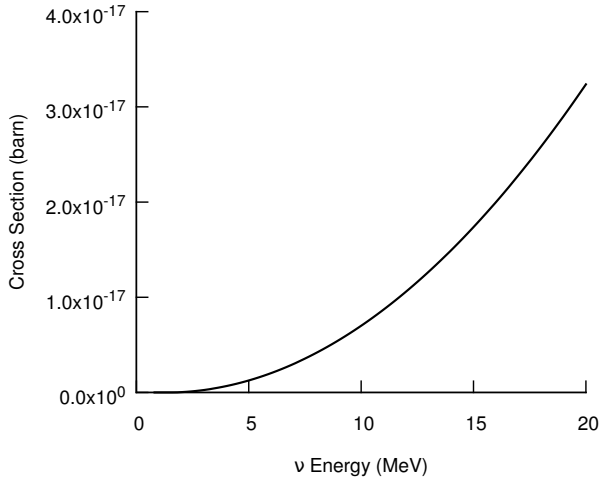

Figure 2.4: Total cross section (at lowest order) for inverse beta decay using Vogel and Beacom's formula.

and axial-vector form factors. E_e, p_e, and v_e are the energy, momentum, and velocity of the outgoing positron. Although succinct, this description is a bit incomplete since the electron energy and momentum are both completely determined once the neutrino energy and scattering angle have been specified.

We begin with the amplitude

$$\mathcal{M} = \frac{G\cos\theta_C}{\sqrt{2}}\left[\bar{v}_\nu\gamma^\mu(1-\gamma^5)v_e\right]\left[\bar{u}_n\gamma_\mu(g_V - g_A\gamma^5)u_p\right] \tag{2.6}$$

Since the energy transfer is small compared to the W mass, we neglect the propagator. Working out the traces,

$$|\mathcal{M}|^2 = \frac{G^2\cos^2\theta_C}{2}\Big\{64(g_V^2+g_A^2)\left[(p_e\cdot p_p)(p_\nu\cdot p_n)+(p_\nu\cdot p_p)(p_e\cdot p_n)\right]+64m_pm_n(g_A^2-g_V^2)(p_e\cdot p_\nu)\Big\} \tag{2.7}$$

which may be expressed in terms of the neutrino energy E_ν and the angle θ between the incoming neutrino and the outgoing positron. In principle the differential cross section is now determined, given in the CM frame by:

$$\frac{d\sigma}{d\cos\theta} = \frac{1}{32\pi}\frac{1}{s}\frac{|\mathbf{p}_e|}{E_\nu}|\mathcal{M}|^2 \tag{2.8}$$

where $s = (p_\nu + p_p)^2$ is the invariant Mandelstam variable.

To be explicit, let us work out the kinematics. We boost to the lab frame in which the proton is at rest with

$$\beta = \frac{E_\nu}{\sqrt{E_\nu^2 + m_p^2}} \tag{2.9}$$

Solving $E'_\nu = \gamma(1-\beta)E_\nu$ for E_ν gives the relationship between the energies of the neutrino

in the two frames:

$$E_\nu = \frac{E'_\nu \sqrt{m_p}}{\sqrt{2E'_\nu + m_p}} \tag{2.10}$$

At first order in E_ν/m_p, the scattering angle is

$$\begin{aligned} \theta' &= \theta - \frac{(2M\Delta - m_e^2)\sin\theta}{\sqrt{(\Delta^2 - m_e^2)(4M^2 - m_e^2)}} \left(\frac{E_\nu}{m_p}\right) + O\left(\frac{E_\nu}{m_p}\right)^2 \\ &\approx \theta - 1.09 \left(\frac{E_\nu}{m_p}\right) \sin\theta \end{aligned} \tag{2.11}$$

where $M = \frac{1}{2}(m_p + m_n)$ and $\Delta = m_n - m_p$. See Fig. 2.5. For our purposes, we are interested in E'_ν much less than m_p, and so we can take $\theta = \theta'$.

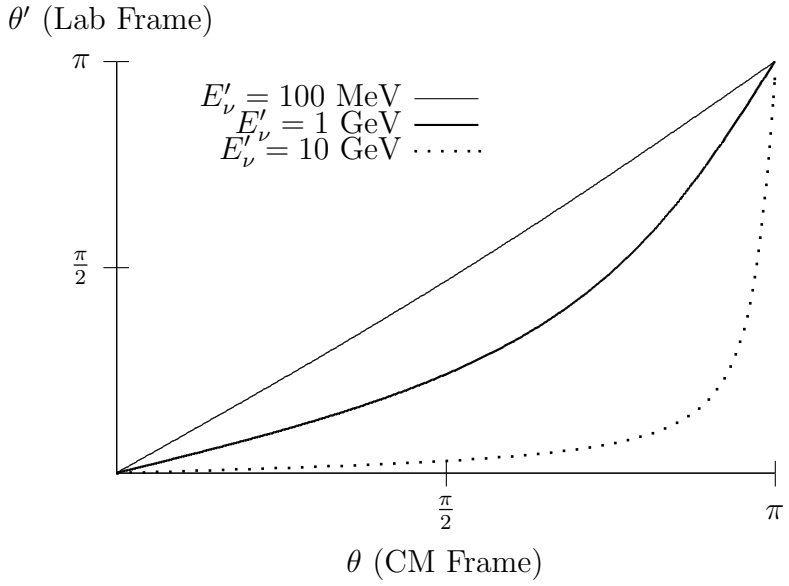

Figure 2.5: Scattering angle in the CM frame versus the lab frame.

Starting with Eq. 2.7 and Eq. 2.8, putting in the kinematic information, plugging in numerical values for all physical constants, and retaining second-order terms in E'_ν/M, we

obtain an approximation for the lab-frame cross section:

$$\frac{d\sigma}{d\cos\theta'} = \left(1.42022 \times 10^{-19}\right)\Big[\left(1 - 1.69278E'_\nu + 0.649358{E'}_\nu^2\right) + \left(-0.0930614 + 0.170828E'_\nu - 0.0665638{E'}_\nu^2\right)\cos\theta' + \left(5.56064 \times 10^{-7}E'_\nu - 1.53111 \times 10^{-6}{E'}_\nu^2\right)\cos^2\theta'\Big] \quad (2.12)$$

where the neutrino energy is in MeV and the cross section is in barns. We have taken $g_V = 1$ and $g_A = 1.26$. This approximation is very close to the "exact" tree-level result, which does not truncate higher order terms in E'_ν/M (see Fig. 2.6). However, the approximation has a root at 1.69 MeV instead of at the correct threshold value of $E^{\text{thr}} = \Delta + m_e = 1.80$ MeV.

A polar plot of the differential cross section is shown for several values of the neutrino energy in Fig. 2.7 and a measure of the forward-backward asymmetry is shown in Fig. 2.8. Just above threshold the positron direction is isotropic. As the neutrino energy is increased toward 4 MeV, the positrons become increasingly backscattered. Above this value, the relative fraction of forward scattered positrons increases. At 119.3 MeV the asymmetry begins to exceed unity, meaning that the positrons are primarily forward scattered.

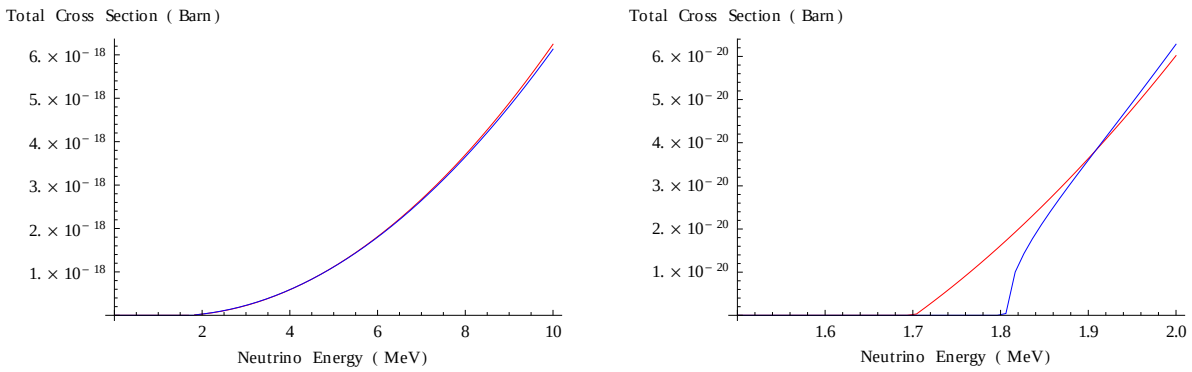

Figure 2.6: Total cross section in the lab frame. Blue is the exact result (the only approximation being $\theta = \theta'$); red is the approximation of Eq. 2.12. In the right-hand plot the approximation is shown to be nonzero below threshold.

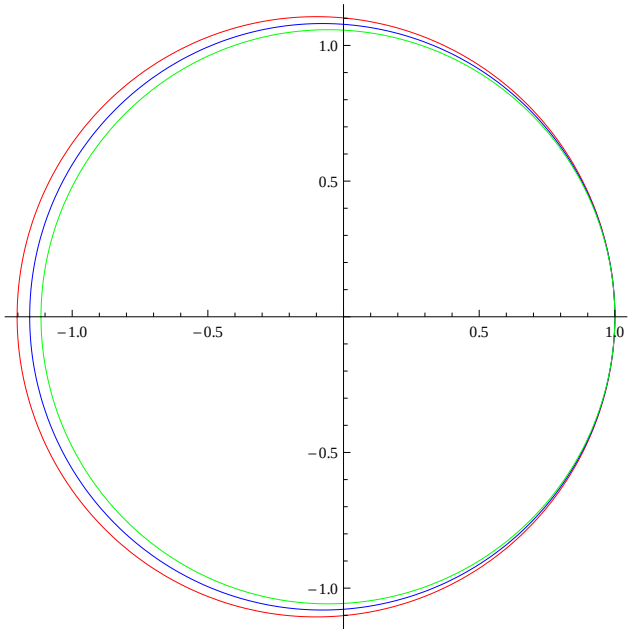

Figure 2.7: Polar plot of the differential cross section in the lab frame for three different neutrino energies: $E'_\nu = 10$ MeV (red), $E'_\nu = 30$ MeV (blue), $E'_\nu = 50$ MeV (green).

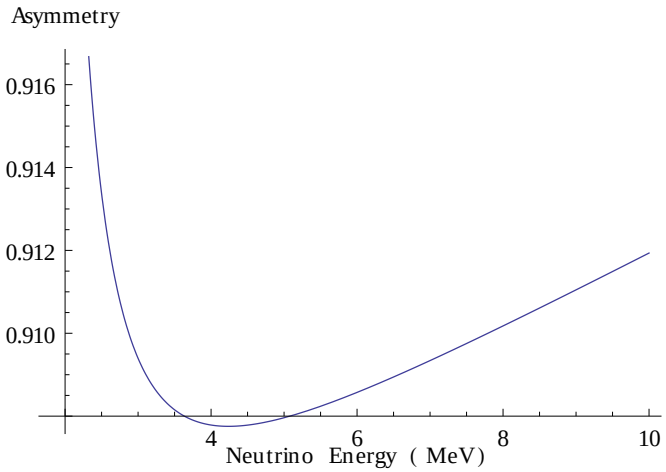

Figure 2.8: Ratio of forward-scattered positrons to backward-scattered positrons versus neutrino energy in the lab frame.

2.3 Reactor Neutrino Flux

Construction of the Daya Bay nuclear power complex began in 1987, before the handover of Hong Kong. As a result, the administrative and ownership structure of the plant is a study in international corporate law. The reactor core design was developed by Framatome (now Areva), a largely state-owned French conglomerate. The 900 MWe pressurized water reactors were built in pairs over a span of several decades, with increasing Chinese participation in each new pair of reactors. Today, only a small French support staff remains at the Daya Bay nuclear power station.

Although the Daya Bay experiment is a relative measurement, the type of analysis performed usually relies on some estimate of the reactor flux. Much effort is devoted to calculating the expected neutrino rates as a function of time. We illustrate the basic idea with a simple calculation, but a complete modeling of the reactor cycle is a full-time profession in itself.

The major fissile isotopes responsible for the core power output are ^{235}U, ^{238}U, ^{239}Pu, and ^{241}Pu. The reactor neutrino spectra for all but ^{238}U were measured at the Institut Laue–Langevin (ILL) several decades ago and are typically taken as inputs into reactor flux calculations. ^{238}U is stable and fissions only when bombarded with fast neutrons; therefore the neutrino spectrum from this isotope must be calculated from models. If x_i is the fraction of the ith isotope, P is the reactor power, and e_i is the mean energy released per fission of the ith isotope, the fission rate of the ith isotope is

$$f_i = x_i P \Big/ \sum_k x_k e_k$$

If s_{ij} is the neutrino spectrum of the jth isotope (i.e. the mean number of neutrinos in the

Isotope	e_i (MeV)
^{235}U	201.92 ± 0.46
^{238}U	205.52 ± 0.96
^{239}Pu	209.99 ± 0.60
^{241}Pu	213.60 ± 0.65

Table 2.3: Average fission energy for isotopes common in nuclear fuel [41].

ith energy bin released per fission), then summing over isotopes gives

$$n_i = \sum_j s_{ij} f_j = \frac{\sum_j x_j s_{ij}}{\sum_k x_k e_k} P$$

The mean fission energy per decay of each of these isotopes is given in Table 2.3. As time passes, the isotopic composition of the fuel changes. The fluctuating power level of a reactor and the time-dependent effects (e.g. burnup), illustrated in Fig. 2.9, mean that the neutrino flux changes with time.

Using a simple model for the reactor fuel composition and preliminary baselines, the initially expected neutrino count rates at Daya Bay, as reported in the TDR, are given in Table 2.4. The effects of oscillation are not considered in the prediction. Given the static fuel composition assumption and the limitations of the model used in this preliminary calculation, it is perhaps not a surprise that the estimates are considerably different than the measured rates.

For the actual Daya Bay analysis, a group of Chinese collaborators known as the Reactor Working Group, who have some access to restricted information provided by the power plant, provides a weekly estimate of the neutrino flux at each reactor. The power plant uses sophisticated models to simulate burnup, incorporating the actual structure of the fuel assembly so that they can simulate neutrino transport within the core.

Recent calculations of reactor spectra suggest that the reactor neutrino flux is several percent higher than previously believed [23]. These studies use improved models but still

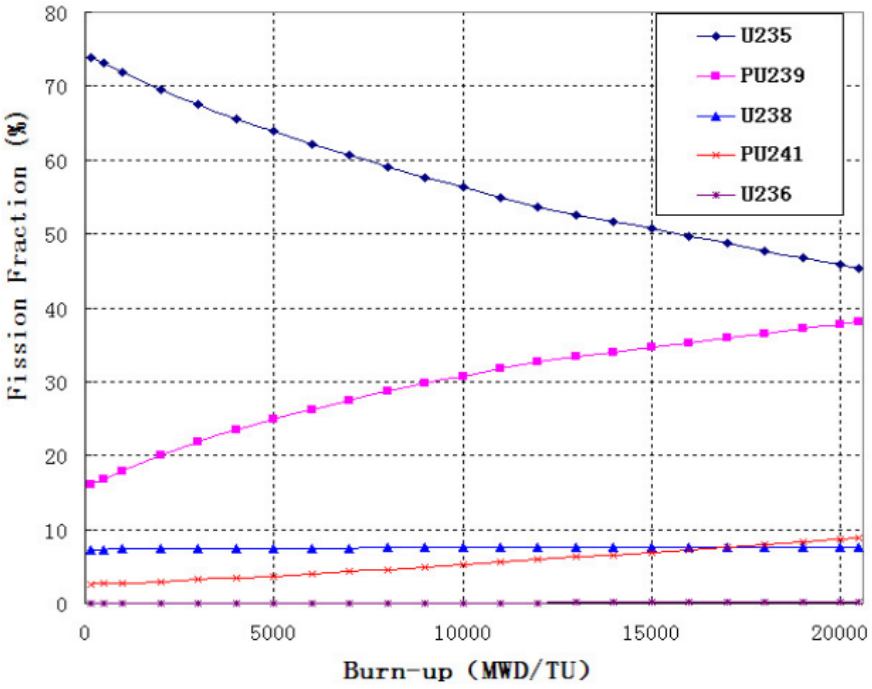

Figure 2.9: Change in fuel composition for typical reactor cycle [41].

rely on the old ILL data. The implication of this work, if true, is that the rate deficits observed in reactor neutrino experiments are larger than claimed, providing some evidence for a massive sterile neutrino. This "reactor anomaly" has been widely reported, but the new flux calculations are not used in the analyses of any experiments to date.

The uncertainty in the expected neutrino rate can be traced back to various reactor-related uncertainties. These include the precise knowledge of the core position (negligible) and the various correlated and uncorrelated uncertainties in the flux model, such as the neutrino spectrum of each fission isotope. Power fluctuations from core to core are generally uncorrelated, as are the varying fuel compositions among the reactors. Another important source of neutrinos comes from the spent nuclear fuel stored on site near the reactors. This waste continues to undergo fission and is therefore a source of some neutrino background

Site	Expected	Measured
Daya Bay near	930	716
Ling Ao near	760	532
Far	90	71

Table 2.4: Neutrino rates (per module per day) at each of the detector sites [1].

even when the reactors are off.

2.4 Liquid Scintillator

2.4.1 Specification and Production

The use of liquid scintillators for neutrino detection has a long history dating back to the discovery of the neutrino. The CHOOZ and Palo Verde experiments both used gadolinium-doped liquid scintillator in oscillation experiments. Stability of the scintillator was a concern for these experiments. Palo Verde used a 0.1% (wt) Gd solution with an attenuation length of 3-4 meters. This dropped by about 1 mm/day. The light yield in the Palo Verde configuration was 0.76 photoelectrons per MeV per photomultiplier tube [24]. CHOOZ used a 0.09% Gd solution with 0.65 photoelectrons per MeV per photomultiplier tube. Their scintillator famously degraded over time, eventually ending the experiment. The degradation was attributed in part to the presence of nitrate ions left over from the scintillator production process [25].

Gadolinium doping improves detector performance in several ways. The thermal neutron cross section of gadolinium is large, increasing neutron capture efficiency and reducing the capture time (which ultimately lowers the accidental rate by allowing a smaller Δt requirement). Also, neutron capture on gadolinium releases an 8-MeV gamma cascade that is well above radioactive backgrounds.

In choosing a liquid scintillator Daya Bay sought a formula with long attenuation length, high light yield, long term stability, and chemical compatibility with the materials with which it will come into contact, such as the acrylic vessels. The Daya Bay proposal required a light yield of at least 100 photoelectrons per MeV (0.52 per phototube), and simulations showed that this specification demanded an attenuation length of at least four meters [49]. A minimum attenuation length of 10 m for light in the region 350-450 nm was preferable, as it would increase the detector uniformity [50].

The Daya Bay scintillator base is linear alkyl benzene (LAB). LAB, with chemical formula $C_6H_5C_nH_{2n+1}$ (n=10-13), is an organic liquid scintillator with 10% free protons by weight. It is a colorless, odorless liquid with a flash point of 130 °C used in the manufacture of biodegradable detergents. To this is added 2,5-diphenyloxazole (PPO) as a primary fluor and 1,4-bis[2-methylstyryl]benzene (bis-MSB) as a wavelength shifter. The LAB itself has a density of 0.8589 g/ml. The liquid scintillator mixture with PPO and bis-MSB has a density of 0.8592 g/ml. The gadolinium-doped liquid scintillator has a density of 0.8609 g/ml [51].

Because it is hard to dissolve inorganic gadolinium salts in aromatic scintillator solvents, it is first necessary to complex the gadolinium with an organic ligand. Numerous complexing agents were studied, and many of these were not viable choices because they tended to precipitate. The most promising ligands studied were carboxylic acids, with the added benefit that the final gadolinium complex could be washed with water to remove impurities and neutralize any remaining acid that might otherwise make it into the liquid scintillator. The solid product, a white powder, could also be stored and transported easily.

Production of the dry scintillator complex began by dissolving $GdCl_3$ in water at low pH (2.70). Separately, the complexing agent 3,5,5-trimethylhexanoic acid (TMHA) was neutralized with ammonia to produce TMHA-NH_4OH at pH 6.85. This was combined with the Gd solution while stirring, and a solid complex formed at the interface of the two phases. The water was drained and the solid washed twice with deionized water. Next, LAB was pumped in to dissolve the solid. The mixture was filtered, and time was allowed for any

remaining water to separate from the organic phase. The bis-MSB and PPO, which were purified through melting, filtration, distillation, and recrystallization, were then mixed with the LAB solution [52]. This mixture was diluted to 0.1% Gd by weight [52, 53].

Throughout this process it was important that the mixing equipment be very clean. In one dry run the attenuation length of the scintillator dropped from 10.5 m to 8.2 m in just one month because the raw materials had not been purified [54]. Iron coming from the joint of the stirrer and motor was found to make its way into the final Gd product, increasing the absorption of the scintillator [55]. The final scintillator product had to be filtered to remove small particles that might reduce the attenuation length.

Another major concern was the possible presence of radioimpurities in our scintillator. Based on a specified singles rate of < 50 Hz, Daya Bay demanded ^{238}U, ^{232}Th, and ^{40}K levels below 10^{-13} (wt) [1]. The concentration of ^{232}Th was measured to be 10 ppb $GdCl_3$ [54]. This contaminant decays into another background source, ^{228}Ra, and so we required the final concentration of thorium to be less than 4 ppb. Fortunately, in the production process gadolinium "scavenges" the thorium, basically displacing it so that after filtration almost 100% of the thorium is removed. Scavenging also removes more than 90% of the iron impurities discussed above. However, more than 70% of the initial concentration of radium remained in solution even after adding gadolinium. Chemical analysis has shown that this impurity does not make it into the final product [56]. We also must deal with the presence of radon, causing an expected coincidence rate of 2.35×10^{-8} Hz. Radon can enter the liquid scintillator from exposure to air during mixing or during storage by permeating the plastic storage bags. To keep the correlated background rate below 0.1% we require the radon level to be less than 6.35×10^9 atoms/ton [57].

The final gadolinium concentration can be measured by weighing or by X-ray scattering. A year after commissioning, the first two ADs still showed that the gadolinium remained uniformly distributed in the detectors to a level better than 1% [58]. The attenuation of both the doped and undoped liquid scintillator is measured to be about 20 m. A slow decrease in

scintillator	τ_0 (ns)	τ_1 (ns)	ω
undoped LS	4.04	16.35	0.88
Gd LS	4.37	17.37	0.83

Table 2.5: Decay time constants for the liquid scintillator.

the attenuation length has been observed in all detectors, with a time constant around six to eight years [59]. Two 5-megapixel CCD cameras at the top and bottom of the AD are used to monitor filling, confirm positions of the sources during calibration, conduct any necessary inspections of the AD interior, and detect any significant changes in optical quality [60]. Other instrumentation provides redundant monitoring of optical clarity.

2.4.2 Scintillation Mechanism

Scintillators are extensively used in particle physics to detect the passage of charged particles. These particles excite atomic electrons in the scintillating medium. With lifetimes on the order of tens of nanoseconds, the electrons then relax back into lower energy states, releasing photons. Organic liquid scintillators are chosen so that the wavelength of the emitted light is matched to the responsivity curve of the light detector, usually a photomultiplier.

The Daya Bay liquid scintillator has two characteristic decay times, and so the scintillation follows a law of the following form:

$$\frac{\omega}{\tau_0} e^{-t/\tau_0} + \frac{1-\omega}{\tau_1} e^{-t/\tau_1}$$

Using a ^{22}Na source coupled to a plastic scintillator the decay rates and relative contributions have been measured for the Gd-doped liquid scintillator as well as the undoped LS (see Table 2.5).

Different scintillators also experience variable degrees of quenching, the conversion of a particle's energy to other degrees of freedom that are not detected as light. The effect is

modeled empirically by Birk's Law, which expresses the distribution of light along a particle's path. If $a = \frac{dE}{dx}$ is the energy lost per unit path length by the charged particle, then Birk's Law states

$$\frac{dL}{dx} \propto \frac{a}{1 + k_B a}$$

where $\frac{dL}{dx}$ is the light yield per unit path length and k_B, called Birk's constant, is a property of the material. This nonlinearity of light yield (i.e. light is not proportional to deposited energy) may be important in vertex reconstruction, for example.

2.5 Antineutrino Detectors

2.5.1 Design

At Daya Bay we employ eight antineutrino detectors (ADs) distributed over three sites to measure the neutrino flux at different baselines. A 1/3-scale prototype detector was developed and studied by the IHEP group to inform many design decisions [26]. The ADs are required to meet certain design principles common to many other experiments, summarized below [61].

1. *High statistics.* A large target mass is preferred to increase the neutrino rate.

2. *High signal-to-noise ratio.* Gadolinium-doped liquid scintillator has a clean neutron capture signal well above radioactive backgrounds.

3. *Identical detectors.* Precise, redudant relative measurements between near and far detectors allows for better control of detector-related uncertainties.

4. *Well-determined target mass.* A precise mass measurement further reduces the detector-related uncertainty.

5. *Low e^+ threshold.* Low single γ rate.

6. *Well-determined neutron detection efficiency.* Use of γ catcher, identical detectors, and energy calibration allow the neutron efficiency to be measured precisely.

7. *Good energy resolution.* Use of high-yield scintillator with long attenuation length and large geometric coverage of the detector by PMTs allow for precise energy measurement.

8. *Detector swapping.* Large 6-m tunnels and detector modularity permit this option.

The Daya Bay detectors are distinct from those used in past neutrino experiments in that they are modular nested cylinders with three zones. We discuss each of these factors in turn.

Modular. Historically, neutrino experiments have employed a monolithic detector at a single baseline, though in some experiments the detector was moveable. At Daya Bay, eight antineutrino detector (AD) modules are used. This is driven partly by the desire to do a near-far measurement. However, there are other good reasons to use modular detectors. First, the detectors are easier to manufacture, with greater overall consistency of design. Second, smaller detectors are easier to lift and transport. They can be partially assembled above ground in the Surface Assembly Building (SAB) and then moved underground for final installation and deployment. In addition, ease of transport leaves available the option of swapping detectors in the future to get a further handle on systematics. A third reason for multiple detectors is that they provide cross checks on systematic errors. Multiple measurements of each systematic at a given site allow better understanding of AD performance. Finally, several smaller detectors are easier to access and modify than a single large detector [62].

Cylindrical. Given that the physical detection mechanism is the same across experiments, there is considerable variation in detector shape from one experiment to another, from

KamLAND's "balloon" to CHOOZ's "geode". At Daya Bay, each AD module is a set of three nested concentric cylinders. The outer tank is constructed of stainless steel, while the inner volumes are made from transparent acrylic. A cyclindrical shape was chosen based on Monte Carlo studies showing that the energy and position resolution of a cylinder is better than that of a sphere [1]. This result seems more anecdotal than factual, however, and it seems that the design was at least in part driven by the necessity of transporting the ADs through the access tunnels when swapping detectors was still likely to be an important feature of the experiment. The shape was also justified on the argument that a cylindrical detector is faster and easier to build than other shapes [63].

Three Zones. The Daya Bay detector is in many ways based on the CHOOZ design. The three-zone feature is a prominent example of this. While a two-zone detector is easier and less expensive to build, the addition of the central gamma-catcher zone decreases the uncertainty in the neutron detection efficiciency. At the sacrifice of some target volume, a three-zone detector increases confidence in the systematic uncertainties [61].

The innermost zone, the target volume consisting of Gd-doped liquid scintillator, is contained by an acrylic vessel 3.1 m in diameter, 3.1 m in height. With a GdLS density of 0.855-0.870 g/mL, the target mass is in the range 20-20.3 T.

The second, central, zone is filled with undoped liquid scintillator and contained by a 4.0-m acrylic vessel. With no capture on Gd occurring in this zone, it does not contribute to the measured neutrino rate, but it helps prevent the loss of light for IBD events occuring near the boundary of the target volume. This gamma-catcher, as it is called, thus increases the efficiency of neutron detection and hence the overall IBD efficiency. The choice to employ a gamma catcher reflects a compromise of statistics in favor of reduced uncertainties.

The outermost region of the ADs, called the buffer zone, shields the scintillating regions of the detector from external radiation, but its primary purpose is to shield the PMTs from each other. Radioactive elements in the PMT glass mean that the PMTs can themselves

be sources of backgrounds. This layer is 0.488 m thick and filled with optically transparent mineral oil. The simulated response to a 1-MeV electron as a function of r^2 for a detector without the buffer region is shown in Fig. 2.10. The blue line is 15 cm from the PMT photocathodes, showing that this much buffer is required to maintain detector uniformity.

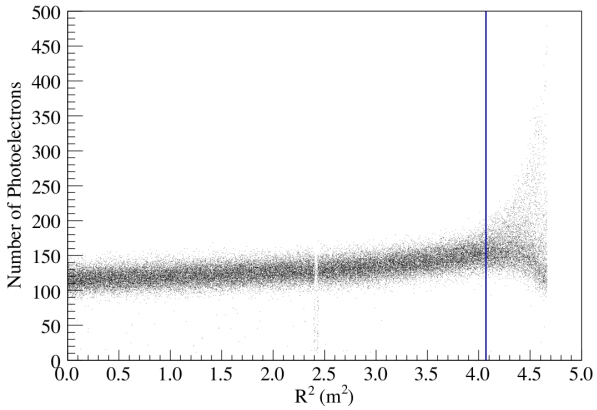

Figure 2.10: Simulated response of a modified detector to a 1-MeV electron [1].

The specified dimensions of the ADs are summarized in Table 2.6. After construction the ADs were surveyed to obtain their actual dimensions. One of the AD modules was found to have a significantly larger target volume (the height of the inner vessel was large by several cm), but this is readily taken into account in the analysis.

We briefly mention two effects that must be regarded in calculating the IBD efficiency. First is the spill-out effect, by which the neutron from IBD events occurring in the target volume leak out of the central zone. Such neutrons cannot be captured on gadolinium, and so even the presence of the gamma catcher does not eliminate this inefficiency. The second effect is spill-in, whereby IBD neutrons created in outer zones diffuse into the target zone. This contributes to the measured IBD signal, even though the associated events occur outside of the target volume. With no fiducial cuts employed in the Daya Bay analysis, these

Region	Inner Radius	Outer Radius	Inner Height	Outer Height	Container Thickness	Material
Target	-	155.0 cm	-	310.0 cm	10.0 mm	Gd-LS
γ-catcher	156.0 cm	198.5 cm	312.0 cm	397.0 cm	15.0 mm	LS
Buffer	200.0 cm	248.8 cm	400.0 cm	497.6 cm	12.0 mm	Mineral oil

Table 2.6: Dimensions of the antineutrino detectors [1].

effects must be carefully studied and their contributions to the overall IBD rate precisely estimated.

2.5.2 Components

A good experimentalist may well find the technical details of an experiment as interesting as the physics goal itself. (The author once heard an hourlong meeting with excited participants discussing the relative merits of teflon versus polyethylene cable jackets.) A good writer, on the other hand, should not bore the reader with too many of these details, and so we quickly summarize the assembly of the AD in the remainder of this section and only briefly discuss the design and construction of the water pool in the next section. It must be noted that in spite of our short treatment, this kind of work is at the heart of experimental particle physics and has earned many a graduate student his or her PhD.

In addition to physics requirements, the ADs must also satisfy a number of chemical and engineering specifications. Clearly low radioactivity is demanded from all construction elements, as well as chemical compatibility of all components with any fluids they might contact. The mechanical integrity of the detector is especially important during periods of least stability, viz. moving and filling. Using finite element analysis, the collaboration has carefully studied the stresses and strains on the detector during these periods to inform the

transportation and filling procedures. Finally, the ADs and indeed the entire experimental setup must meet various safety and environmental regulations by the funding agencies, the Chinese government, and the power plant.

Stainless steel tank. The stainless steel vessel (SSV) is 5 m in diameter and 5 m in height, manufactured of low radioactivity 304L stainless steel and weighing about 24T. The vessel has several ports where signal, power supply, and other instrumentation cables may be passed into the AD. The inner surface of the SSV is painted with a black fluorocarbon paint [64].

Acrylic vessels. The acrylic vessels must be designed in such a way as to allow the automated deployment of calibration sources, and they must be strong enough to withstand stresses and strains arising from transportation, filling, and thermal expansion of the liquids [1]. The acrylic used for the 3- and 4-m vessels has been chosen to avoid UV damage from the sun during transportation to the experimental site. (Some acrylics show degradation in optical properties with only a few hours exposure to sunlight [65].) The density of acrylic samples from all vendors was found to be about 1.19 g/cm^3 [66]. The vessels are constructed in sections and joined with a UV-transparent adhesive. Simulations show that these bonds have no effect on the light yield [67]. Increasing the thickness of the acrylic from 10 mm to 25 mm has been shown in simulations to decrease the neutron detection efficiency by 2%, and the uncertainty in this efficiency rises from 2.5% to 3.2% [68].

PMT ladders. Eight ladder-type structures are used to mount the PMTs. The ladders are cleaned and PMTs are mounted before each segment is installed in the AD. Guide rails ensure that the ladders are aligned and secure during installation [69]. The error in the PMT positioning is expected to be within 5.5 mm vertically, 5.5 mm radially, and 5.0 mm circumferentially [70].

Ribs and support structure. Various supporting structures are part of the AD design in order to ensure the mechanical stability of the assembled detector.

Radial shield. The presence of PMT mounts, support structures, numerous cables, etc., which break the cylindrical symmetry of the detector, led to concerns about the position uniformity of the ADs. To address these issues, a black radial shield consisting of 32 black frosted acrylic panels surrounds the AD. Prior to installation the panels were shown to be compatible with mineral oil and not a significant source of radioactive backgrounds [71].

Reflecting panels. In constrast to the black sides, the top and bottom of the AD are covered with reflective panels. Diffuse reflection on the top and bottom of the detector doubles the light yield and improves energy resolution [72]. The panels consist of a reflective film sandwiched between two 1-cm thick acrylic discs. They are positioned just above and just below the 4-m acrylic vessel, with three holes in the top reflector for calibration PMTs [73].

Lid. The lid of each AD houses the Automated Calibration Unit (ACU), which contains calibration sources, motors, and all the facilitating hardware. Several pipes allow the radioactive and LED sources to be deployed into the tanks. Liquid depth sensors, temperature monitors, and even an inclinometer are also mounted to the lid. At one site the detectors have actually showed a gradual increase in tilt, though not sufficiently pronounced to endanger the experiment. Three overflow tanks with a capacity of 100-150 L allow for thermal expansion of the liquids up to 6-8 °C or possible overfilling in any of the three zones without danger of the liquids from separate zones mixing [74]. It is expected that the central overflow tubes will contain 0.0248% of total target mass [75].

2.5.3 Installation and Performance

The dry ADs are assembled above ground at the SAB. Before filling with liquids, the AD interior is kept at a dry nitrogen atmosphere. The detectors are subjected to a dry run in which high voltage is applied to the PMTs and the ADs are checked for adequate perfomance. The completed AD is then hoisted onto a transporter that takes the detector into the liquid scintillator hall. All three AD zones are filled simultaneously over about two days using a procedure to minimize internal stresses due to pressure differentials and buoyancy of the inner vessels. Coriolis flow meters and load cells monitor the target mass during filling to $< 0.1\%$. The liquid scintillator is prepared with enough material for two ADs at a time. By filling the ADs pairwise, it is claimed that greater control over the target mass uncertainty can be achieved. The filled AD is then transported to its designated site and moved by overhead crane into its position on a stand within the water pool.

A comparison of the first two ADs to be commissioned was published in [27]. The first pair of ADs were declared to be "functionally identical". The ratio of the IBD rates between AD1 and AD2 after background subtraction was found to be 0.987 ± 0.009, compared with an expected ratio of 0.981 due to baseline differences. Since then the remaining six ADs have been commissioned and are all working to specification.

2.5.4 Detector-Related Uncertainties

We quickly list the dominant uncertainties related to the detectors. The first of these is the uncertainty in the target mass. As already discussed, pairwise filling with redundant mass measurement is used to guarantee that the target mass is known within a narrow tolerance. The effective target mass, however, is somewhat different due to spill-in and spill-out. Detector non-identicality may arise from varying scintillator density among batches; damage, dirt, or imprecise construction of the acrylic vessels; slightly different geometries; etc.

IBD neutrons in the target volume are thermalized in times on the order of tens of μs. Once thermalized, the capture time is exponential with time constant τ related to the average concentration of Gd in the detector module. The rate of capture, $\Gamma = 1/\tau$, is given by $\Gamma = \Gamma_{Gd} + \Gamma_H = [n_{Gd}\sigma_{Gd} + n_H\sigma_H]v$ where $n_{H(Gd)}$ is the number density of hydrogen (gadolinium) in the liquid scintillator, $\sigma_{H(Gd)}$ is the neutron capture cross section on hydrogen (gadolinium), and v is the velocity of the thermal neutrons. For liquid scintillator one generally obtains $1/\Gamma_H \sim 200$ μs, whereas for the Gd-LS we expect $\tau \sim 30$ μs. The fraction of neutrons that capture on Gd rather than H is then $P_{Gd} = 1/(1 + \Gamma_H/\Gamma_{Gd})$ and we would like to know this relative fraction between different detector modules to $\sim$0.1%. Thus we must measure the time constants τ for different detector modules to a relative precision of 0.2 μs, or about 0.5%.

In addition to the H/Gd ratio, the H/C ratio in the gamma catcher must be known within 1% to limit the uncertainty from spill-in events. This quantity can be accessed in several ways, from combustion analysis of the scintillator to NMR measurements of fluid samples to analysis of spallation neutrons within the detector.

Varying trigger efficiencies between detectors may also create non-identical performance. Trigger efficiency can be measured using LEDs to high precision following KamLAND. Redundant triggers also enable us to cross-check the trigger efficiency.

Live time varies between detectors also. The detector electronics uses a 100-MHz onboard clock to set the trigger window and record trigger times. The absolute time scale is given by synchronizing all detectors to a GPS signal. This level of precision will result in a very small uncertainty associated with the live time of the detector. During the analysis, numerous cuts are employed to filter out backgrounds. These cuts may be optimized for individual detectors, and thus create additional uncorrelated uncertainties.

The pairwise placement of the detector modules enables one to estimate the uncorrelated detector-related systematics. If the detectors receive identical flux, then the asymmetry between a given pair due to statistics alone should be $\pm$0.34% over the course of the experiment.

For all pairs of detectors, this asymmetry can be brought down to $\pm 0.04\%$ [1]. In practice the angle between the ADs can also have a significant impact on the flux measurement. Optimal positioning can bring the rate difference down to 1.5-2% [76].

As an illustration of the utility of swapping, let us consider two detectors at two different sites. Let $\epsilon_{1,2}$ be the efficiencies of detectors 1 and 2. Let $F_{1,2}$ be the fluxes at sites 1 and 2. Suppose that initially detector 1 is at site 1 and detector 2 is at site 2, and then later the detector positions are swapped. The total integrated flux at site 1 must be some weighted average of the two rates, namely $w_1\epsilon_1 F_1 + w_2\epsilon_2 F_1$, where w_1 and w_2 are functions of the time of each configuration and the average reactor power level during that period. For site 2, the total counts is $w_1\epsilon_2 F_2 + w_2\epsilon_1 F_2$. Taking the ratio of counts at site 1 to that at site 2, we obtain

$$\frac{F_1}{F_2}\left(\frac{w_1\epsilon_1 + w_2\epsilon_2}{w_1\epsilon_2 + w_2\epsilon_1}\right)$$

Now we observe that if we match the weights, i.e. $w_1 = w_2$, then the entire expression in parentheses drops out of the above ratio. Then the detector efficiencies have dropped out of the ratio altogether. Setting the weights equal in the above ratio is accomplished more easily on paper than in practice. Reactor power fluctuations and other uncertainties make it difficult to match the expected rates.

2.6 Muon Veto System

Many significant backgrounds are induced by cosmic ray muons. These events include scintillation and Čerenkov light from the muons themselves, fast neutrons created in the surrounding rock that then propagate into the detector, spallation neutrons generated in the AD itself, and various isotopes generated by muon showers. These will all be discussed more fully when we discuss the data analysis.

To contain these backgrounds, we have implemented redundant muon-tagging systems. The AD modules at a given site are immersed in an octagonal water pool, also called the

water shield, serving as a Čerenkov detector. Fig. 2.11 shows the detectors being deployed into the still-dry water pool. An opaque Tyvek film divides the pool into an inner region containing the ADs and an outer region. The near-site (far-site) outer zone contains 109 (128) inward-facing PMTs and 64 (96) outward-facing PMTs. The inner zone is more densely populated, with 96 (128) inward-facing PMTs and 20 (32) upward-facing PMTs. In addition to the water shield, a roof of RPC (resistive plate chamber) modules will tag most muons at low to moderate zenith angles. The combined tagging efficiency of the two systems is expected to be better than 99.5%.

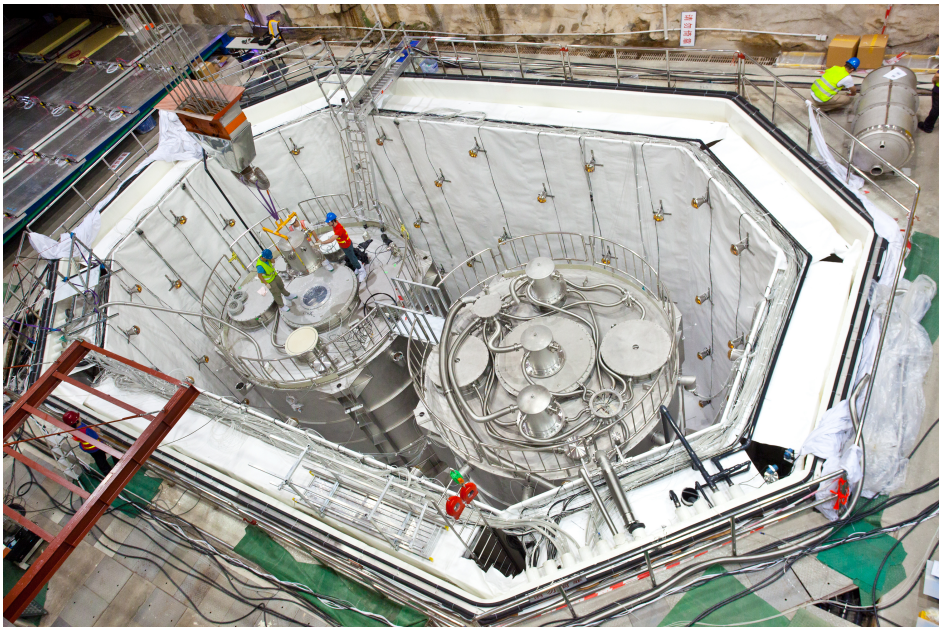

Figure 2.11: Two detectors deployed in the water pool before filling.

A number of designs for the veto system were considered in the earliest phases of the experiment, including a liquid scintillator pool [77]. The final two-volume octagonal water pool design was chosen because it offers a number of advantages, including:

- Attenuates radiation from surrounding rock, air (e.g. radon), or dust.

- High tagging efficiency since PMTs are more densely packed and are more suitably positioned.
- More space, and hence easier to calibrate.
- Temperature stabilization.
- Easier to circulate and purify water, partly due to less material needed for supporting structures.
- Saves about 500 T of water and requires the removal of 500 m^3 less rock.

The design also offered some disadvantages, such as challenges in the deployment of AD modules, inaccessibility of AD modules once deployed, and greater complication in the design of the water pool calibration system, to name a few [78]. The water is highly purified. The minimum distance from the side wall of the water pool to an AD is 2.5 m. The walls of the pool are coated to seal leaks and prevent radon from leaking into the pool from the rock.

In addition to the features we have mentioned, the Daya Bay experiment has designed and deployed RPC modules over every water pool. These may be employed for future redundancy, cross-checking, and increased efficiency in muon tagging, but they are not currently considered in the identification of neutrino events for any oscillation analyses.

2.7 Photomultiplier Tubes

The basic detector elements in the Daya Bay antineutrino detectors are photomultiplier tubes, or PMTs. These are essentially amplification devices that detect light and convert it to an electronic signal. In brief, light incident on the photocathode of a PMT can cause the release of a photoelectron via the photoelectric effect. This electron is accelerated toward a metal plate called a dynode. When the electron strikes the dynode, its kinetic energy causes the release of several more electrons. Through a sequence of such dynode stages, the signal is amplified until a measureable charge pulse is registered at the anode.

2.7.1 PMT Selection

Daya Bay considered two types of PMTs for its detectors, the Hamamatsu R5912 (which was selected) and the Electron Tubes 9354KB (used by Double CHOOZ [79]). Both are 8-inch tubes with approximately 2π coverage, i.e. the field of view encompasses the entire forward region. The Hamamatsu tube has ten dynodes, while the Electron Tubes tube has 12. Selection criteria included high quantum efficiency; large peak-to-valley ratio for ease of identifying the single-photoelectron peak; linearity of the gain with applied voltage; spectral response matched to the scintillator spectrum; and low rates from dark current, pre-pusling, afterpulsing, and radioactivity from the PMT itself [28].

The Hamamatsu PMTs were ordered with two designs: waterproof PMTs for the water shield and oilproof PMTs for the ADs. The circuit boards at the base of the PMTs were developed by members of the Collaboration. A small number of 2-inch calibration PMTs are also deployed in the ADs for various monitoring purposes. In addition, Daya Bay was donated 438 EMI tubes (9350KA and D642) and 45 Hamamatsu tubes (R1408) left over from the MACRO experiment [80].

2.7.2 PMT Potting and Testing

A laboratory at the Dongguan University of Technology (DGUT) was remodeled and equipped for testing the Hamamatsu PMTs. PMTs were shipped to this facility from the manufacturer, and the units were inspected and labeled. To "burn in" the PMTs, they were placed in a dark box for three days and subjected to high voltage corresponding to a gain of 10^7. The burn-in procedure is intended to stabilize operating characteristics and reduce the rate of post-installation failures due to infant mortality. Afterward, the PMTs underwent a battery of tests [81].

MACRO tubes were repotted at the Institute of High Energy Physics (IHEP) in Beijing since the original bases were not designed for underwater operation. The MACRO tubes

were also submerged in a pressure tank to test their mechanical strength. The potting procedure for these tubes was designed with multiple safeguards to prevent water leakage into the tube. Some tubes were found to fail when water managed to wick into the PMT base through cracks in the cable jacket. The cracks could be located by submerging the PMT cable into salt water and measuring the resistance between the cable and the bath. After potting and pressure testing, the MACRO tubes were shipped to DGUT for more extensive testing.

Pressure testing of tubes was continued on some sample of the PMTs at the Daya Bay site by submerging PMTs in ultrapure water at 30 psi for 12 hrs (later reduced to 8 hours) [82]. Some of the tubes imploded during pressure testing. The pressure gauge on the tank would drop suddenly, and upon opening the tank the PMT cathode were found be cracked or completely shattered. The glass of the photocathode would turn clear as the bialkali coating apparently dissolved. This mode of failure was observed to be correlated with the mass of the PMT [83]. PMTs with thinner glass are found to be more susceptible to pressure failures.

A paper describing the PMT testing and characterization procedures is currently being written.

Magnetic field effects

PMT performance is known to deteriorate in the presence of ambient magnetic fields. Because this effect depends on the orientation of the PMT, this effect could also reduce the uniformity of each AD. The earth's field at Daya Bay is about 44,908 nT (changing about 4 nT per year), oriented 2.5 degrees west of north and pointing downward at 39.6 degrees from the horizontal [84]. At MiniBooNE, welds used in the PMT frames created some local magnetic field, but this was determined to be insignificant to PMT performance [85].

Tests have shown that the signal amplitude varies about 30% by changing the orientation of the PMT [86]. Another study showed a variation of 25% for the EMI and Photonis PMTs

and 12% for Hamamatsu PMTs, although the comparisons were not with the same models of PMTs from which we were deciding [87]. Rotation about polar axis was shown to create a greater variation for EMI tubes than for Hamamatsu tubes. In addition, the peak-to-valley ratio dropped by 20-30% and the collection efficiency fluctuated by 35-50%, although the gain did not change significantly.

To compensate for the magnetic field, there was an early proposal to rotate the PMTs so as to minimize the variation in the performance due to earth field [88]. Experiments with other methods showed that a cylindrical mu-metal shield could reduce the magnetic field by a factor of 7 [89]. Finally there was a decision to use a Finemet cone shield. This was shown to reduce the variation in detection efficiency due to the earth's residual magnetic field below 5% [90]. A radial shield in AD covers up the PMT magnetic shield, so that the Finemet cones cannot complicate the detector optics [91].

We have simulated the effect of the field with a simple three-part PMT geometric model including the photocathode, the first dynode, and the focusing grid, assuming that the entire effect is due to a variation of the collection efficiency at the first dynode [92]. Using a finite difference method we calculated the electric field within the PMT due to the voltage applied between the photocathode and the first dynode, making some approximations to account for the open boundary conditions.

Assuming monoenergetic electrons with energy given by the peak of the photocathode response curve and assuming a cosine dependence of the momentum with respect to the surface normal, we then integrated the equations of motion, following the electrons until they either left the grid boundary or struck the first dynode. With this technique we mapped out the collection efficiency of the PMTs for electrons emanating from different points on the cathode surface. The variation over the cathode was seen to vary from about 20% for no applied field to 100% with a field of 0.5 gauss. By taking the field to be transverse to the PMT axis, we translated this into a $\pm 15\%$ variation in the overall collection efficiency depending on the orientation of the PMT.

The magnetic effect was also empirically studied at Brookhaven National Lab and UIUC. Field-canceling Helmholtz coils were used to negate the effect of the earth's magnetic field to study the PMT under "free" conditions. On the left-hand side of Fig. 2.12 the coils are clearly observed to effectively cancel the earth's field, and the PMT response is uniform over the photocathode surface. On the right-hand side the presence of the earth's field is seen to induce a dead region on the cathode surface.

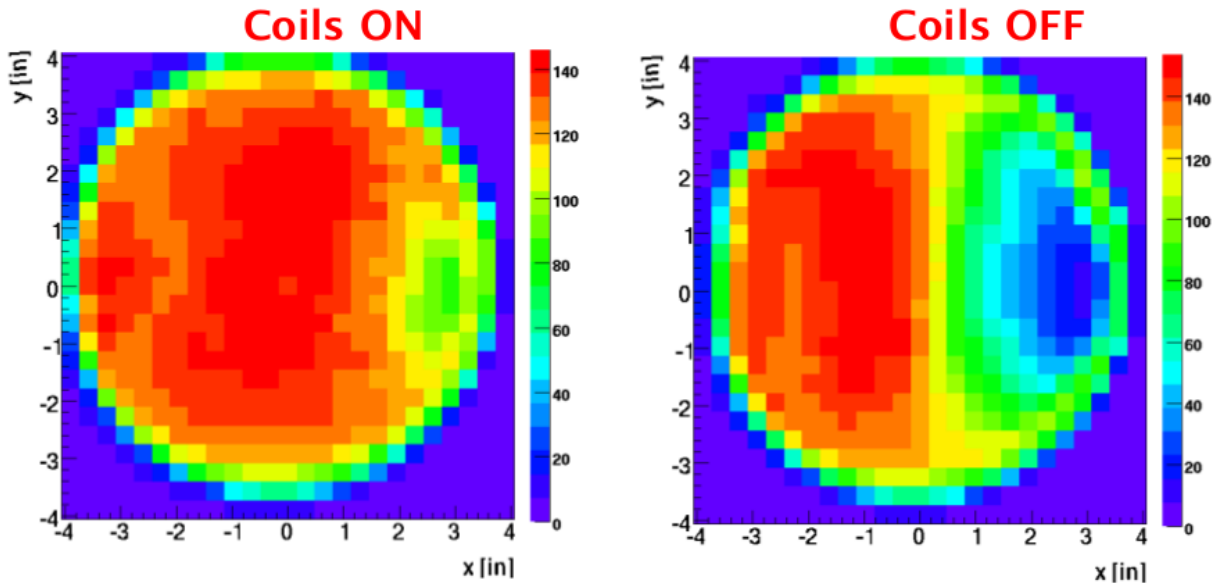

Figure 2.12: Variation in collection efficiency over the photocathode under the influence of the earth's magnetic field (right) and with field-canceling Helmholtz coils (left) [29, 93].

2.7.3 PMT Electronics

The PMT electronics were designed with a number of considerations. The signal is required to be within 1.5 mV of the baseline 400 ns after a pulse for prompt events. For the delayed signal (actually events with more than 100 photoelectrons) the PMT signal is required to return to be at 1% of its peak value 500 ns after the main pulse [94]. Because the experimental

	SPE peak height (V)	SPE charge (pC)
7-m cable	0.0167 ± 0.0003	1.53 ± 0.01
45-m cable	0.0097 ± 0.0002	1.14 ± 0.02
Attenuation	42%	26%

Table 2.7: Measured mean height and integrated charge for the single photoelectron peak of PMT signals in two cable lengths. The attentuations are relative to the 7-m cable [42].

sensitivity depends heavily on the energy calibration, considerable thought must be given to the ways that the electronics can distort the energy scale. The PMTs themselves may have poor gain or timing precision or high noise rates, which will worsen the energy resolution. Dead PMTs in the detectors would also have some effect. The electronics may limit the dynamic range due to saturation of the ADCs, low sampling rates, suboptimal triggering conditions, or a poor baseline restoration [95]. The same FEE boards are used for both the muon system and the AD PMTs [96].

The PMT output signal carried on the same coax as the voltage supply. It is necessary to use a signal decoupler to extract the higher frequency PMT pulse from the voltage supply line. Because it is difficult to get an accurate measurement of the integrated pulse charge, the pulse height is used as a proxy for the PMT integral. The signal is subjected to a pulse-shaping circuit, which stretches and modifies the signal, and the resulting charge measurement based on the amplitude of the shaped pulse has been shown to be reliable.

Because different PMTs are connected to cables of different lengths, it has also been necessary to measure the relative cable attenuation. These measurements are summarized in Table 2.7.

A few other PMT features

As the underlying detector elements, PMTs have been extensively studied to make sure that they are well-understood and characterized. A number of interesting observations are

made about PMT behavior, which are handled in various ways both in the data acquisition and in the analysis. For example, RC components in the PMT base can cause ringing in the output at the PMT anode. In addition, pulse-shaping and baseline restoration circuitry introduces some distortion in the PMT signal, such as PMT overshoot, which is the tendency of the signal to go below its baseline value immediately following a large pulse. Some more attention to these effects will be given in Section 3.3.

Following a large signal, PMTs may exhibit afterpulsing, causing spurious triggers following the primary trigger in a short time interval. Afterpulsing is believed to be due to ionization of residual gas molecules within the PMT bulb. The positively charged ions migrate back to the photocathode, where they induce a second cascade of electrons. The afterpulses have been observed to occur with distinct time and charge signatures corresponding to the q/m ratio of the corresponding ions.

2.7.4 PMT Mounting and Installation

PMT assembly was performed above ground at the SAB facility. The tested tubes were shipped from Dongguan to Daya Bay, and then the PMT bases and Finemet shielding were assembled and attached to the PMTs. Actual installation was performed by contractors.

The mounts were designed so as not to put excessive strain on the base of the PMTs. The weight of the PMT should be on the neck of the tube and not on the base pins, which could lead to failure. In addition, the supports needed to account for any buoyant forces on the tubes due to the liquids. Finally, as mentioned previously, the PMT mounts had to be carefully constructed so as not to create weld joints with local magnetic fields [97].

PMT sorting

Daya Bay has given thought to the problem of sorting the PMTs during installation in the detectors. PMT sorting has two goals: make ADs as identical as possible, and maximize

performance of each AD [98]. There were several options: installing the PMTs randomly, actively trying to distribute the PMTs for greatest uniformity, or installing the PMTs nonuniformly to maximize light collection or some other aspect of performance [99]. The metric most considered for distinguishing PMTs was the quantum efficiency, though others were proposed.

We performed an investigation of different sorting methods based on a deterministic light model in which the PMTs were sorted by quantum efficiency (drawn from a distribution) and the best PMTs were placed either at the top, bottom, or center of the detectors. We also looked at random placement. Sorting was shown not to decrease the light yield but to have an effect on the uniformity of the AD. The vertex resolution was not significantly affected by this PMT sorting. The energy resolution, being statistics limited rather than limited by the vertex uncertainty, is unaffected by sorting [100].

Ultimately we decided not to sort PMTs in our detectors [101]. However, since slight systematic biases are not critical to the performance of the water pool, the MACRO tubes were installed at the top of the water pool where they would be subject to less intense pressure than the Hamamatsu tubes. This was intended to prolong their lives since they are more susceptible to pressure damage.

2.8 Electronics, Trigger, and DAQ

The front-end electronics (FEE) of the data acquisition (DAQ) system were largely developed by the Collaboration. Each PMT signal is amplified and split for time and charge measurement, with each FEE board handling 16 PMT channels. The muon veto system uses the same design of electronic boards as the AD. The RPCs use a separate electronics system.

The raw data coming from the DAQ essentially consists of time and charge information. The charge information is recorded in terms of the analog-to-digital converter (ADC) value,

while the time information is recorded in terms of the time-to-digital converter (TDC) value. Each trigger board maintains the local time as well as receives a timestamp from a global GPS clock. In this way signals in different boards can be synchronized offline. To avoid saturation of the electronics during high-charge events, we extend the dynamic range of the DAQ by using two amplifier-ADC pairs. The fine scale ADC has a range up to about 400 photoelectrons, while the coarse scale ADC extends to about 4000 PEs.

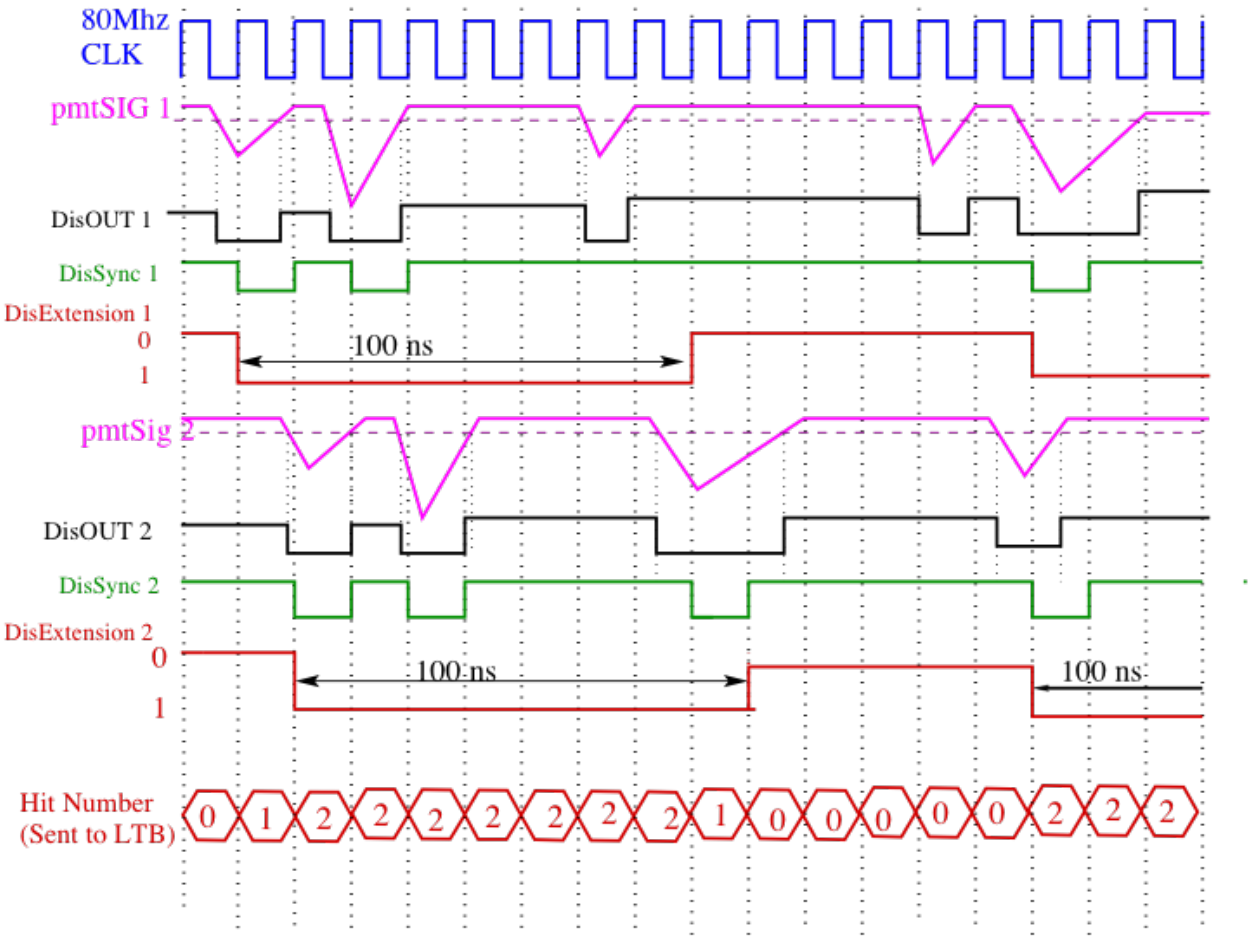

Figure 2.13: The basic priniciples of the trigger electronics are illustrated [102].

The basic idea of the NHIT trigger condition, which is a minimum threshold of the number of PMTs registering a signal to read out the electronics, is illustrated in Fig. 2.13. The

shaped PMT waveform is passed to a charge discriminator which returns TRUE whenever the signal is above threshold. (Actually below threshold, since we are working with negative high voltages.) The discriminator output is synchronized to the 80-MHz onboard clock that checks at the beginning of every clock cycle whether the discriminator output is true or false. Following a signal, a 100-ns window is opened to allow for variation in the response times of different PMTs as well as allowing enough time for all the light in the detector to be detected. The instantaneous sum of the number of ADC channels with an open trigger window is the value of NHIT for the given clock cycle. When NHIT crosses some prespecified threshold from below, a readout occurs in which the time and charge information from each PMT are recorded to disk.

The threshold decision must be a compromise between trigger efficiency and noise rates. If the threshold is too high, low-charge events that just happen to be at the lower end of the SPE distribution will be discarded. If the threshold is too low, every little voltage fluctuation can cause the signal to go above threshold. At Daya Bay, each ADC channel threshold is set at approximately one-third of a photoelectron. The $\frac{1}{3}$-PE requirement means that the voltage threshold is one third of the way from the channel baseline to the mean charge of a single photoelectron. The trigger rate is dominated by natural radioactivity and cosmic-ray muons.

In addition to the NHIT trigger, a separate trigger condition may cause a readout of the DAQ. This is the ESUM trigger, which is a measure of the total charge in the detector. A carefully calibrated charge measurement is conducted offline during the analysis, but for the purpose of the trigger a rudimentary built-in circuit computes the ESUM in terms of the sum of ADC units of all PMT channels. Thus if a great deal of charge is concentrated in a few PMTs, the NHIT OR ESUM trigger will read out the raw data. The trigger conditions are set by Field Programmable Gate Arrays (FPGAs).

The measured prompt energy at the threshold for the IBD reaction is 1.022 MeV, but due to finite energy resolution the positron energy is smeared out. Allowing up to 3σ of

energy smearing, the low-energy threshold for the ESUM trigger is set at 0.7 MeV. With this setting we expect the efficiency for IBD positrons to be effectively 100%. The 8-Mev neutron signal easily passes the energy threshold.

2.9 Calibration and Monitoring

A number of radioactive sources were considered for calibration purposes, and we shall mention them again when we discuss energy scale calibration. For now we just mention that the sources may be divided into three types:

1. *Neutron sources.* Used to study the neutron response of the detector, especially the efficiency and neutron capture time. Examples: AmBe, ^{252}Cf, PuC, spallation neutrons, IBD events.

2. *Positron sources.* Used to study the positron response, calibrate the low end of the energy scale, set the trigger threshold, and investigate the relative quantum efficiency of PMTs. Examples: ^{22}Na, ^{68}Ge, IBD events.

3. *Gamma sources.* For energy scale calibration, especially detailed studies of linearity, stability, resolution, uniformity, and quenching. Examples: ^{60}Co, IBD neutron capture.

In addition to these sources, LEDs couple to a diffuser ball by optical fiber are used in the calibration of the ADs. The usefulness of LEDs is that the trigger time and the source intensity can be carefully controlled. A system of LEDs also surrounds the water pool for testing and calibrating muon veto PMTs.

During normal data acquisition, the calibration sources are deployed weekly. A full calibration run takes approximately one shift period, which is eight hours long.

As already discussed, the ADs included a variety of monitoring contraptions such as load sensors, level sensors, mass flowmeters, and attenuating length monitoring devices. Prior to

the filling and installation of each AD, they are subjected to a dry run in which sample data is collected. This is primarily a quality assurance procedure.

Each detector site has several gauges monitoring temperature, humidity, pressure, radon concentration, and other environmental parameters. The water system is monitored for changes in resistivity, and indeed some drop in resistivity has been observed. It is believed that there is some kind of biological contamination in the water system, but this is still being investigated.

A couple of other monitoring systems have been developed but do not seem to be in regular use. One of these is the mineral oil clarity monitoring system, which consists of a light beam with a retroreflector (called the "corner cube"). An LED sends a pulse of light from the top of the MO to the bottom of the detector, the light reflects from the corner cube, and then the reflected light is detected by a 2-inch PMT at the top of the detector [103]. Also, the ADs are equipped with CCD monitoring cameras. These were used to make some videos of the AD interior during filling but do not seem to have been used since. They were turned off because they were suspected of generating electronic noise within the DAQ.

Chapter 3

Analysis

3.1 Software

Before discussing any physics, we look at the behind-the-scenes aspects of data analysis, namely data management and software. Since all data analysis is done offline with the aid of large computing clusters, these aspects of the experiment can be as intricate as the design of the detectors themselves. In this section and the next we discuss these technical details, and then in Section 3.3 we bring hardware and software together to make the first steps toward extracting physics from the Daya Bay experiment.

3.1.1 NuWa and The GAUDI Framework

The earliest version of the Daya Bay software, `g3dyb`, was a relatively simple simulation code based on GEANT, version 3. GEANT is a high energy particle physics simulation tool developed at CERN for the tracking of particles in matter, including the interactions and trajectories of secondary particles. After upgrading to Geant4 and embedding the simulation in the GAUDI framework, the Daya Bay code was rechristened `NuWa`, after the Chinese deity Nüwa (女媧). The name is also supposed to resemble the English word "newer" spoken in a Long Island dialect, reflecting the fact that the software is constantly under development [104].

As just mentioned, the Daya Bay simulation and analysis software is built around a customized implementation of the GAUDI framework, a code which was originally developed

for LHCb. GAUDI has been in continual development since 1998 [30], though this long history does not seem to have improved its usability. Other experiments using GAUDI include ATLAS, BES III, GLAST, HARP, and MINERνA [105].

Daya Bay's decision to base its simulation and analysis code on this framework was supported by GAUDI's emphasis of modular design, its separation of data from algorithms, its distinction between data in memory versus data on disk, and the need for minimal recompilation due to its reliance on dynamically loaded libraries [106]. In practice these features seem to have complicated the analysis more than facilitating it.

GAUDI's basic features reflect its object-oriented design, and their description can apparently only be accomplished by introducing a new lexicon [107]:

Algorithm User-written code retrieving the raw data and doing the actual data processing.

Job Sequence of algorithms applied to a data set for multi-step processing.

Tool Reusable code implementing specific, commonly used functionality.

Service Object providing framework-wide functionality, such as printing error messages, random number generation, and accessing data.

Transient Data Store (TDS) Object holding temporary information for processing by a job. Example is the Transient Event Store (TES), which stores information about a single trigger at a time.

Archive Event Store (AES) Object storing lookback information for triggers in a specified time window.

These descriptions may seem rather opaque, and indeed it turns out that these features have largely been promoted by computer experts who do not actually analyze data. They are very careful to distinguish between developers (themselves) and users (physicists who are supposed not to ask questions).

GAUDI depends upon a number of libraries, including the C Standard Library, ROOT, GSL, AIDA, Boost, CLHEP, Geant4, and the Python Standard Library. Users may write algorithms in either C++ or Python. The native GAUDI code is written in C++, which runs faster since it is compiled rather than interpreted. However, most of the Gaudi classes are given Python wrappers since most end users prefer the quick turnaround of Python scripting to more laborious development in C++.

In the author's experience, much of the software development has only reinforced a divide between final users and developers. Experts' obsessions with abstract principles of object-oriented design took precedence over physicists' needs for transparent, useable code. This gradual entanglement in a nearly unworkable software framework inhibited collaborative analysis, and this was enabled by the leadership's early lack of interest in the offline development and the rank-and-file's dogmatic acceptance of experts' recommendations—a true emperor's new clothes phenomenon.

The basic NuWa algorithm is a class with three member functions. The `initialize()` function runs at the beginning of a job to set up any necessary services, initialize variables, and declare any histograms or other data containers. The `execute()` function loops over events, accessing triggers one by one as they pass through the transient event store. At the end of an algorithm, `finalize()` is called to clean up any dynamic memory, save histograms, write data files, etc.

Code development is maintained through the use of a Subversion (SVN) repository. SVN allows many simultaneous developers to create multiple parallel branches of the simulation/analysis software for the purpose of testing new code and then merging these additions, once validated, into the main code, called the trunk. SVN also allows users to specify earlier versions of NuWa other than the most recent one. The current version of the software is rebuilt nightly, and a stable release version is frozen from time to time. NuWa is typically run on one of five computing clusters: the IHEP cluster in Beijing, PDSF at Lawrence Berkeley National Laboratory, the COOP and RACF clusters at Brookhaven National Laboratory,

and the Onsite Offline Computing Cluster at Daya Bay.

The author has supplemented the tools provided with NuWa with a custom library of streamlined data storage and visualization objects such as one- and two-dimensional histograms, scatterplots, descriptive statistics, etc. These are stored in binary files and post-processed locally to speed analysis and allow more direct access of raw data. This also permits the use of many other statistical analysis programs that are nearly impossible to interface with GAUDI, such as R.

3.1.2 Simulation

Detector Simulation

To model detector response, detailed materials and geometry information about the Daya Bay detectors must be specified. This information, as well as the orientation and position of all detector sites, is contained in XML files. The geometry information is quite detailed; for example, the antineutrino detector description contains the stainless steel vessel, radial shield, top and bottom reflectors, the AD "ribs", multiple overflow volumes and associated tubing, PMT cable trays, the PMTs themselves, and a number of other small detector components. These XML files also contain detailed materials information necessary to the simulation, such as the scintillation spectra of all fluids; their Birks constants; the isotopic composition of the steel, glass, and other construction materials; and so on.

NuWa uses the GiGa interface to GEANT to simulate the detailed physics of particles traveling through detectors. That is, a user desiring to simulate a particle in a detector must write a Python script specifying a list of physical processes to be simulated, and NuWa then uses GiGa to execute GEANT within the GAUDI framework. The physical processes available fall into the following six categories: general (generators and decays), optical (scintillation and Čerenkov processes), electromagnetic (Brehmstrahllung, Compton scattering, photoelectric effect, etc.), electronuclear processes, hadronic processes, and ionic

processes [108]. When simulating muons, the large number of photons is prohibitively slow. In this case some importance sampling is used to speed the muon simulation [109].

Kinematic Generators

After specifying the geometry, materials, and physics, it remains to set the initial state of the primary particles. Generating vertices and intial momenta is the role of kinematic generators. The particle type and its initial conditions may be either fixed or random. In the first case, one might for example decide to simulate 5-MeV isotropic positrons at the center of the detector, specifying this in the code or at the command line. More commonly, one would want to simulate vertices uniformly distributed throughout some specified volume, with momenta thrown according to a given distribution.

Perhaps the most important generator, the generator for inverse beta decay particles, gives the initial states of the neutron and positron resulting from IBD events. The positron spectrum (which is directly related to the neutrino energy) depends on the energy-dependent cross section and the reactor neutrino spectrum. Estimated fluxes for the six reactor cores are maintained in a database with one entry per day [110]. Since there are 33 energy bins per spectrum, the smooth spectrum is obtained by interpolation. The IBD rate at each detector depends also on the number of target protons and the precise baselines, but these quantities do not affect the shape of the spectrum. The γs arising from neutron capture are handled separately from the IBD generator [111].

The muon generator is based on a separate study of the muon flux at Daya Bay. A detailed muon simulation was performed starting with the Gaisser formula for the angular distribution of cosmic muons. These were then propagated through rock using the detailed mountain topography of the Daya Bay site to obtain a set of muon vertices at each of the Daya Bay detector sites. The output of this study is provided as a lookup table to the muon generator, which randomly samples from these vertices. Because of fast neutrons and showers originating in the surrounding rock, the correct orientation of each detector site is

important to the accuracy of the angular distribution of the muon flux [112].

Other generators are provided for calibration sources and even the LED diffuser ball. Radioactive backgrounds were initially handled with old Fortran legacy codes with C++ wrappers [113], but this has been superceded by a single package based on the Evaluated Nuclear Structure Data File data sets maintained by the National Nuclear Data Center [114]. This package essentially automated the lookup of radioactive decay channels and the generation of secondaries.

Our contribution to the simulation software was the initial development of a ^{8}He/^{9}Li generator [115]. These isotopes are important backgrounds that we will discuss later. For the generator we determined the important decay channels and their branching ratios, Q-values, and widths, considering only those pathways followed by delayed neutron emission. Decays to broad levels were modeled with a Breit-Wigner distribution. The ^{8}He/^{9}Li generator was improved by other authors with the addition of new channels and other modifications [116, 117, 118].

Electronics, Trigger, and Readout Simulation

When sensitive detector elements (PMTs or RPCs) in the detector simulation register a hit, this information is stored. In the next phase of the simulation, the hit is converted into an electronic pulse. The electronics model must account for many effects related to the shape and amplitude of the pulse. Nonlinearity and charge saturation in the PMT response, for example, mean that both the amplitude and the shape of the PMT waveform depend on the charge generated by the hit. (Saturation may also be due to the scintillator response.) Baseline restoration of the signal must account for ringing and overshoot in the PMT pulse [119]. In addition, the electronics simulation must model prepulsing, afterpulsing, and dark noise, as well as account for variations in calibration parameters. PMT flashing is not implemented.

The output of the electronics simulation for PMTs is a set of realistic ADC and TDC

values, as well as an ESUM variable representing the front-end electronics' (uncalibrated) estimate of the total deposited charge [120]. This information is then fed into the trigger simulation to make a trigger decision based on the ESUM, NHIT, etc. Finally, the readout simulation packages the simulation results into the same format used for the real data. Simulated data files may be processed and analyzed by the same algorithms as real data files.

To produce these realistic Monte Carlo data sets, we must ask: how should the different types of events from different generators be combined so that they resemble realistic data? Three methods were developed to address this problem. One option is to generate initial vertices for each of the particles of interest and then allow the simulation to run as usual. Essentially each particle is assigned a random timestamp along with the initial state kinematics, and then these are input to the detector simulation. A second option, which is simpler to implement, is to run the detector simulation separately for each type of particle and mix the output after the physics processes have been simulated but before the electronics simulation [121]. In both cases it is necessary to set the rates of each type of event prior to running the simulation [122]. The third option is readout-level mixing, whereby all primaries are simulated through the electronics level and only mixed prior to readout [123]. Once the first stage of simulation is done, this method allows for fast remixing of the data, and the user can adjust the rates of each particle type after the fact. The downside is that this method may not properly treat events that are overlapping in time [124].

3.1.3 Simulated Data Sets

Particle physics experiments rely heavily on simulated data to validate analyses, justify selection criteria, estimate efficiencies, understand basic distributions and features of the data, and compare real results with predictions. From 2008 through 2010, five official data sets were produced biannually. The simulation group called this the Mock Data Challenge,

although in fact there was no competition, and a small group of code developers was responsible for providing these simulated data. The goal during this period was to produce 15 minutes worth of realistic data at both the Daya Bay near and the far sites, and this in part drove research on mixing techniques to combine the simulated data sets.

By 2011, when data collection began in earnest, serious production of mixed Monte Carlo data sets kicked into high gear with Fast Monte Carlo Production (FMCP) data sets representing 100 days of real detector data at the near site. The meaning of the word "fast" in the name is somewhat apocryphal, but is often claimed to signify the various optimizations and sample reuse necessary to overcome computational speed limitations. When we discuss any comparison with simulation, we refer to the FMCP data sets. These simulated data include IBD events, radioactive backgrounds, muons and muon products, and calibration sources [125].

3.1.4 Real Data

As trigger data passes through the TES, raw data is accessed through data objects called headers, which are just C++ classes with accessor functions use to retrieve information. At the level of individual PMT channels, the basic information available consists of the number of hits (with a maximum of five per channel per trigger) and the ADC, TDC, and pre-ADC values of each hit. Some other information related to the onboard electronics, but of less interest to the actual data analysis, is also available.

The end user is typically not interested in accessing the raw data. Calibration algorithms convert the raw ADC (charge) information to energies and the raw TDC (clock time) information to calibrated times. The calibrated data are used by reconstruction algorithms to estimate the true particle energy, the location of the interaction, muon tracks, etc. Starting from the calibrated and reconstructed data, real physics analysis can proceed.

It is worth mentioning that many collaborators performing data analysis have elected

to use alternative methods to access data and perform analysis. Most common is the use of ROOT scripts to analyze preprocessed data, avoiding the use of the NuWa data model altogether. The KUP data (described in the next section) are essentially pre-processed by NuWa scripts to allow for "on-the-fly" analysis by most collaborators. In addition, some collaborators use NtupleAna, a "lightweight analysis framework" meant to simplify access and analysis of data [126]. In general, most students took recycled scripts passed down from a few senior developers and applied them to pre-processed data in which almost all calibration, reconstruction, data filtration, and selection cuts had already been made. This model made even the most trivial changes to the analysis quite challenging.

The moral of this section is that the same rules that we apply to politics should equally well be applied to any analysis team: equal participation, democratic decision-making, transparency of algorithms as opposed to use of black boxes, and unobstructed access to raw data. In the absence of these features, a hierarchical system of dependence and patronage develops that prohibits independent analysis and verification of results.

3.2 Data Management

3.2.1 Data Acquisition, Shift-Taking, and Data Quality

During data collection, two people are on shift to monitor detector systems. Shift responsibilities are divided among institutions, with each eight-hour shift lasting one week. A chronicle of shift observations is kept in an online ELOG, along with the records of other working groups, i.e. commissioning, PMTs, ADs, liquid scintillator, water pool, etc. Shifters initiate new runs, monitor trigger rates, environmental conditions, and keep a lookout for abnormal behavior. The above-ground control room contains several computers with GUI interfaces to the DAQ software. Runs typically last two days, with half a day per week devoted to calibration.

A record of all runs and their trigger conditions is maintained in the Offline Data Monitor (ODM). The ODM records basic distributions and statistics for physics, calibration, monitoring, diagnostic, and pedestal-measurement runs. Plots are automatically generated and saved. In addition, the ODM records data from the detector control system (DCS), also called the slow-control system. The DCS maintains high voltage settings, temperature readings, AD tilt sensors, etc. Information about the integrity of each data set is recorded in a portion of the ODM called the Physics Quality Monitor (PQM). An example of the PQM display is shown in Fig. 3.1. While shifters would not normally monitor the PQM, the offline Data Quality Working Group might use this information in constructing their good run list.

The standardized "DAQ configuration for stable data collection" specifies the AD local trigger conditions as follows: NHIT $>$ 45 OR ESUM $>$ 100 OR RANDOM [127]. The first condition causes a readout to occur whenever the whenever the number of fired PMTs (NHIT) exceeds 45. The ESUM condition is based on an onboard estimate of the total charge over all PMT channels. When this exceeds the charge corresponding to approximately 100 photoelectrons, the trigger condition is also satisfied. The RANDOM trigger is just an external trigger with some preset average frequency that reads out all DAQ information regardless of the state of the DAQ. Random triggers are acquired every 100 ms. For the inner (outer) water pool, the trigger condition is: NHIT $>$ 5(7) OR ESUM $>$ 40(45) OR RANDOM OR LOOKBACK. Again, the random trigger rate is 10 Hz. The LOOKBACK trigger is intended for studying muon-like events and works as follows: for some subset of the AD triggers, a signal is sent to the muon system DAQ. This cross-trigger induces a readout of the previous 200 μs of the water pool PMTs, which is possible because trigger information is stored for a short duration in buffers. In addition to trigger conditions, the DAQ configuration for stable data collection specifies the gain of the PMTs (10^7), the RPC configuration, the FEE threshold (the ADC value at which a PMT is said to "fire"), and other electronics settings.

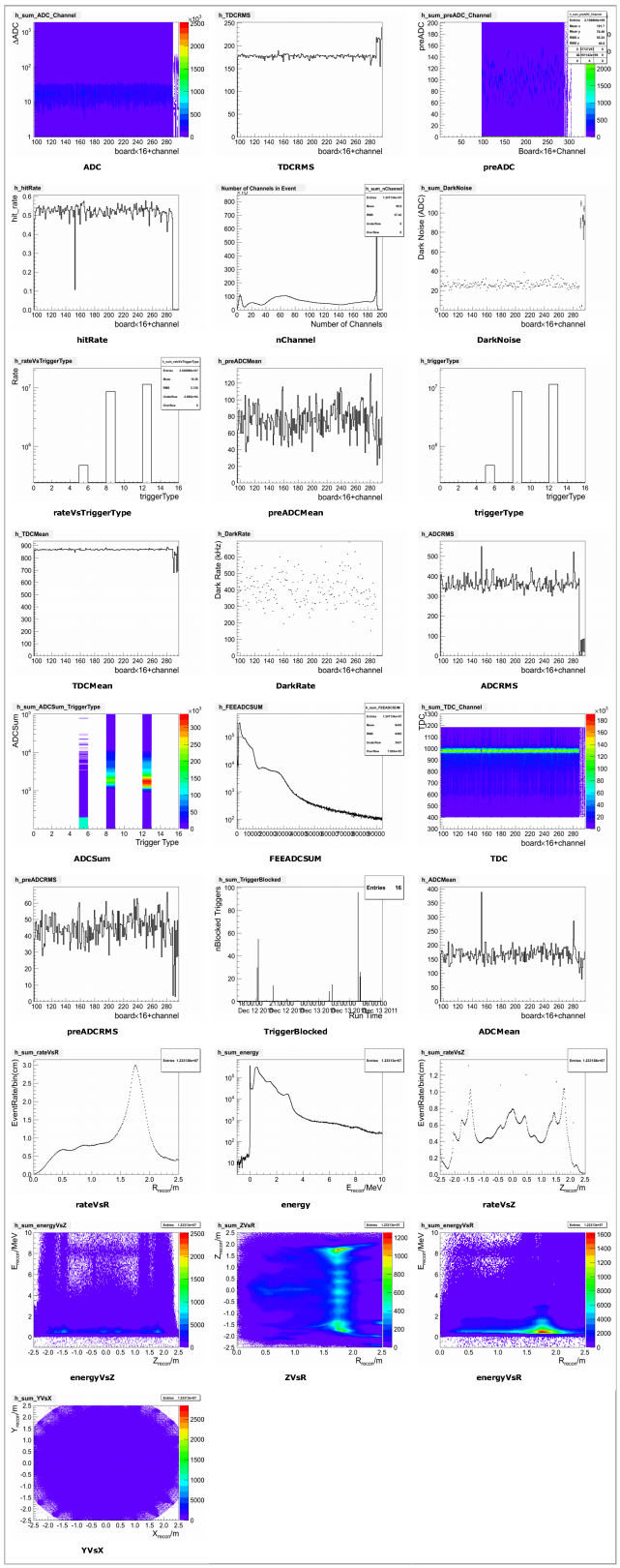

Figure 3.1: Example of PQM data quality monitoring plots.

With tens of thousands of runs (many of them just short calibration runs), it is essential to maintain a list of good runs for analysis. The Data Quality group maintains such a list down to the level of individual subruns. For a subrun to be declared good, they demand stable trigger rates in the ADs and water pools; low deadtime; and stable event rates for muons, spallation neutrons, flashers, and IBD events. The deadtime specification is actually a requirement that the fraction of triggers lost due to the finite readout time of the DAQ is less than 0.5%. This does not account for any kind of offline veto. Removal of subruns failing these criteria reduces the live time by 0.6% [128]. The location and retrieval of good run data is facilitated by a Python script called `Catalog`. The `Catalog` module returns the file paths of specified runs, allowing the user to filter by detector ID, site, and file type (KUP, ROOT, or NuWa's native data format).

3.2.2 Data Transfer and Storage

The Daya Bay experiment produces several hundred gigabytes of data per day. The exact trigger rate depends on many factors including the trigger conditions, the detector site, etc. Runs (periods of data collection at a single site with set trigger conditions) are broken into subruns for the purposes of data management, with a single subrun consisting of about 1 GB of data. A single run is typically broken into roughly 200 subruns, with a single subrun containing $\sim 10^6$ triggers.

Such a high data volume demands specialized systems to manage the data flow. After encoding raw data in the so-called "raw event format" [129, 130] the data files are transferred from Daya Bay to other locations via SPADE, a data movement system developed for the IceCube experiment. SPADE copies data files to remote servers as they are created, confirms the arrival and integrity of the transferred data, and keeps local disk space free for new data [131]. The transfer networks and storage available at each site are illustrated in Fig. 3.2. In addition to the files maintained on disk for analysis, backup tape archives are held at IHEP

and LBNL [132].

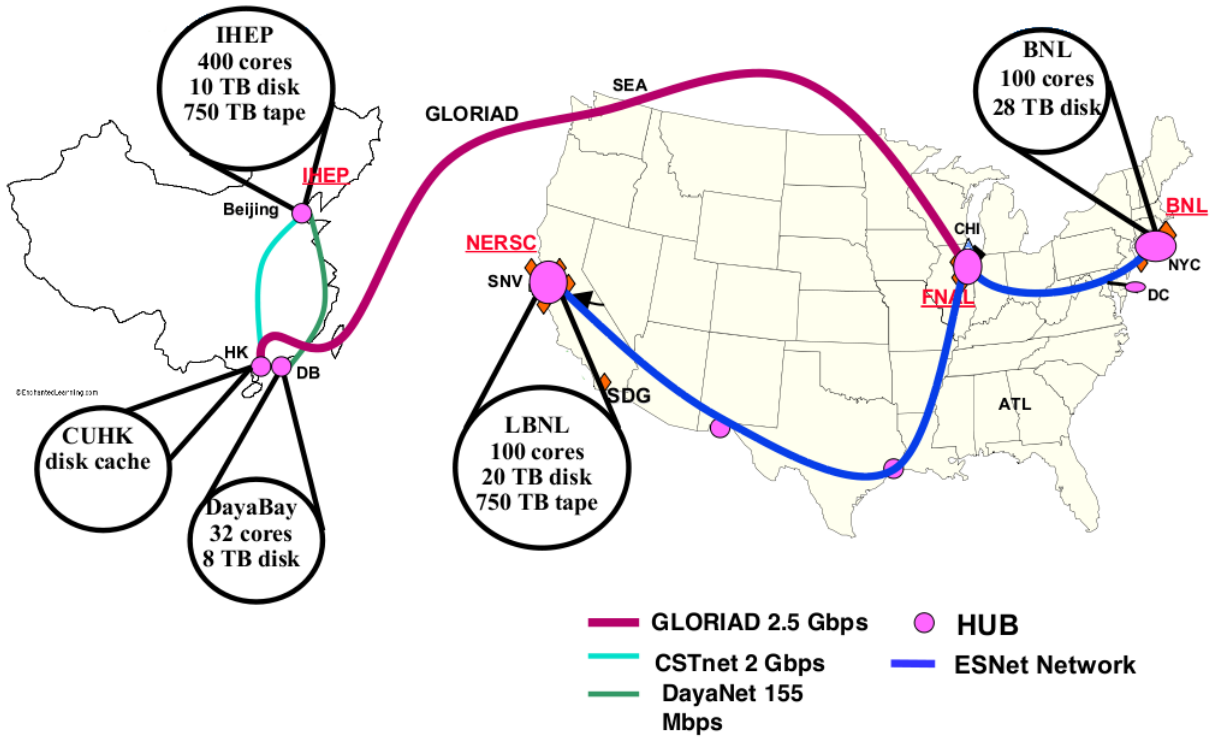

Figure 3.2: Data transfer network used by Daya Bay [132].

3.2.3 Hit Selection and Basic Data Processing

The use of a multi-hit TDC means that up to five hits may be recorded per channel per trigger. These hits occur with distinct timestamps, except in certain spurious cases in which the TDC records the same timestamp for multiple triggers. Since hits outside of some limited time range are likely to be noise, only the first hit per channel in the TDC range (-1650 ns, -1250 ns) is used [133]. It should be emphasized that this is enforced only offline at the beginning of the analysis phase of data processing. The hit selection criteria have changed

several times and may continue to be modified.

An automated data preprocessing system called Keep Up Production (KUP) has been developed to speed up the time between data collection and physics results. KUP automatically applies calibration and reconstruction algorithms to raw data files and stores the results for quick analysis. It is the majority opinion of collaborators that this system reduces the overhead of analysis and allows analyzers to have speedy access to basic distributions in the form of ROOT trees. By contrast, we feel that in fact the KUP system eliminates the ability of analyzers to access raw data and customize their analyses.

3.3 Detector Calibration

The first real step in the offline analysis of data is to calibrate detector elements. Since the basic information stored in the raw data format consists of ADC and TDC values, it is first necessary to take these digitized quantities and convert them into some physically meaningful information. That is the purpose of calibration. The calibrated charges and times can then be used to perform higher level analysis. Energy scale calibration and the use of the ACU sources will be treated in the next section. In some sense, energy scale calibration is already a higher-order analysis task. In detector calibration our goal is to bridge the gap between the detector and physics, and only then can we start talking about energy scale corrections.

Calibration constants are stored in MySQL databases, along with other important records such as the time-dependent reactor data, PMT voltage settings, and the mapping between PMT IDs and FEE channels. The database interface permits rollback, or the selection of calibration parameters for a given detector at a given time. The computer experts have call this setting the "context". Choice of context allows for the analysis of time-dependent data using time-dependent calibration constants. Where multiple algorithms have been used to estimate the same calibration constant, the user may choose among them by selecting the "task".

3.3.1 PMT Charge Calibration

As the most basic detector elements, the photomultiplier tubes must be well-understood and characterized. An accurate measurement of the neutrino energy depends crucially on our ability to measure charge in a PMT. Before going into the details, let us summarize the essence of charge calibration. The charge measured by the ADC is used to estimate the number of photoelectrons in a PMT. This number is then taken to be approximately proportional to the deposited energy.

The PMT signal contains a bias P, called the pedestal, which must first be subtracted. The zero of charge in ADC units then corresponds to no charge in the detector. This value is then converted into physical units by the gain factor G. If A is the raw charge in ADC units and Q is the calibrated charge in physical units, then charge calibration is essentially accomplished by calculating $Q = G(A - P)$. Since it is crucially important to get this calibration right, the estimation of the gain and pedestal, as well as corrections to the simple method of calibration outlined above, occupy a central role in the analysis. In passing we note that it is possible for the calibrated charge to be negative from time to time, which occurs when the pedestal is greater than the raw charge ($P > A$). Usually negative calibrated charges are ignored in any subsequent analysis.

3.3.1.1 Pedestal Subtraction

Since PMT signals are carried on the same transmission lines as the voltage supply, each pulse rides on top of a bias level, or baseline, which is removed by a decoupling circuit. The remaining bias is called the pedestal, which can have fluctuations due to noise in the voltage supply and in the FEE. To separate the signal from the noise, only pulses above some preset threshold are recorded. In order to reconstruct the charge of the PMT signal, it is necessary to subtract the pedestal from the raw ADC value of the PMT signal. For this reason, it is necessary to estimate the signal bias.

The pedestal can be measured by externally triggering the FEE. Since this kind of artificial trigger does not correspond to a real hit, the resulting ADC value should represent the baseline of the FEE channel when no physical signal is present. This approach has several problems, however. First, if the hit rate is sufficiently high, then the probability of the external trigger coinciding with a real signal increases, biasing the measured pedestal upward. At normal trigger rates this complication is not a real concern, and in any case is easily handled by using a robust measure of the baseline such as the median. A second concern with directly measuring the pedestal is that the signal into the FEE board is processed by a peak finding algorithm that selects the highest value of the ADC within a 300-ns window. The resulting pedestal measurement is thus biased upward by about 1.6-2.1 ADC units [134]. Also, pedestal measurements are observed to vary with temperature of the environment [135].

The main issue with a direct pedestal measurement is related to multiple hits in a very short time interval. In this case, the baseline may not have fully recovered to its equilibrium value when the second hit occurs. This baseline distortion is illustrated in Fig. 3.3.

As a solution to these problems with a dedicated pedestal measurement, we use instead a running baseline called the pre-ADC. The pre-ADC is an average of four ADC samples immediately preceding a hit. Thus every ADC measurement has an associated pre-ADC measurement. This allows for real-time measurement of the signal bias, which has been shown to yield more accurate charge measurements than using the pedestal from dedicated runs. The pre-ADC is calculated separately for the fine and coarse ADC scales.

The pre-ADC is not without its own complications. Since the ADC output cannot go below zero, the baseline restoration problem described above may not be fully corrected by the pre-ADC for large pulses. Moreover, the return of the PMT signal to its baseline is not a simple decay. Following a large pulse, the baseline may be affected by overshoot (overcompensation of the baseline restoration circuit), ringing (oscillatory decay to equilibrium), or afterpulsing. In addition, the pedestal has a natural spread due to voltage fluctuations

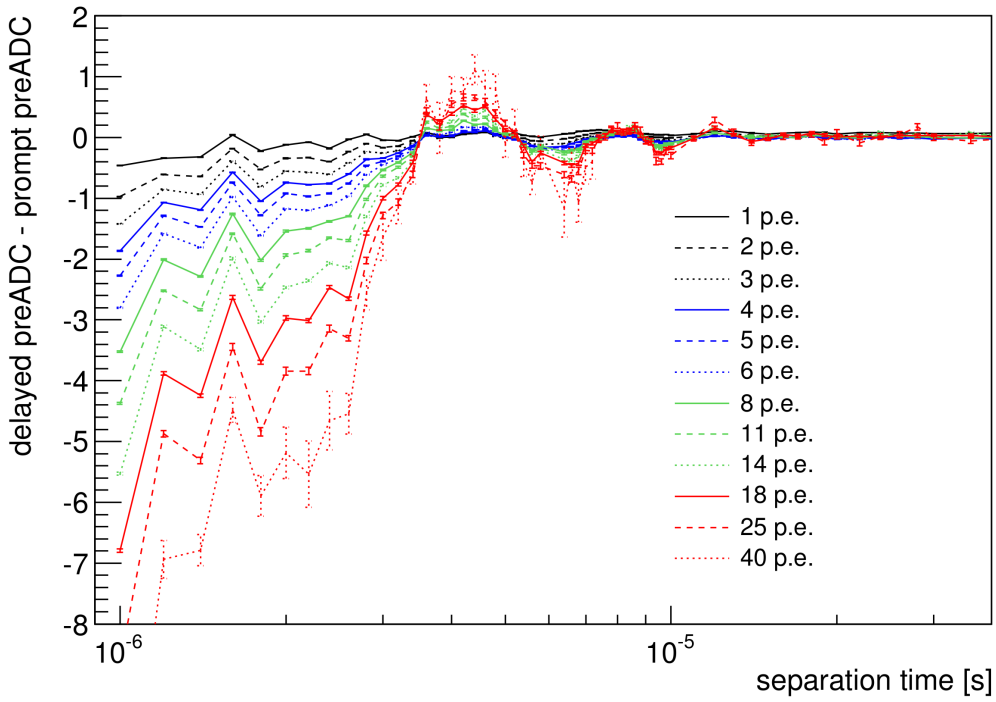

Figure 3.3: Baseline distortion for single FEE channel at various intensities of a double pulsed LED. The prompt signal refers to the initial pulse, while the delayed signal refers to the second pulse in each pair. For higher primary charges the baseline distortion is more significant, and the effect of ringing in the decoupler circuit becomes visible [136].

on the power supply. In addition, the pre-ADC has been observed to pick up a 5-kHz noise when the FEE threshold is set to a low value, and this noise can substantially alter the measured pre-ADC distribution [137].

The baseline restoration problem is illustrated in Fig. 3.4. In the figure, $t_{1,2}$ refer to the time that the PMT pulse crosses the FEE threshold and $x_{1,2}$ are the TDC values when the shaped and stretched pulse is maximum. Neither actually corresponds to the time in which the pre-ADC is sampled, which is represented by p. The time between the first trigger (which biases the baseline) and the second trigger has already been defined as $\Delta t = x_2 - x_1$. When

the first pulse is large and Δt is small, the pre-ADC recorded at time p does not accurately represent the baseline at time x_2.

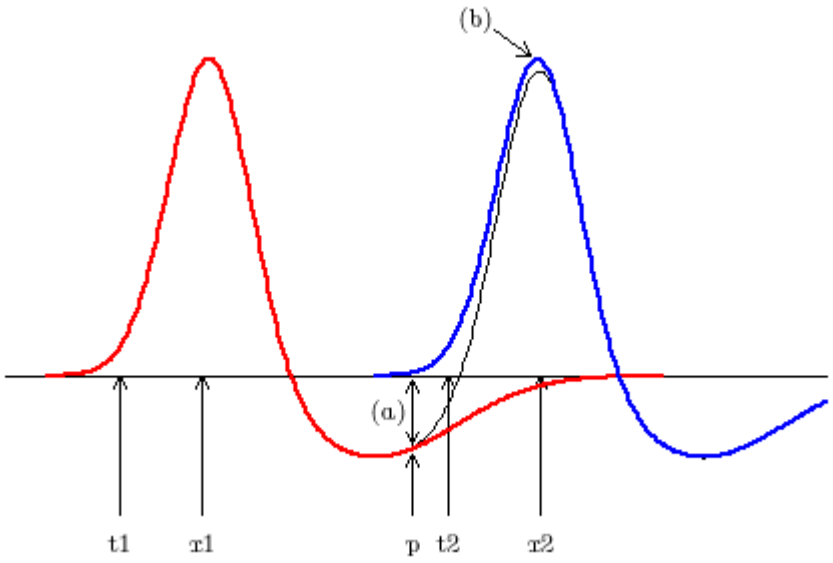

Figure 3.4: Illustration of two PMT pulses close in time with the later pulse in blue. The solid black line is the actual shape of the rising edge of the second PMT pulse, whose left side rests on the overshoot of the first pulse. By using the pre-ADC as a measure of the baseline, we use a value corresponding to the point (a), which is measured before the second pulse crosses threshold. Since we are interested in the peak height, however, it is actually the bias at point (b) that matters. The points labeled t_1, t_2, x_1, x_2, and p are explained in the main text.

When the time between adjacent hits, Δt, is large, we may use the pre-ADC as is. When Δt is small, it is better to apply some correction for the complications due to baseline restoration. We now illustrate a method. Our data are taken from a test run with a single LED flashing at 100 Hz. We take a subset of triggers with $0 < \Delta t \leq 1000$ ns and $0 \leq$ Last ADC ≤ 1500. In other words, we focus on triggers that follow other triggers within short time intervals, without regard to the charge of the first pulse. (The ADC cuts are not restrictive and encompass almost the entire range of the ADC. The remainder of the full ADC range contains too few triggers for analysis.) The distributions of the independent

variables are shown in Fig. 3.5.

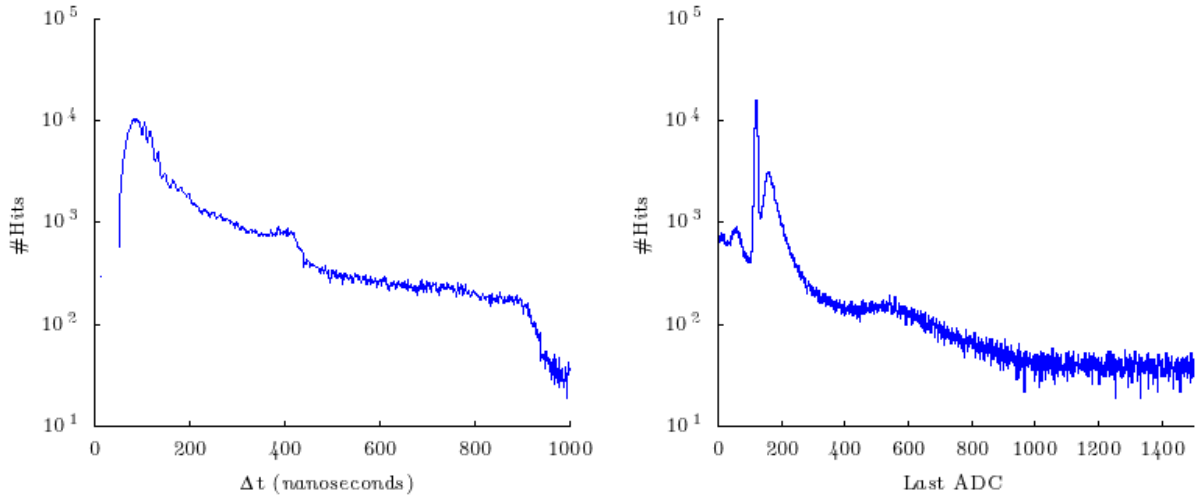

Figure 3.5: Left plot is the distribution of the time between hits. On the right is the distribution of the value of the last ADC, which is the same as the distribution of the present ADC value up to a single count. In addition, there are more than 2×10^5 counts at last ADC=0 (not shown).

One might expect the distribution of Δt in a run with an LED pulsing at frequency f will be dominated by hits with $\Delta t = 1/f$, but at these high trigger rates almost every LED interval is interrupted by other triggers. It is possible to decrease the time separation further using double pulsed LEDs, which are actually two LEDs with slightly different delays. However, the LED configuration at Daya Bay does not allow such short pulses, and so we rely on random triggers to obtain data for very short time separations. Furthermore, a double pulsed LED can only provide information about a single Δt, whereas we want to explore the baseline distortion over a range of pulse separations. In the remainder of our discussion about the pre-ADC measurement, we focus our analysis on a single PMT channel.

It has been shown that the shaped PMT pulse can be visualized by plotting the pre-ADC versus Δt with cuts on the value of the last ADC [138]. We use this method to produce the sequence of plots in Fig. 3.6. The height of the shaped pulse (as measured by the pre-ADC) depends on the value of the last ADC, which is not surprising given the correlation

between these quantities mentioned earlier. We also note that for large values of the last ADC, the pre-ADC is truncated at 0 in the overshoot region since negative ADC values are not possible. We remove the noise with the following cuts: The signal events are chosen to be those with $850 < \text{TDC} < 1000$ OR $111 < \text{this ADC} < 193$.

Having removed the noise, our goal is now to come up with some model for the shape of this surface, where the independent variables are TDC and Last ADC (value of the ADC for the first signal), and This ADC (value of the ADC for the second signal). We use the following probability model for the data:

$$\Pr(y|\mu,\sigma) = F_{\mu,\sigma}(0)\ \delta(y) + \mathcal{N}_{\mu,\sigma}(y)\ I(y>0)$$

F is the cumulative normal distribution, δ is the Dirac delta function, N is the normal density, and I is the indicator function that is 1 where its argument is true and zero elsewhere. This is just a normal gaussian distribution with the integrated density up to zero gathered as a point mass at $y = 0$. In other words, the distribution of signals above zero is supposed to be gaussian, but all data that would fall into the negative end of the ADC spectrum are simply placed at $y = 0$.

We fit for $\mu = \mu(\Delta t, \text{last ADC})$ using 2D tensor splines with a total of 25 degrees of freedom. The negative baselines in the overshoot region can thus be estimated. Essentially the maximum likelihood method compares the number of triggers with pre-ADC > 0 to the number of triggers with pre-ADC $= 0$ and thus arrives at some estimate of the depth of the overshoot, which is illustrated by Fig. 3.7.

We have worked backwards from data at small Δt to obtain a model for the shape and depth of the overshoot following a large pulse. To estimate the baseline for these hits we simply plug in the values of Δt and Last ADC into our model. In Fig. 3.8 we use our model to show the bias in the pre-ADC compared to the actual baseline at the pulse peak. If $P(\Delta t, \text{ADC}_{\text{last}})$ is our model, then the bias is given by $P(\Delta t, \text{ADC}_{\text{last}}) - P(\Delta t + T, \text{ADC}_{\text{last}})$,

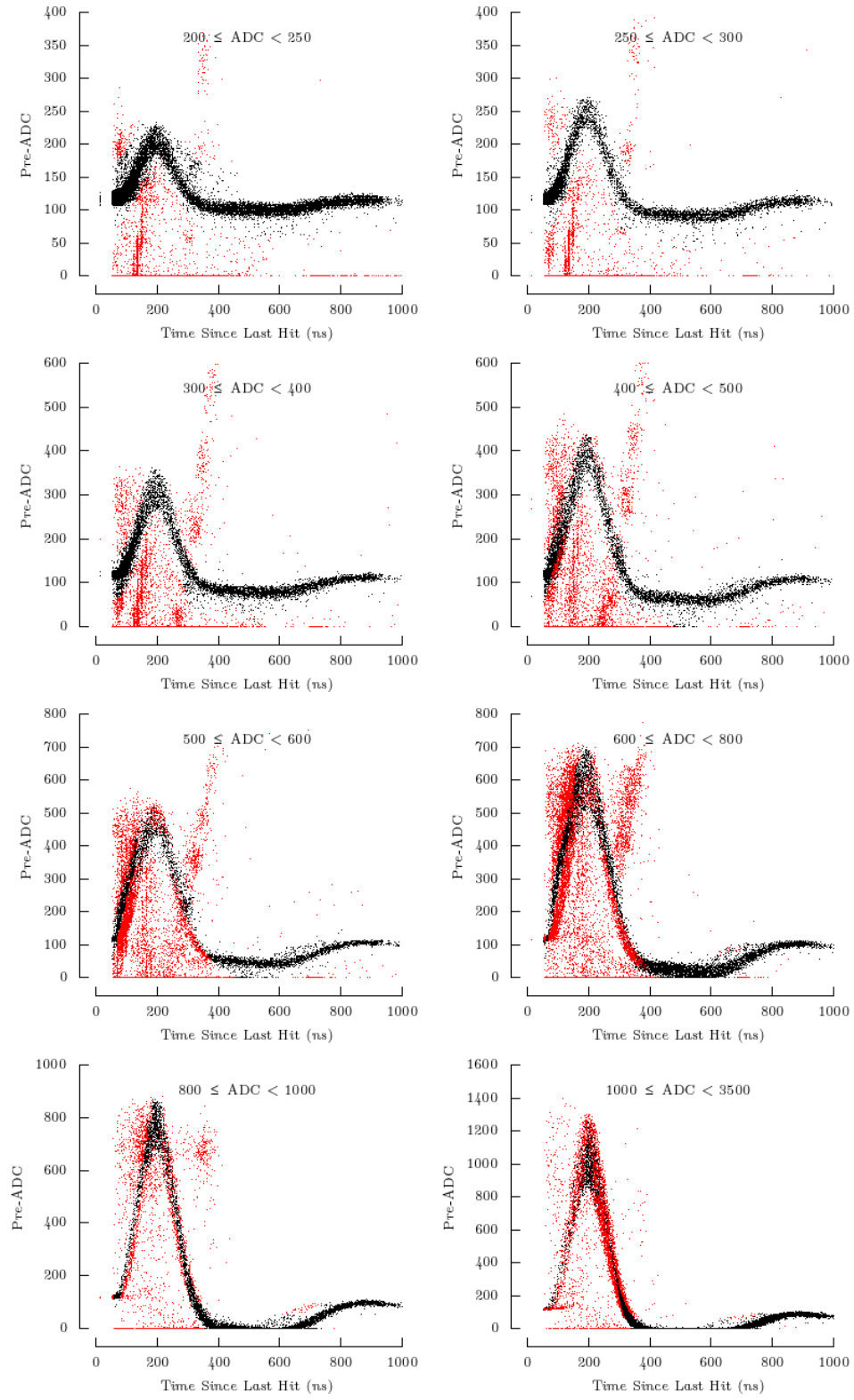

Figure 3.6: Pre-adc vs. Δt for different slices of last ADC. The red points are considered to be noise.

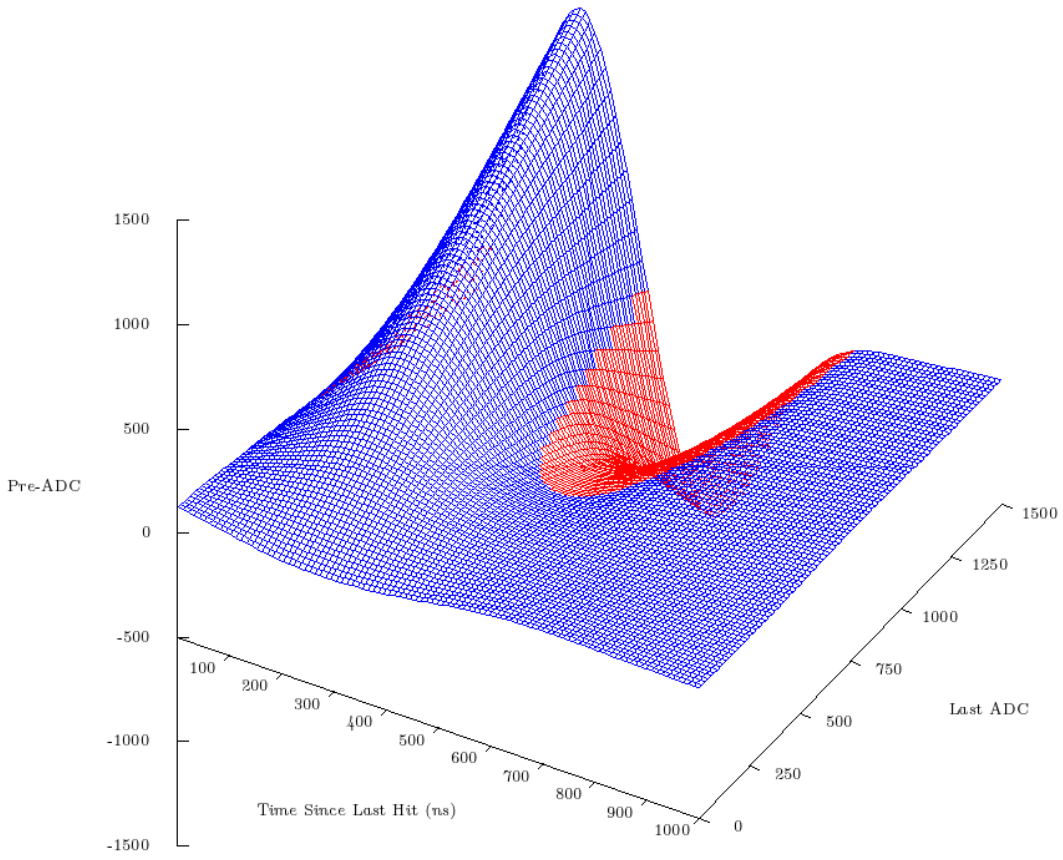

Figure 3.7: Pre-ADC versus the last ADC and time since previous trigger. The red area shows the estimated depth of the overshoot region, where pre-ADC < 0.

where $T = 200$ ns. For $\Delta t < 700$ ns this bias can be in the hundreds of ADC units, corresponding to perhaps twenty or thirty photoelectrons. In short, baseline restoration can bias the energy of such triggers by a few tenths of an eV.

We have shown that by parametrizing the waveform of PMT pulses we can estimate the bias in the signal baseline at small time separations [139]. A similar method has been implemented in NuWa using a seven-parameter model for the PMT waveform with these parameters tuned separately for each PMT [140]. For most triggers, however, the time separation is large enough that the pre-ADC is perfectly adequate as a measurement of the

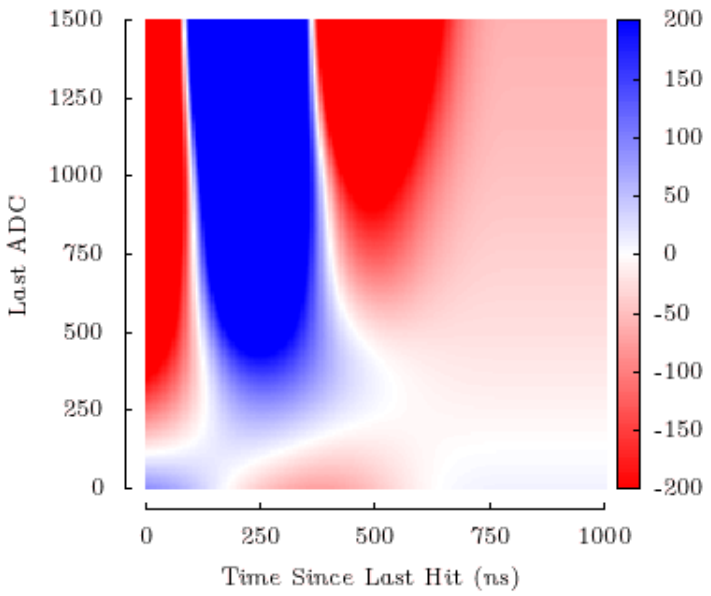

Figure 3.8: Estimated bias in the baseline caused by the time shift between the pre-ADC measurement and the peak PMT position. The points in red are biased low, and the points in blue are biased high. Points off scale are colored according to the closest extreme of the color scale. We use a time from pre-ADC measurement to peak position of 200 ns.

signal bias, and indeed is already an improvement over a periodically calibrated constant pedestal.

3.3.1.2 Gain

A number of effects can lead to variations in the responses of individual PMTs. Different quantum and collection efficiencies affect the probability that a photon will be converted to a photoelectron and register a signal at the PMT anode. Geometric effects may place some PMTs in the shadow of various detector elements or otherwise darker regions of the AD. In addition, variations in the dynode structure can result in different amplifications, or gains. The gain is simply the integrated charge at the PMT anode divided by the electron charge, e. A gain of 10^7 means that a single photoelectron produced at the photocathode results on average in an integrated charge corresponding to 10^7 electrons, or 1.6 pC, at the anode. The

distributions of the measured gains in SPE units for the first two ADs are shown in Fig. 3.9.

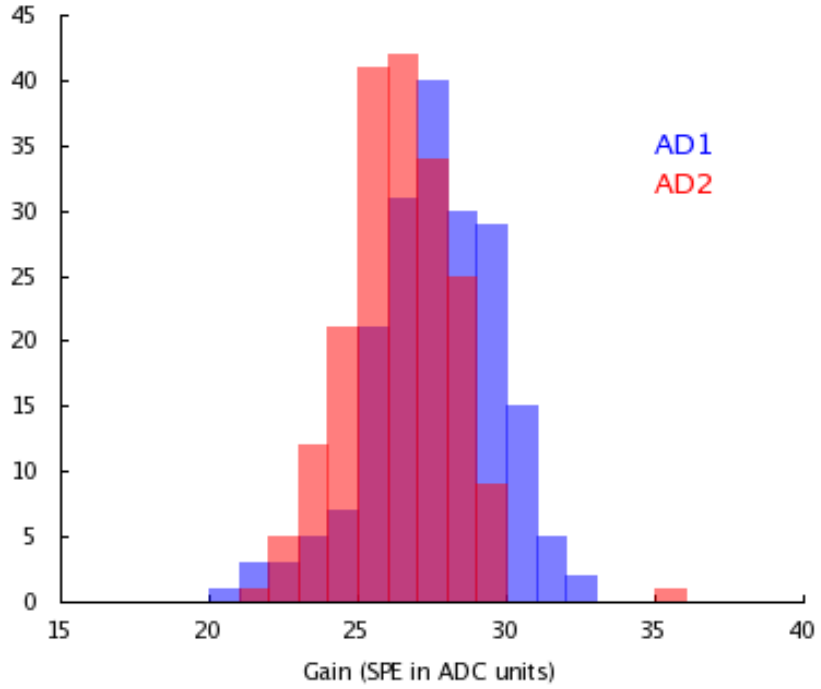

Figure 3.9: ADC position of the single-photoelectron peak in first two ADs.

The high voltage settings for each PMT channel were originally chosen to produce a gain of 10^7 based on measurements at DGUT. When these PMTs were installed at Daya Bay, some of the operating characteristics had changed, and the HV settings had to be recalculated.

Measurements of gain typically use low-intensity LED or noise spectra to locate the positions of the single photoelectron peak and the pedestal. With higher-intensity sources, the single-photoelectron peak has much lower probability and may be obscured by a multiplicity of higher-photoelectron peaks. When the positions of both peaks have been identified in an ADC spectrum, then the difference can be used to calculate the gain of the PMT. In practice the pedestal may be measured separately or its position may be inferred from the ADC spectrum. Because the Daya Bay electronics exclude the pedestal by the application

of an FEE threshold to cut out excessive noise, our fitting methods fall into the category of using an implied pedestal. However, because we measure the pre-ADC, we have the ability to compare the estimate of the pedestal resulting from a fit with the pre-ADC.

At Daya Bay several models are in place to measure the gain. The "Full Model" fits the ADC spectra to a physically motivated functional form and thus measures the gain [141]. The original authors of the physical model emphasize that it can be broken down into its components for greater interpretability [31]. The "Rolling Gain" model has been developed to study the variation of PMT gain over time, i.e. to check for stability in the calibrated gains [142]. TDC cuts remove afterpulses and select dark noise events, which are supposed to correspond to one photoelectron. Comparisons of fitting to dark noise versus fitting to a low-intensity LED do not prefer either method [143].

There is no absolute measurement of gains with which we can compare the results of fitting to various models. Also, high precision in the gain measurement has little impact on the energy resolution [144]. Thus it is adequate to calibrate the gains relative to some reference PMT, and we now demonstrate how this can be accomplished with a modified version of the Full Model.

The multiplicity of photoelectron peaks in the ADC spectra is modeled as a mixture of gaussians weighted by their Poisson probabilities. The so-called "ideal" spectrum is given by

$$S_i(x) = \sum_{n=0}^{\infty} \frac{\mu^n e^{-\mu}}{n!} \cdot \frac{1}{\sqrt{n}\sigma_1} \phi\left(\frac{x - nQ_1}{\sqrt{n}\sigma_1}\right) \tag{3.1}$$

where μ is the mean number of photoelectrons (proportional to the source intensity), Q_1 is the mean charge output in response to a single photoelectron, and σ_1 is the width of the single-photoelectron peak. ϕ is the standard normal density. Note that Q_1 is just the gain expressed in ADC units per photoelectron.

The backgrounds are modeled as the sum of a gaussian (pedestal) and an exponential

(noise):

$$B(x) = (1-w)\frac{1}{\sigma_0}\phi\left(\frac{x}{\sigma_0}\right) + w\theta(x)\alpha e^{-\alpha x} \tag{3.2}$$

The relative contributions of the two terms are controlled by the parameter w. The noise term with decay constant α is defined only for $x > 0$ through the Heaviside θ-function. The pedestal width is given by σ_0.

The "real" spectrum is the convolution of $S_i(x - Q_0)$ and $B(x)$, where Q_0 is the location of the pedestal:

$$S_r(x) = (S_i * B_{Q_0})(x) = \int_{-\infty}^{\infty} dy\, S_i(x-y)B(y-Q_0) = \sum_{n=0}^{\infty} \frac{\mu^n e^{-\mu}}{n!}\left[(1-w)I_1 + wI_2\right] \tag{3.3}$$

writing $B_{Q_0}(x)$ for $B(x - Q_0)$. The first integral is

$$I_1 = \frac{1}{\sqrt{\sigma_0^2 + n\sigma_1^2}}\ \phi\left(\frac{x - Q_0 - nQ_1}{\sqrt{\sigma_0^2 + n\sigma_1^2}}\right) \tag{3.4}$$

Writing $\sigma_n = \sigma_0^2 + n\sigma_1^2$, we have for the second integral

$$\begin{aligned} I_2 &= \alpha \int_{-\infty}^{x} \frac{1}{\sigma_n}\ \phi\left(\frac{u - Q_0 - nQ_1}{\sigma_n}\right)\ e^{-\alpha(x-u)}\, du \\ &= \frac{\alpha}{2}\exp\left[-\alpha\left(x - Q_0 - nQ_1 - \frac{\alpha\sigma_n^2}{2}\right)\right]\operatorname{erf}\left(\frac{y - \alpha\sigma_n^2}{\sqrt{2}\sigma_n}\right)\Bigg|_{y=-\infty}^{y=x-Q_0-nQ_1} \\ &= \alpha\exp\left[-\alpha\left(x - Q_0 - nQ_1 - \frac{\alpha\sigma_n^2}{2}\right)\right]\Phi\left(\frac{x - Q_0 - nQ_1 - \alpha\sigma_n^2}{\sigma_n}\right) \end{aligned}$$

where Φ is the standard normal cumulative distribution function.

In this model we have glossed over the fact that the $n = 0$ component in Eq. 3.1 is not well-defined. In the paper originally describing this model, this is interpreted as the limit $\sigma_0 \to 0$ of a normal distribution, a represention of the Dirac δ-function. After convolution, the background term $B_{Q_0}(x)$ appears explicitly as the $n = 0$ component of S_r.

At Daya Bay the FEE threshold is chosen as a compromise between the needs for signal

efficiency and a low noise rate. This threshold removes the pedestal from our ADC spectra and alters the shape of the spectrum. The Full Model solution to the threshold modeling is simply to drop the $n = 0$ term from Eq. 3.1. One problem with this approach is that it not only removes the pedestal, but it also removes the contribution of this term to the ADC spectrum at higher ADC values. We could consider applying the threshold directly by fitting only for $x > x_0$. With a 1/3-PE cut, $x_0 = Q_0 + \frac{1}{3}Q_1$, but unfortunately we are in the circular situation where we do not know either Q_0 or Q_1 until after we have already done the fit.

Another solution is to truncate S_r at some value x_0, smear out the resulting spectrum by convolution with a gaussian of width ρ, and then include x_0 and ρ in the list of parameters to be estimated. The smearing is necessary because the ADC spectra do not exhibit a hard lower cutoff. This is due to the fact that the thresholding is applied to the raw PMT pulse, but the ADC readout corresponds to the pulse height after passage through the shaping circuit. The result of this calculation still gives Eq. 3.3, but I_1 and I_2 are substituted with

$$I_1' = \frac{1}{\sigma'}\phi\left(\frac{x - Q_0 - nQ_1}{\sigma'}\right)\left[1 - \Phi\left(\frac{x_0 - \tilde{\mu}}{\tilde{\sigma}}\right)\right] \tag{3.5}$$

where $\sigma' = \sqrt{\sigma_n^2 + \rho^2}$, $\tilde{\sigma} = (\sigma_n/\sigma')\rho$, and $\tilde{\mu} = (Q_n\rho^2 + x\sigma_n^2)/(\sigma'^2)$; and

$$\begin{aligned} I_2' = \alpha \exp\left[-\alpha\left(x - Q_0 - nQ_1 - \frac{1}{2}\alpha\sigma'^2\right)\right] \times \\ \frac{1}{\rho}\int_{x_0}^{\infty} \Phi\left(\frac{y - Q_0 - nQ_1 - \alpha\sigma_n^2}{\sigma_n}\right)\phi\left(\frac{y - x + \alpha\rho^2}{\rho}\right) dy \end{aligned} \tag{3.6}$$

To the extent that ρ is small, we may treat the second factor in the integrand as a δ-function, whence

$$I_2' \approx \alpha \exp\left[-\alpha\left(x - Q_0 - nQ_1 - \frac{1}{2}\alpha\sigma'^2\right)\right]\Phi\left(\frac{x - Q_0 - nQ_1 - \alpha\sigma'^2}{\sigma'}\right)\theta(x - x_0) \tag{3.7}$$

Comparing I_1 and I_2 with I_1' and I_2', we see that the only differences are the substitution

$\sigma_n \to \sigma'$ and the appearance of weighting factors (which for I_2' is just the Heaviside θ-function).

We are now in a position to fit the above model to data. The fit is very sensitive to the choice of starting values. There are many local minima in the fit criterion (the residual sum of squares), and with inadequate starting values the fit can be quite poor. Fortunately we have the pre-ADC data at our disposal to estimate the position (Q_0) and width (σ_0) of the pedestal. We can also guess the location of the first photoelectron peak ($Q_0 + Q_1$) from the maximum of the ADC spectrum. The FWHM (divided by 2.35) is used to obtain a starting value for σ_1.

This is not yet good enough. In particular, the expected number of photoelectrons (μ) and the normalization factor (N) both significantly affect the χ^2 and are not stable against different choices of their starting values. It turns out that the number of counts in the ADC spectrum is not a good initial guess for N. To find good starting values for the parameters, we generate 1000 random vertices in the parameter space, keeping Q_0, σ_0, Q_1, and σ_1 close to their initial guesses, and we choose the best of these. The Full Model, having fewer parameters than the modified version, seems to give a more robust fit. Since we perform this minimization first, we can use the results from the Full Model fit as our initial guesses to restrict the search space for the starting values of the modified model. With an enlarged parameter space, we now use 5000 initial random vertices to locate a starting point for the modified model.

It is also important to choose a fit range in which the ADC spectrum is well above zero. In particular, if x_i is any possible ADC value and $f(x_i)$ is the number of counts in the ADC spectrum with charge x_i, then letting A be the set of ADC values for which the spectrum is at least 3% of the maximum (i.e. $A = \{x_i > 0 : f(x_i) \geq 0.03 \max_u f(u)\}$), we fit to the range $[\min A, \max A]$.

A poor choice of starting value for μ usually leads to a bad fit in the upper tail of the ADC spectra. In order to improve the fit in the tail, and perhaps to stabilize the algorithm

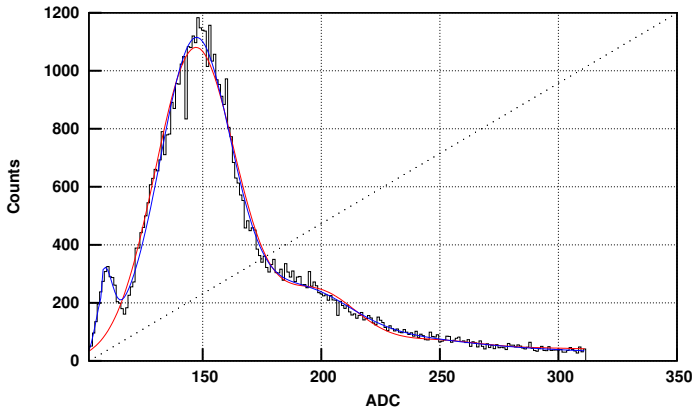

Figure 3.10: ADC histogram for a single channel. The fit to the model we described is shown in blue. A simplified model is shown in red.

against unsatisfactory guesses of μ, we may try to perform a weighted fit. Each ADC bin, with bin content $f(x_i)$, is given the weight $1/\sqrt{f(x_i)+1}$. Thus bins with fewer counts, such as those in the tails, are more heavily weighted. Because the χ^2 measure of goodness-of-fit is a sum of terms inversely weighted by the expected bin contents, the χ^2 statistic improves when we use weighted least squares. However, because the bins in the vicinity of the maximum of the ADC spectrum are de-emphasized by this method, the fit does not locate the single-photoelectron peak as accurately. Therefore we reject the use of weighted least squares in our gain calibration fits.

The minimization becomes prohibitive in such large spaces to find a better starting point by the method we have described. Our solution to this problem is to minimize the function, and then "kick" the fitted parameters by addition of a random vector. We iterate this process many times, decreasing the size of the "kick" at each iteration, until the spread of the last 50 sum of squared residuals is within 1%. We find that this procedure helps to avoid being trapped in local minima. An example of the results of both models on a particularly unusual ADC spectrum is shown in Fig. 3.10.

One may consider a number of other changes to the Full Model. For example, we have assumed perfectly linear PMT responses when we placed successive photoelectron peaks

Table 3.1: Correlations of fit parameters between the two methods.

Parameter	Correlation
μ	0.470
Q_0	0.951
σ_0	0.368
Q_1	0.786
σ_1	0.530
w	0.120
α	0.241
N	0.278

at intervals of Q_1. If for some reason the PMTs were nonlinear at low intensities, this assumption would be invalid. In fact it seems that photoelectron energy is independent of the light intensity, but we know of no results pertaining to the gain versus wavelength of the incident light.

The gaussian assumption for the peak shapes is also subjected to scrutiny. As mentioned earlier, differences in hit times and transit times across the first dynode stage mean that the two pulses forming the two-PE signal may not line up perfectly. Thus the width of higher-photoelectron peaks may in fact be broader than the Poisson $\sqrt{n}$ scaling in Eq. 3.3 would suggest.

The background modeling in Eq. 3.2 is a conspicuous candidate for adjustment. In the first place, we find little stability in the fitted results for the parameters w and α. The actual background shape may turn out to be quite different from the one-sided exponential. Furthermore, Eq. 3.2 is not even continuous at $x = 0$.

Future studies may further investigate the applicability of the Fuller Model to the muon dry run results. It would also be interesting to compare the two models studied here with the Crystal Ball fit as well as the simple gaussian fit. There is more work to be done regarding optimization of this algorithm. Uncertainties in the fitted parameters are also a target for future updates.

3.3.1.3 Coarse ADC Scale

Scintillation light produced in the Daya Bay detectors is detected as a set of charge pulses by an array of photomultiplier tubes (PMTs). These analog signals are processed by pulse-shaping circuits in the front-end electronics (FEE) and then converted to digital readouts. The Daya Bay data acquisition system (DAQ) uses two independent analog-to-digital converters (ADCs): a fine scale (ADC1) for small PMT signals and a coarse scale (ADC2) for larger signals. When the signal in ADC1 is below some preset threshold, the DAQ writes the fine scale output to the data stream. When the signal in ADC1 is at or above this threshold, up to and including the possibility that ADC1 is saturated, the DAQ writes the coarse scale output to the data stream. This use of two ADCs increases the dynamic range of the antineutrino detectors, allowing for better detection and veto of showering muons.

The ratio of the digital ADC units to the real charge at the PMT anode can be measured directly by injecting pulses in which the total charge is known into the FEE and simply reading the ADC output. One objection to this method is that the injected pulse, which comes from a pulse generator, does not resemble a real PMT signal. It may be difficult to perform this direct measurement after detector deployment. In this study we consider the possibility of finding the ADC scales indirectly from calibration data. In particular, we seek not the absolute calibration for each ADC, but the relative scale between ADC1 and ADC2. Since it is not necessary in any physics analysis to know the true charge read out by the PMTs, it is sufficient to measure only the relative scale between the two ADCs. This approach could be used for online monitoring of the scale factor.

After pedestal subtraction, the output from each ADC should be proportional to the integrated charge at the PMT anode. The only difference between the fine and coarse scales is the charge corresponding to a single ADC unit. Using primed variables to denote quantities in ADC2 units and unprimed variables to denote quantities in ADC1 units, we may write

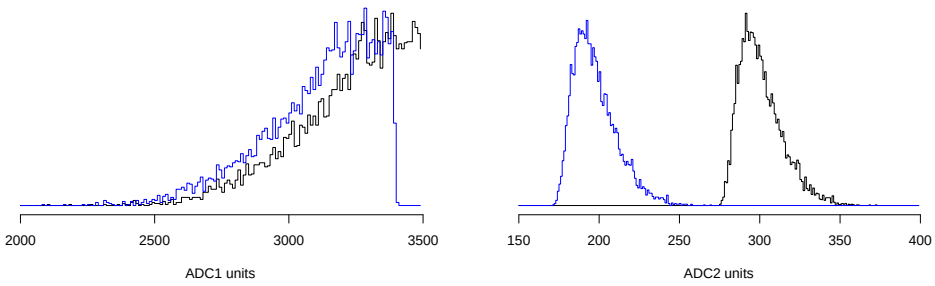

Figure 3.11: ADC1 (left) and ADC2 (right) spectra for a single FEE channel. Black is the raw spectrum; blue is after pedestal subtraction.

the transformation between the two scales as

$$y - \eta_1 = M(y' - \eta_2) \tag{3.8}$$

where M is the scale factor that converts from the coarse scale to the fine scale and η_1, η_2 are the pedestals in the two ADCs. It will be our task to determine M from the data.

The essence of our approach is to consider both ADC spectra, assume that they arise from a single distribution split into two halves by the existence of the threshold mentioned above, and then use maximum likelihood to fit a parametrized model for the two spectra. The relative scale factor M will be one of the fit parameters. This will be described in more detail in the next section.

In Fig. 3.11 we show example data for a particular FEE channel in which the counts in ADC1 (7662) are approximately equal to the counts in ADC2 (7888). We have shown the spectra in each scale before (black) and after (blue) pedestal subtraction. The data come from an LED calibration run with the LED intensity set so that both ADCs are frequently read out. In this particular run the LED is off center. Combined with the LED anisotropy, varying path lengths, and detector geometry, the relative occupancies of the two scales show considerable variation from one FEE channel to another.

We start from the assumption that the true charge distribution is gaussian. Inspection

of FEE channels in which the ADC spectrum is almost entirely in one ADC scale or the other shows that the gaussian assumption is reasonable. We assume this "true" distribution is measured in ADC1 units and rides on top of the ADC1 pedestal. With mean μ and standard deviation σ, the probability of reading out a charge z is

$$\Pr(z) = \mathcal{N}_{\mu,\sigma}(z) \tag{3.9}$$

This is the spectrum we would expect to see if the threshold were set suffiently high that the entire ADC spectrum were in ADC1 and if we have not subtracted any pedestal. The FEE cuts this single spectrum into two halves at the ADC threshold t, as illustrated in Fig. 3.12. The separate distributions for each scale may then be written

$$p_1(x) \sim \mathcal{N}_{\mu,\sigma}(x)\, I(x < t), \quad p_2(y) \sim \mathcal{N}_{\mu,\sigma}(y)\, I(t \leq y) \tag{3.10}$$

where we use x to represent a charge read out from ADC1 and y to represent a charge read out from ADC2 converted to ADC1 units via Eq. 3.8. I is the indicator function, which is 1 wherever its argument is true and 0 elsewhere. We refrain from using the = sign because the probabilities are not yet normalized.

From the blue histogram in the left-hand plot of Fig. 3.11 we can see that the upper cutoff of the ADC1 spectrum is not perfectly sharp as it is in the black histogram or in Fig. 3.12. This is entirely due to pedestal subtraction. Since the pedestals are calculated for each count as the average of the three ADC values preceding a readout, the pedestal itself is a random variable. A constant pedestal would have preserved the hard cutoff. In the case of ADC1, the mean and width of the gaussian are given by η_1 and ρ_1, which are just the mean and standard deviation of the ADC1 pedestal distribution. Both of these parameters are known from the empirical pedestal distribution.

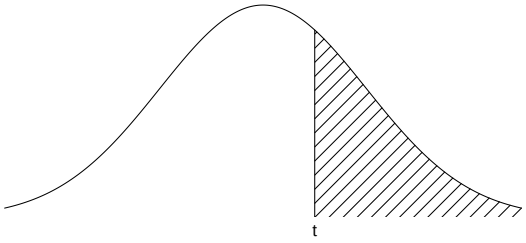

Figure 3.12: Single gaussian cut into two distributions at a threshold t. The unshaded region represents the ADC1 spectrum, while the shaded region represents the ADC2 spectrum.

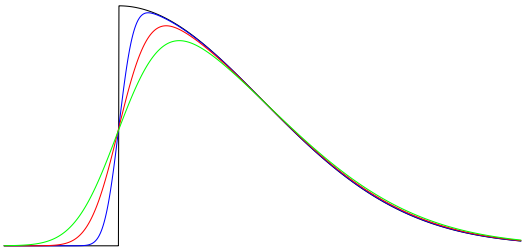

Figure 3.13: Representative shapes of the ADC2 spectrum with jitter, a truncated gaussian after convolution.

We model the smearing of the ADC1 spectrum by convolving $p_1(x)$ with a gaussian:

$$\tilde{p}_1 \sim p_1 * \mathcal{N}_{-\eta_1,\rho_1} \tag{3.11}$$

Carrying out the integral, we obtain

$$\tilde{p}_1(x) \sim \mathcal{N}_{\mu_1',\sigma_1'}(x)\, F_{\tilde{\mu}_1,\tilde{\sigma}_1}(-x) \tag{3.12}$$

with

$$\sigma_1'^2 = \sigma^2 + \rho_1^2$$

$$\tilde{\sigma}_1 = (\sigma_1'/\sigma)\rho_1$$

$$\mu_1' = \mu - \eta_1$$

$$\tilde{\mu}_1 = \eta_1 + (\rho_1/\sigma)^2 - (\sigma_1'/\sigma)^2 t$$

$F_{\tilde{\mu}_i,\tilde{\sigma}_i}$ is the cumulative gaussian distribution.

A similar effect smears out the lower cutoff of the ADC2 spectrum, but we can see from the black histogram in the right-hand plot of Fig. 3.11 that even before pedestal subtraction, the ADC2 data are already smeared. This is because the second ADC is independent from

the first. The decision to read out ADC1 or ADC2 is based on the ADC1 response, but ADC2 is not constrained by the value in ADC1 and may in principle register any value in its range. We call this effect the jitter of ADC2 with respect to ADC1. The smearing ρ_2 has two contributions: the pedestal width (known) and the ADC2 jitter relative to ADC1 (unknown). We treat ρ_2 as an undetermined parameter.

Modeling of the smearing in ADC2 is a bit more complicated than in ADC1. First we must transform the distribution $p_2(y)$ to ADC2 coordinates (before pedestal subtraction) by Eq. 3.8. This gives

$$p_2(y) \to M p_2(My' - M\eta_2 + \eta_1) = g(y') \tag{3.13}$$

Now we can proceed as for ADC1, starting with the convolution

$$\tilde{p}_2 \sim g * \mathcal{N}_{-\eta_2,\rho_2} \tag{3.14}$$

which gives

$$\tilde{p}_2(y') \sim \mathcal{N}_{\mu_2',\sigma_2'}(y') \left[1 - F_{\tilde{\mu}_2,\tilde{\sigma}_2}(-M\sigma^2(y' + \eta_2))\right] \tag{3.15}$$

with

$$\begin{aligned}
\sigma_2'^2 &= (\sigma/M)^2 + \rho_2^2 \\
\tilde{\sigma}_i &= M^2 \sigma \sigma_2' \rho_2 \\
\mu_2' &= (\mu - \eta_1)/M \\
\tilde{\mu}_2 &= (\mu + M\eta_2 - \eta_1)(M\rho_2)^2 - (t + M\eta_2 - \eta_1)(M\sigma_2')^2
\end{aligned}$$

We note that $p_2(y)$ takes its argument in ADC1 units, but $\tilde{p}_2(y')$ takes its argument in ADC2 units. The effect of this smearing is illustrated in Fig. 3.13.

In principle either ADC may now read out any possible real value. In practice, we fit data only within some predetermined window of ADC values. We fit ADC1 data x_i in a window

$a \leq x_i < t$ and ADC2 data y'_j in a window $0 \leq y'_j \leq b'$. The data x_i and y_j have already had their pedestals subtracted. This truncation of the spectra changes the normalization of our probabilities, and so we now replace $\tilde{p}_1$ and $\tilde{p}_2$ with the truncated distributions

$$q_1(x) = \frac{\tilde{p}_1(x)\, I(a \leq x < t)}{\int_a^t \tilde{p}_1(u)\, du}, \quad q_2(y') = \frac{\tilde{p}_2(y')\, I(0 \leq y' \leq b')}{\int_0^{b'} \tilde{p}_2(u)\, du} \tag{3.16}$$

In our example we have chosen $a = 2000$ and $b' = 1000$. For the current FEE configuration, $t = 3500$.

We have introduced four parameters to be estimated from the data. The scale factor M is used to convert from ADC2 to ADC1 units. The parameters μ and σ characterize the underlying charge distribution. Finally, ρ_2 represents the degree of smearing in the coarse-grained scale. The analogous parameter ρ_1 in the fine-grained scale is entirely due to pedestal subtraction and so is known empirically. In addition the mean pedestals η_1 and η_2 are assumed given.

The number of free parameters can be reduced by introducing a constraint. We want the integrated areas of the fitted spectra in the two regions to be proportional to the observed number of counts there. We require

$$\frac{\int_a^t \tilde{p}_1(x)\, dx}{\int_0^{b'} \tilde{p}_2(y')\, dy'} = \frac{N_1}{N_2} \tag{3.17}$$

where N_1 is the number of counts in ADC1 and N_2 is the number of counts in ADC2. In the calculation of the likelihood this constraint is implemented as $\mu = \mu(\sigma, M, \rho_2)$.

Estimation of the scale factor and the other undetermined parameters is accomplished by fitting the data by maximum likelihood to the shapes described above. We use the

log-likelihood $\ell(\sigma, M, \rho_2) = \ell_1 + \ell_2$, with

$$\ell_1 = -N_1 \ln \sigma_1' - \sum_i \frac{(x_i - \mu_1')^2}{2\sigma_1'^2} + \sum_i \ln F_{\tilde{\mu}_1, \tilde{\sigma}_1}(-x_i) - N_1 \ln Q_1 \tag{3.18}$$

$$\ell_2 = -N_2 \ln \sigma_2' - \sum_j \frac{(y_j - \mu_2')^2}{2\sigma_2'^2} + \sum_j \ln \left[1 - F_{\tilde{\mu}_2, \tilde{\sigma}_2}(-M\sigma^2(y_j' + \eta_2))\right] - N_2 \ln Q_2 \tag{3.19}$$

where Q_1 and Q_2 are the respective denominators of $q_1(x)$ and $q_2(y)$ in Eq. 3.16. Although ℓ_1 depends explicitly only on σ and not on ρ_2 or M, there is an implicit dependence on these parameters through μ, which is calculated from the constraint equation.

Our strategy is to make reasonable first guesses for the parameters. We then maximize only ℓ_1 to arrive at an improved estimate of σ and μ. Usually we find that these parameters are insensitive to reasonable starting values of ρ_2 and M. Next, we use the improved μ and σ to minimize ℓ_2, varying only M and ρ_2. We then use these improved guesses to minimize the total likelihood.

As mentioned at the beginning of the previous section, different PMTs experience different light levels. In some cases the charge spectrum is entirely in the low range or entirely in the high range. For such channels we cannot use this method to calibrate the relative ADC scale. In a dedicated calibration, it is probably necessary to apply the algorithm to different runs in which the light source is moved around. In order to make sure that both ADCs are occupied with similar frequencies, we demand that neither scale contain fewer than 10% of the total ADC counts ($N_1, N_2 \geq 0.1N$). Since we fit within a window $a = 2000 \leq x_{\mathrm{ADC1}} < 3500$ and $0 \leq y'_{\mathrm{ADC2}} \leq b' = 1000$, only ADC values in these ranges are counted towards N_1 and N_2. Also we demand that the combined spectra have at least 500 counts ($N \geq 500$).

To demonstrate the algorithm, we apply this method to Run 5197. Restricting our attention to the channels satisfying the requirements above, we calculate the maximum likelihood estimate of the scale factor for 58 out of 192 channels. Examples of the fitted spectra are shown in Fig. 3.14. A cursory inspection by eye seems to indicate that the fitted spectrum in ADC1 is poorer when the mean μ falls in ADC2. Overall the fit seems more

impressive when we remember that *both* spectra are fit with only three free parameters, one more parameter than we might use to fit a single spectrum to a gaussian.

Next we pursue a complete calibration of all FEE channels. For this we consider the following sets of LED intensity scans from the Dry Run 2: Runs 5514-5569, Runs 5587-5616, Runs 5619-5646, Runs 5647-5758, Runs 6318-6349, Runs 6350-6381, and Runs 6397-6413. Altogether this amounts to 307 runs with the LED intensity varied from one run to the next and the LED position varied from one set of runs to the next set. In all, the calibration algorithm was executed 1433 times, and 191 out of 192 channels were calibrated at least once. Our hope is that by looking at so many runs, most or all of the PMTs will have a chance to satisfy the requirements of the calibration algorithm.

To estimate the quality of the fits, we bin the data and calculate separate chi-squared values for each of the two spectra. We exclude from consideration any fits with chi-squared/dof > 2 for ADC1 or chi-squared/dof > 4 for ADC2. This leaves calibrations for 185 channels, with an average of 6.0 calibrations per channel. The most calibrations per single channel is 10, and the minimum is 1.

For each FEE channel the mean of each calibration parameter was computed. The average values of each of the parameters are: $\langle\mu\rangle = 3501.1$, $\langle\sigma\rangle = 327.1$, $\langle\rho_2\rangle = 5.0$, and $\langle M\rangle = 18.7$. In addition, we have calculated the average value of $\sqrt{\rho_2^2 - \sigma_{\eta_2}^2}$, a measure of the jitter of ADC2 without the pedestal contribution σ_{η_2}, also to be 5.0. In other words, the smearing in ADC2 is largely due to this jitter rather than due to pedestal subtraction, a fact we could already discern just by looking at Fig. 3.11.

Where there are at least two observations, the standard error of each parameter is also computed. The means of the standard errors for each parameter over all channels are: $\langle\Delta\mu\rangle = 97.4$, $\langle\Delta\sigma\rangle = 17.4$, $\langle\Delta M\rangle = 0.09$, and $\langle\Delta\rho\rangle = 0.27$. The large standard errors of the mean and width of the ADC distribution are simply due to the varying relative occupancies of the two ADCs for different FEE channels, and therefore we have no reason to expect that this parameter should remain stable.

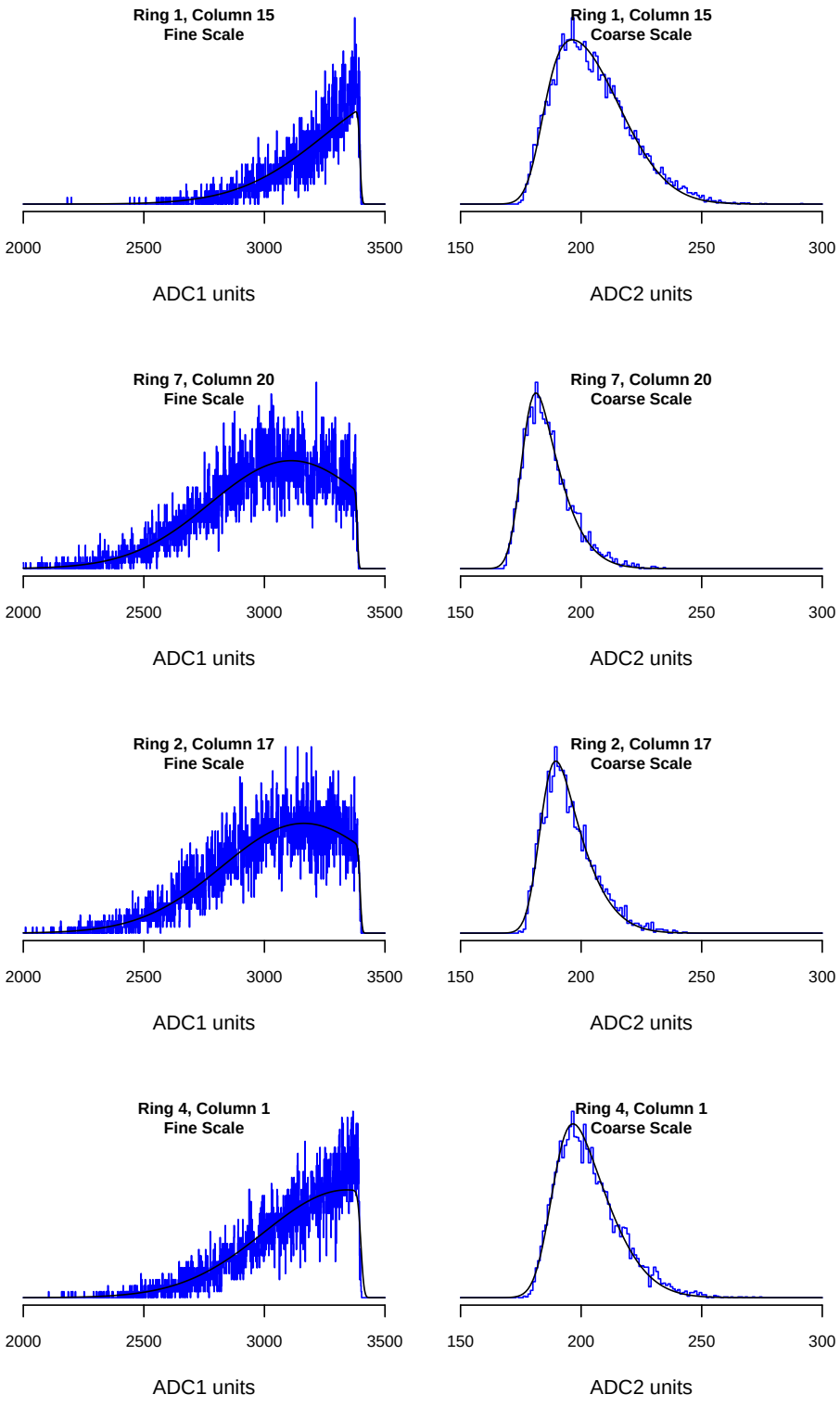

Figure 3.14: Fitted ADC1 and ADC2 spectra for four FEE channels.

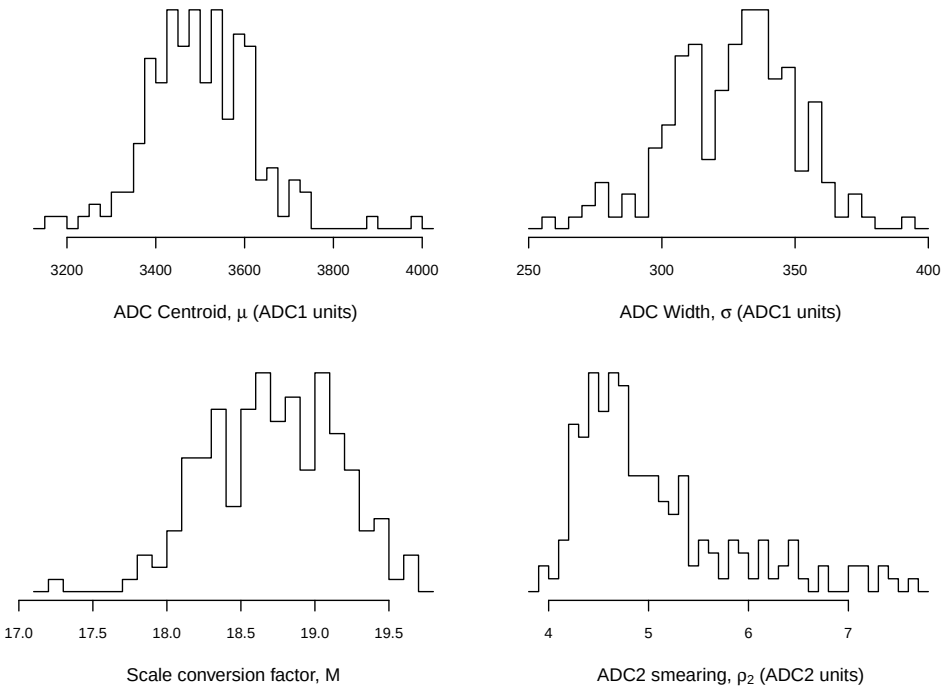

Figure 3.15: Distributions of fit parameters for 185 FEE channels.

Table 3.2: Correlations of fit parameters.

σ	0.436		
ρ_2	0.056	-0.305	
M	-0.022	0.261	-0.647
	μ	σ	ρ_2

The distributions of the fitted parameters are shown in Fig. 3.15. The distribution of the scale factors in the lower left plot shows a roughly bell-shaped curve with no extreme outliers. The mean is around 18.7, in good agreement with the rough value of 19 reported by the FEE group. The standard deviation is 0.43, or about 2.3% of M. It is this variation in the ADC2 scale that we are trying to correct through calibration. The smearing parameter ρ_2 shows a long tail toward the right, perhaps implying a few noisy channels in which the jitter is more than average. The correlations of the fit parameters with each other are shown in Table 3.2. The dominant correlation is that between M and ρ_2. It appears that the jitter in ADC2 decreases with larger M.

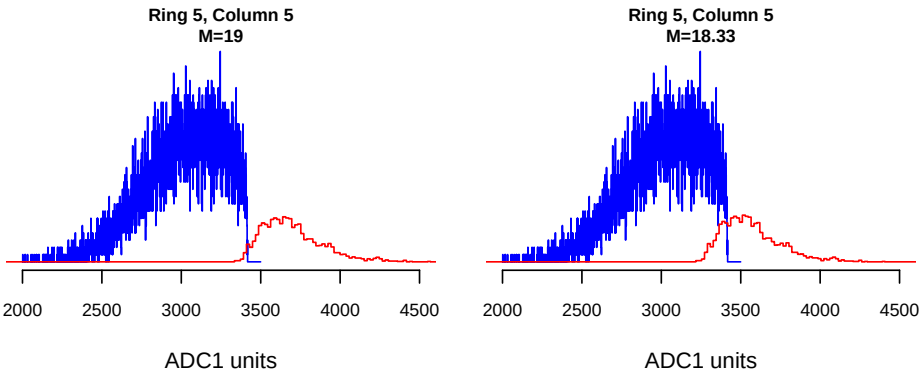

Figure 3.16: ADC1 (blue) and ADC2 (red) spectra presented on the same scale after conversion by Eq. 3.8. The left plot uses the "default" value of $M = 19$, while the right plot uses the calibrated value.

3.3.1.4 Linearity

The formula given at the beginning of this section indicates a simple linear relationship between ADC units to charge. In practice, the PMT response may be nonlinear. It is important to characterize these effects because of their impact on energy resolution.

At the low end of the ADC scale, some amount of the total charge is lost due to the FEE threshold. When the threshold is set at a low value, almost every PMT hit is captured, but the data are inundated with noise. As the threshold is raised, low-charge noise disappears at the expense of signal efficiency. A simple simulation using realistic values for the gain and single-photoelectron distribution indicates that the detectors should see a 0.3% reduction in deposited charge for a 1-MeV signal when the threshold is set at one third of a photoelectron [145].

For higher-energy signals the threshold effect is less important, and the main cause of nonlinearity is PMT saturation. This effect limits the dynamic range of the detectors. High-energy muons, for example, may saturate the detector's energy response. A number of methods have been proposed to quantify this effect. For example, one may feed the PMT a signal from a generator and measure the integrated charge on an oscilloscope. If q_1 and q_2 are the charges from two separate pulses and q_{1+2} is the charge from the combined pulses, one measure of the nonlinearity is

$$\text{nonlinearity} = \frac{q_{1+2} - (q_1 + q_2)}{q_1 + q_2}$$

One of the challenges with this kind of measurement is that the presence of overshoot and ringing in the PMT waveform complicates the calculation of the peak area. Other studies of nonlinearity make relative measurements comparing each PMT with the average response of its neighbors or to one of the 2" reference PMTs. For the most part, these studies show that the PMTs are linear up to about 400 photoelectrons.

Even the front-end electronics may contribute to the nonlinearity. Various upgrades were

made to the FEE boards to improve this until the nonlinearity was brought to about 0.5%. The FEE has a self-test function for measuring the nonlinearity. A sequence of square-wave signals of increasing amplitude are fed into the FEE channels. The nonlinearity of the response may be calculated from the output.

Although nonlinearity measurement has been a focus of considerable effort, corrections can actually be performed downstream in the analysis as part of the energy reconstruction. For this reason the correction is not applied at the calibration stage of the analysis.

3.3.2 PMT Time Calibration

While vertex reconstruction algorithms rely on the charge pattern within the detectors, it is still necessary to calibrate the timing of PMT signals. Timing cuts are used for data reduction and in the selection of IBD events, and so it is important to synchronize the timing of PMT channels. If PMTs were perfectly calibrated and responded instantaneously to signals, then we would have $T_{\text{meas}} = T_0$, where T_{meas} is the TDC measurement and T_0 is the real time of the physical signal. In practice, $T_{\text{meas}} - T_0 = \Delta$, where Δ is a timing offset correction.

The most obvious source of this correction is simply the geometry of the AD: different PMTs are at different distances from the source. The time-of-flight correction, t_{TOF}, is a few nanoseconds. Unless each time correction is based on the reconstructed vertex of the source, t_{TOF} remains part of the timing uncertainty.

The PMTs have an intrinsic time offset related to the transit time of photoelectrons through the dynode chain, the response of the FEE boards, etc. This bias, t_{PMT}, can be calibrated out of the timing response. There is also an energy-dependent timing correction, t_E, that we call the time walk. The time walk has two causes. The first is statistical: when many photons are detected, the expected first-hit times in each channel occur earlier in time. The second cause has to do with the pulse shape. A large PMT pulse will cross the

FEE threshold at an earlier time than a smaller pulse. Thus t_E is a decreasing function of deposited energy. It too can be calibrated out.

Since $\Delta = t_{\mathrm{TOF}} + t_{\mathrm{PMT}} + t_E$, we may perform a relative PMT timing calibration by estimating $t_{\mathrm{PMT}} + t_E$ for each channel [146]. Subtracting this correction from measured TDC values improves the timing uncertainty.

3.4 Reconstruction

3.4.1 Energy Reconstruction

The conversion from deposited energy to a detector signal depends on many factors. Calibration accounts for differences in PMT gain, quantum efficiency, and discriminator thresholds. However, there remain effects in the energy response due to the detector geometry (e.g. top-bottom asymmetry, solid angle effects, light attenuation lengths) and due to the physical processes themselves (different scintillation spectra in different media, light quenching, multiple primary photons). Finally, statistical effects also serve to smear out the energy response of the detectors. It is the goal of energy reconstruction to convert the calibrated charges to physically meaningful energies.

To illustrate the geometric dependence, we have constructed a simple deterministic light propagation model [147]. Each PMT is modeled as an oblate spheroid of major radius 10.10 cm and minor radius 7.37 cm, with the photocathode only partially covering one hemisphere (contact-lens shape), extending out to a radius of 9.5 cm. We calculate the fraction of the light incident on the PMT as the surface integral

$$\int_{\rho=0}^{\rho_m} \rho \, d\rho \int_{\phi=0}^{2\pi} d\phi \, e^{-\ell/L} \times \left(\frac{1}{4\pi\ell^2} \sqrt{1 + \frac{\rho^2}{R^2 - \rho^2} \left(\frac{R}{r} \right)^2} \times \cos\theta \times \Theta\left(\cos\theta\right) \right) \tag{3.20}$$

where ρ_m is the cathode radius, $\ell = \ell\left(\rho, \phi\right)$ is the path length, L is the attenuation length, R

and r and the major and minor radii of the PMT, and $\theta = \theta(\rho, \phi)$ is the angle with respect to the PMT normal. Note that ℓ and ϕ vary over the surface of the PMT and also depend on the source position. The Heaviside Θ-function is included to ensure that only light hitting the front of the PMT is counted; rays with $\theta > 90°$ will be shadowed. Reflections off the top and bottom panels are treated by adding image sources at appropriate positions. Given the location of the light source, we can solve this integral numerically for each of 192 PMT positions. Summing the results, we find that the total light yield in the target volume may vary by several percent, depending on the source position, as shown in Fig. 3.17. In addition, this model has been used to show that random PMT displacements on the order of 1 cm can affect the total light yield by $\sim 0.1\%$ [148].

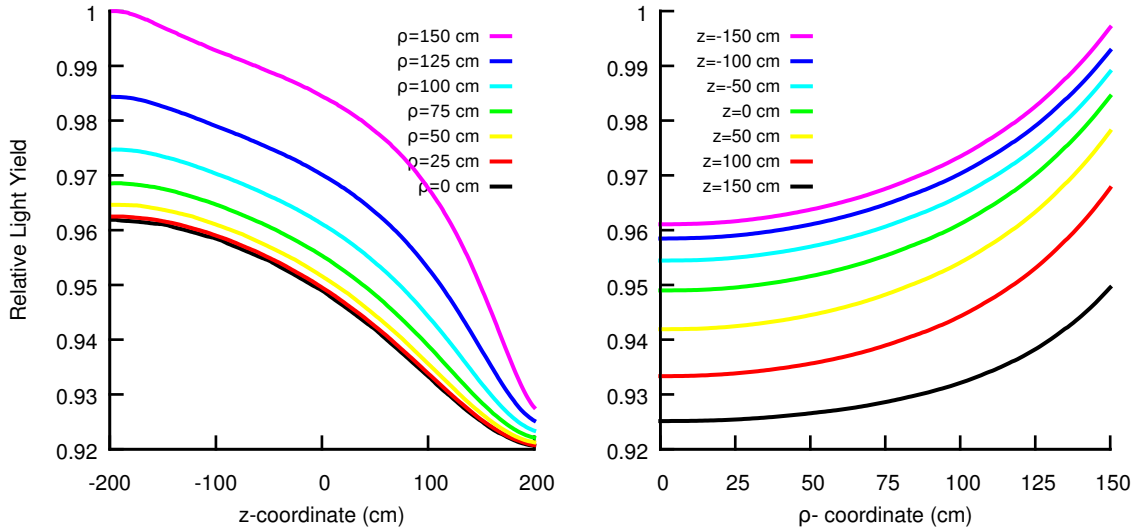

Figure 3.17: Geometric dependence of total light yield in a single antineutrino detector module using a deterministic model.

Quenching is the loss of light in the scintillator due to the conversion of energy to other degrees of freedom. The amount of light quenching depends on particle type, but the particle

ID is not used in the energy reconstruction. The effect can be described empirically by Birk's law [32]:

$$\frac{dS}{dr} = A\frac{dE/dr}{1 + k_B\, dE/dr} \tag{3.21}$$

where S is the luminosity of the scintillator and dE/dr is the amount of energy deposited by the charged particle per path length traversed. The energy loss dE/dr depends on the particle, while A and k_B are properties of the scintillating material. Birk's constant k_B has been measured for the Daya Bay scintillator [149]:

$$\begin{aligned} \text{Gd-doped liquid scintillator} \qquad & k_B = (6.489 \pm 1.058) \times 10^{-3} \\ \text{undoped liquid scintillator} \qquad & k_B = (8.205 \pm 1.231) \times 10^{-3} \end{aligned}$$

Rather than treating these effects individually, the energy scale is simply calibrated with ^{60}Co, ^{68}Ge, and AmC sources weekly. The energy scale has been observed to drift as much as 0.5% per week [150]. The time dependence may be due to changes in the PMT gains, FEE channel efficiency, and optical properties of the liquid scintillator [151], all of which may be caused by temperature fluctuations in the detector halls. Spallation neutron capture on Gd can be used as a check of the energy calibration.

Energy reconstruction begins by directly converting the calibrated charge to energy, using the ^{60}Co source to define the conversion factor. The Daya Bay antineutrino detectors measure about 170 photoelectrons per MeV of visible energy.

To calibrate the geometry dependence, the radioactive sources are placed at 15 vertical positions along three axes. The charge-weighted (or center-of-gravity) source position is given by $\vec{x}_{\text{cog}} = \sum Q_i \vec{x}_i / \sum Q_i$, where Q_i is the charge measured by the ith PMT and $\vec{x}_i$ is its position. The sum is over 192 AD PMTs. This vector is converted to cylindrical coordinates, and the real source position is fitted to the charge-weighted position, giving a temporary vertex reconstruction:

$$\begin{aligned} R &= 1.82 R_{\text{cog}} - (1.95 \times 10^{-4}) R_{\text{cog}}^2 \\ Z &= \left[Z_{\text{cog}} - (1.579 \times 10^{-7}) Z_{\text{cog}}^3\right] \times \left[3.128 - (9.64 \times 10^{-4}) R_{\text{cog}}\right] \end{aligned} \tag{3.22}$$

Finally, these values are used to fit a vertex-correction factor [152]:

$$f(R,Z) = (1 + C_R \times R^2)(C_{Z1} + C_{Z2}Z + C_{Z3}Z^2 + C_{Z4}Z^3) \tag{3.23}$$

where

$$C_R = 3.3762 \times 10^{-8},\ C_{Z1} = 1.0005,\ C_{Z2} = -1.002 \times 10^{-5},$$
$$C_{Z3} = -1.894 \times 10^{-8},\ C_{Z4} = -1.758 \times 10^{-13}.$$

All coordinates are given in centimeters. After the position correction is applied, the energy is corrected for the nonlinearity of the detector energy response (see Fig. 3.18).

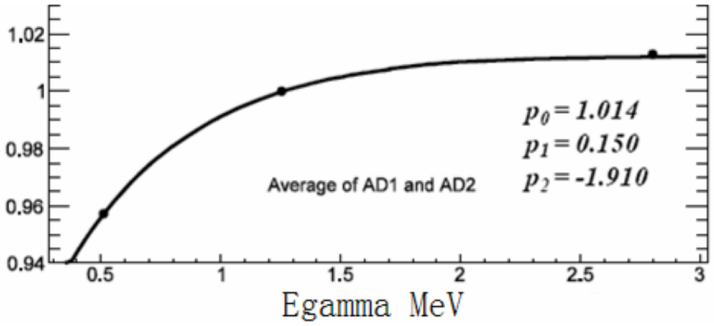

Figure 3.18: Nonlinearity of the detector energy response [153].

Using the isotopic abundances we can estimate the energy resolution at 8 MeV by fitting the spallation neutron peak to the sum of two gaussians:

$$f(E) = A\left[N(\mu_1, \sigma_1) + 0.2231N(\mu_2, \sigma_2)\right] \tag{3.24}$$

The results of the fits for two Daya Bay near site ADs are shown in Fig. 3.19. The relative

amplitudes of the two peaks are constrained by the abundances and relative cross sections. Averaging the values of $\sigma/\sqrt{E}$, we can estimate a crude scaling of the energy resolution: $\sigma(E) = 0.098\sqrt{E}$. We neglect the constant term in this expression. This back-of-the-envelope calculation is consistent with a 5% uncertainty for the IBD positron energy at 4 MeV.

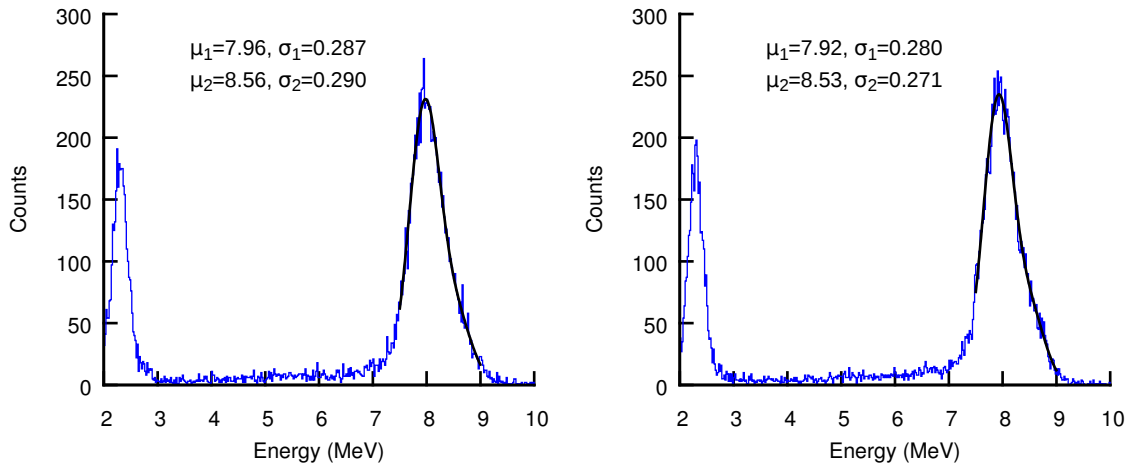

Figure 3.19: Fit of the 8 MeV peak for spallation neutrons to the sum of two gaussians. On the left is AD1; on the right is AD2. The relative energy resolution σ/E at 8 MeV is approximately 3.4%.

3.4.2 Vertex Reconstruction

Three methods have been developed to reconstruct particle vertices. The first of these is a maximum likelihood fit [33] to a model similar to that described above, except that no integral over the curved photocathode surface is performed. Since the PMTs are relatively far from the target volume, a simple $\cos\theta$ dependence of the light yield is a fair approximation to the integral. The algorithm has the disadvantage that the minimization tends to be slow.

A faster method simply fits the charge-weighted vertex to the true vertex using simulated

data. The charge center $\vec{x}_{\text{cog}}$ itself is not a good estimate for the true vertex. Low-energy events whose energy is primarily deposited in a small number of PMTs tend to be reconstructed very close to the AD walls, while high-energy events that illuminate the PMTs uniformly are reconstructed toward the center of the AD. In addition, the z-coordinate of the charge center is constrained to lie between the planes of the top and bottom PMT rings. These biases can be removed by using an energy-dependent map $\vec{x}_{\text{cog}} \rightarrow \vec{x}_{\text{rec}}$.

Inverse beta decay events were simulated, and the charge centers of the positrons were compared to the true vertices. The position-dependent bias of the positron signal is estimated by binning the detector in z and r^2 and averaging the residuals in each bin:

$$\text{Bias}(\vec{x}_{\text{cog}})_{\text{bin } i} = \text{Average}\left[\sum_{\vec{x}_{\text{true}} \in \text{bin } i} (\vec{x}_{\text{cog}} - \vec{x}_{\text{true}})\right] \tag{3.25}$$

Having histogrammed the average residuals in this way, the charge-center vertex can be corrected by subtracting the bias. To improve the resolution and smooth the effects of binning, the bias correction is interpolated between the grid points.

The third method of vertex reconstruction, and the one currently in place for most analyses, is the so-called charge template method [154]. Instead of starting from the charge center, the response of each PMT is individually taken into account. Half a million IBD events were simulated, and the mean response of each PMT was recorded for a 20×20 grid of $\vec{x}_{\text{true}}$. Each grid square is called a "template". A chi-squared function is used to compare the real distribution of charge over the PMTs with each of the 400 templates. Once again, interpolation is used to pinpoint the minimum between the grid squares. This method is found to give a radial resolution of 7 cm for IBD positrons and 18 cm for IBD neutrons, and a vertical resolution of 9 cm for IBD positrons and 20 cm for IBD neutrons [155]. The poorer resolution for the neutrons is due to the fact that the neutron capture releases two primary γs, smearing out the position resolution. Another factor is that the neutrons drift for some distance before they are captured.

3.5 Singles

Most of the events satisfying the trigger criteria are not related to the IBD signal. Although some of the backgrounds can produce multiple triggers that are correlated in time, most of the DAQ readouts are single events isolated in time from other triggers. It is also possible for independent triggers with no causal relationship to form time coincidences by mere chance. These accidental triggers will be discussed in a later section.

The complex spectrum of the single triggers merits some study. Many of these backgrounds come from uranium, thorium, and potassium decay chains, and data for these isotopes have been used to fit the singles spectrum [156]. These contaminants may arise from construction materials, PMT glass, and from the scintillator itself. This is shown in Fig. 3.20.

Not all of the single triggers correspond to physical backgrounds. PMT dark noise, which depends on temperature, may contribute to the singles rate. Because it is unlikely for many PMTs to fire simultaneously due to chance, dark noise should not pass the multiplicity trigger. Electronics noise, especially in the wake of a high-energy event such as a showering muon, may also affect the trigger efficiency. As already mentioned, the PMTs may exhibit pulse "overshoot", ringing, and afterpulses as they return to a stable baseline. We have also observed noise from loose connectors and from the power supply line. One of the more persistent sources of noise in our detector was a 300-kHz signal that was ultimately traced back to the cameras of the safety monitoring system [157]. These were powered off and the noise disappeared. The trigger rates are monitored in real time by the ODM. The trigger rate per AD is usually about 280 Hz, and the rate in the inner/outer water shields is about 150/200 Hz. A back-of-the-envelope calculation indicates that the prompt-like singles rate is known to a relative uncertainty of 0.0044% (stat) $+ 0.176\%$ (sys). The delayed-like singles rate relative uncertainty is 0.25% (stat) $+ 0.04\%$ (sys) [158].

The singles rate (usually defined as those events passing energy, muon, and flasher cuts,

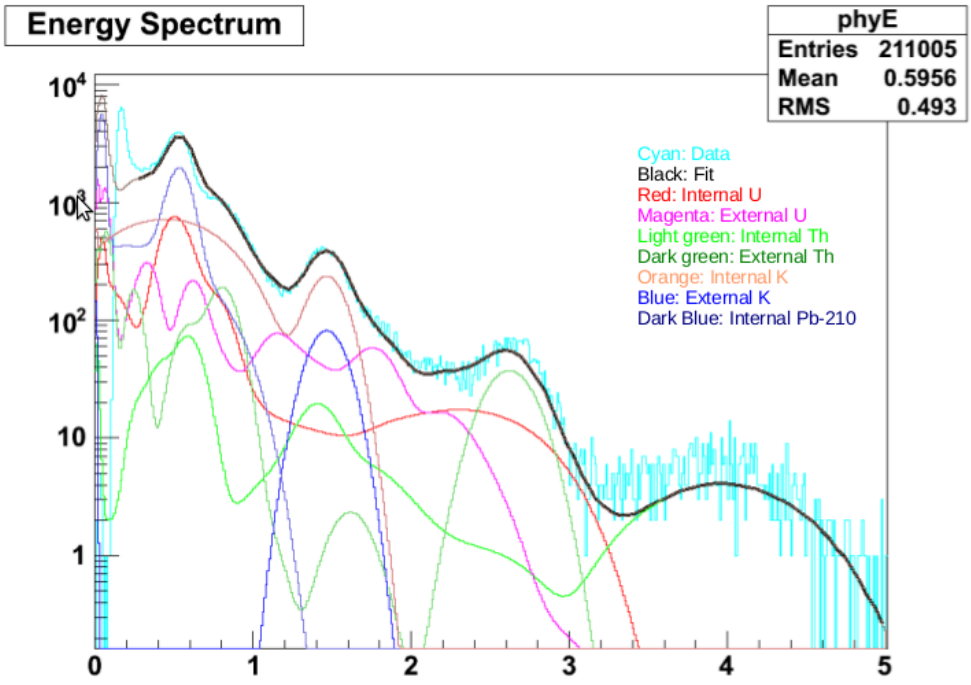

Figure 3.20: Singles spectrum from uranium, thorium, and potassium decays [156].

which will be described) is not constant in time as one might expect. The singles rate in the AD has been observed to decrease with a half life of 25 days, indicative of radioactive contamination [159]. A trigger rate discrepancy of the inner and outer water shields also shows a decay with time and has a rate consistent with radon contamination. Radon daughters can excite dissolved N_2, which then releases light upon de-excitation [160, 161].

The singles spectrum after muon and flasher cuts, which will be described, is shown in Fig. 3.21. The figure is intended to convey the very similar performance of the first two AD modules that were deployed at the Daya Bay near site. Their singles spectra are nearly identical.

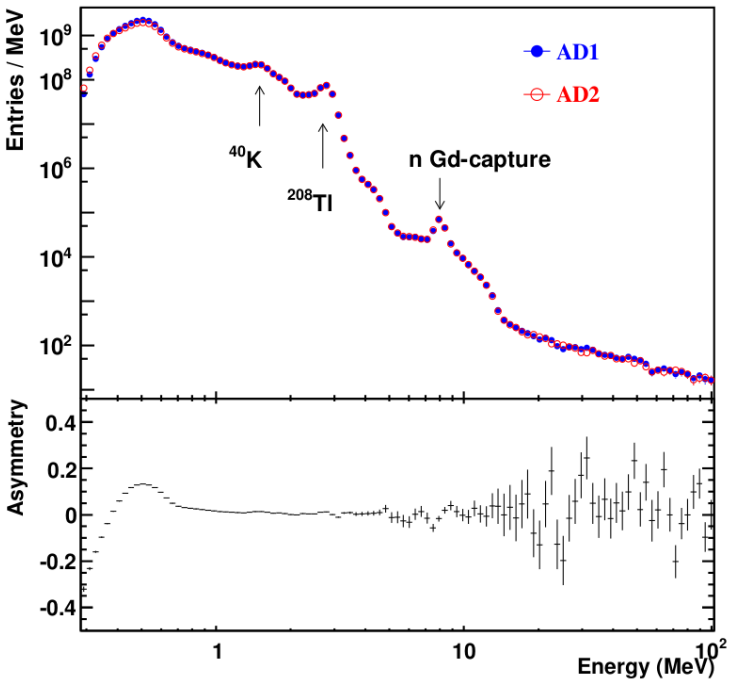

Figure 3.21: Singles spectrum in two ADs after muon and flasher cuts [27].

3.6 Muon Backgrounds

Atmospheric muons are responsible for many of the backgrounds in our data. Muons passing through the ADs are easily detected by the scintillation light they create. Muons passing through the water shield are detected from their Čerenkov radiation, electromagnetic radiation generated when a charge particle passes through a medium with velocity greater than the speed of light in the medium.

Short-lived radioactive isotopes induced by the muons may contribute to the singles rate. Neutrons from muon spallation (nuclear breakup) can occur in coincidence with these singles to create triggers that satisfy the IBD cuts. Longer-lived isotopes such as ^{9}Li can also mimic the IBD signal. These categories of backgrounds will be treated in following sections, but first in this section we consider the muons themselves.

Site	Overburden (m.w.e.)	Muon flux (Hz/m^2)	Average energy (GeV)
Daya Bay	280	1.27	57
Ling Ao	300	0.95	58
Far	880	0.056	137

Table 3.3: Overburden and muon rate at each site as expected from simulation [2].

To minimize backgrounds due to cosmic rays, the Daya Bay detectors are situated within the 700-m high Páiyá Mountain (排牙山), which provides a large overburden as shown in Fig. 3.22. The overburdens are given in Table 3.3, and the density of the rock surrounding the sites is about 2.60 g/cm^3. Using these values, the propagation of cosmic muons through the mountain was simulated to estimate the flux at each of the detector sites. Gaisser's empirical formula for muon flux, modified to correct for differences at small zenith angles, was used to model the atmospheric muon flux [1]. The mountain topography discretized as a 4 km $\times$ 3 km rectangle of 150,000 grid points. The results of this calculation are used as inputs to the muon generator. Fig. 3.23 illustrates the energy distribution of muons.

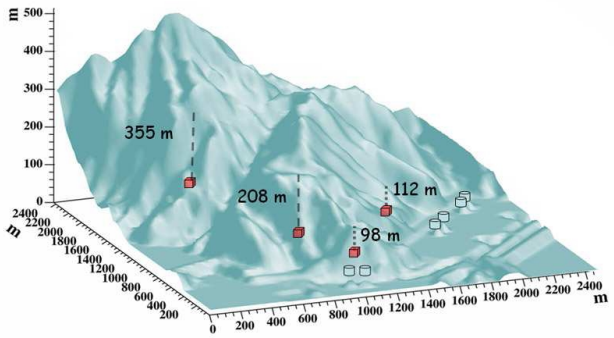

Figure 3.22: Topology of mountain wherein the Daya Bay antineutrino detectors are situated.

As an interesting example of physics outside the main thrust of the experiment, it is

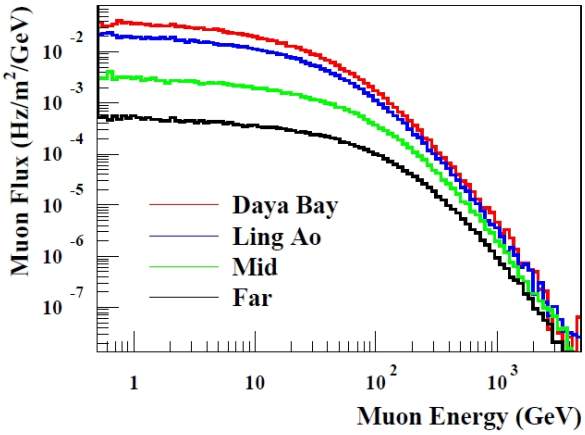

Figure 3.23: Simulated flux of muons at the various sites.

possible to study those muons that decay within the fiducial volume [162], so-called stopped muons. These tend to be low energy muons that nevertheless produce large prompt signals. By detecting the Michel electron associated with the muon decay the muon lifetime in AD1 is measured to be 2.064 ± 0.035 μs.

Muon Veto

In addition to their function of shielding the ADs from external radioactivity, the water pools' second purpose is to aid in tagging muons based on their Čerenkov light. A water pool muon is any trigger that causes more than 12 PMTs to fire in either the inner water shield or the outer water shield, i.e. ($\mathrm{NHIT_{IWS}} > 12$ OR $\mathrm{NHIT_{OWS}} > 12$). In the ADs, the muon tag is a simple energy cut. This is not very sophisticated and allows muons that do not deposit much energy in the water pool to go untagged, but the inefficiency is weighed against the simplicity of estimating the impact of the muon tag on the IBD detection efficiency. An AD muon is defined to be any trigger with a reconstructed energy greater than 20 MeV in

either AD. A showering muon is defined as any trigger with a reconstructed energy greater than 1 GeV. The RPCs may provide for some redundancy in the future, but at this time they are not being used in the analysis.

That these cuts are arbitrary is seen from Fig. 3.24. A bump between 500 MeV and 1 GeV is due to minimal ionizing muons, which deposit roughly 2 MeV/cm [163]. The distribution tails off to about 3 GeV, where the ADCs are saturated. That is, the coarse ADC scale for all channels has reached its maximum value, at which all higher muon energies are truncated. The NHIT distributions for the water pool muons are shown in Fig. 3.25. The structure here is due to the complex geometry of the pool. The presence of counts with NHIT below 12 is due to the fact that the pool muon need only have NHIT > 12 in either the IWS *or* the OWS; the other water shield may have a lower firing multiplicity.

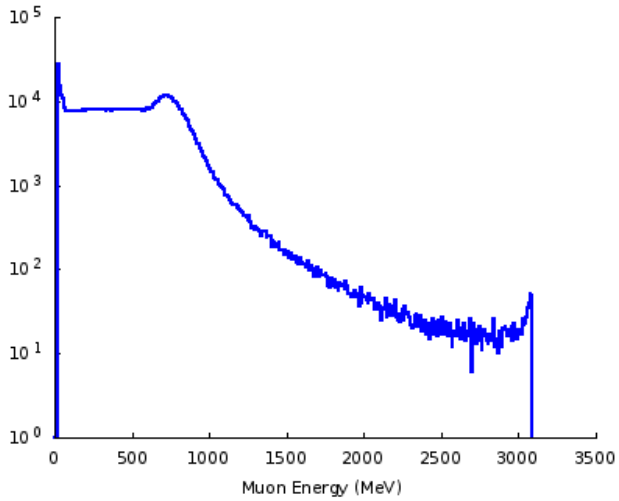

Figure 3.24: Energy distribution of AD muons (i.e. triggers with energy greater than 20 MeV).

The efficiency of the water pool may be defined as the ratio of the number of muon tags to the number of muons with nonzero path length in the water shield. One way to estimate

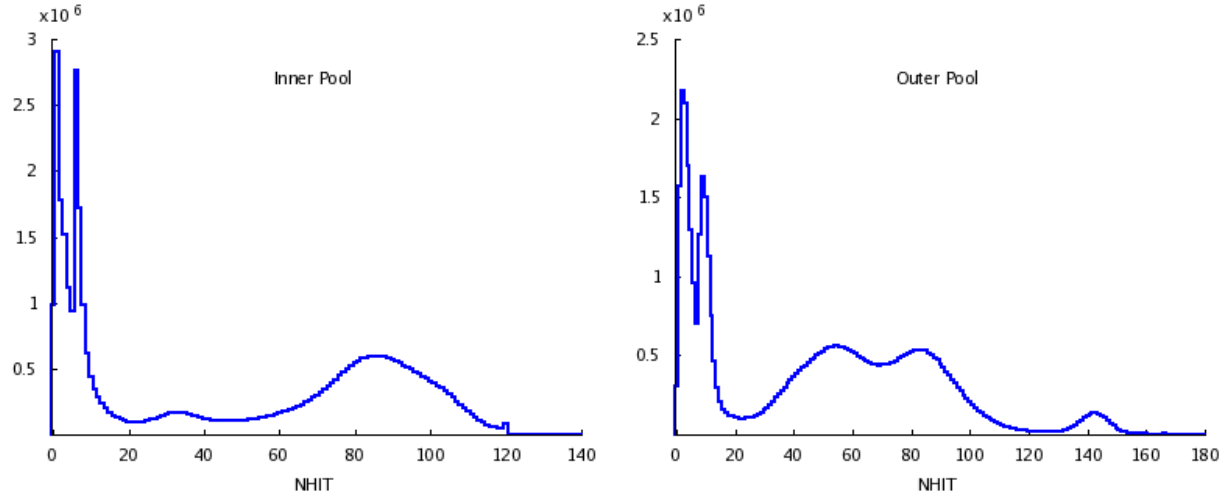

Figure 3.25: NHIT distribution of water pool muons.

the efficiency is to find the fraction of events tagged by one water shield that are not tagged by the other water shield. This approach is crude, but it has become the accepted measure of muon efficiency. One particular criticism of this approach is that muons passing through the outer water shield do not necessarily pass through the inner water shield and therefore should not be counted against its efficiency. In any case, the quoted efficiency of the outer water shield is $97.1 \pm 0.2\%$ and for the inner water shield it is $99.98 \pm 0.02\%$ [164].

Many of the inefficient events, those muons that pass through the water pool but do not satisfy the pool muon tag, are "corner clippers", muons with a short track segment in the pool. Though these events are likely to be missed, they also have a large impact parameter with respect to the ADs and are therefore less likely to create any background triggers within the liquid scintillator. Some efforts have been made to reconstruct the muon tracks but so far this is not applied in the analysis [165].

Once the muons have been tagged, it is necessary to remove any data that might be muon-induced. The high number of singles following a muon could easily create artificial

coincidences, and the most direct response is simply to remove this data from the analysis. Muon veto is applied during the IBD selection stage, removing all triggers withing 200 μs of a pool muon, 1 ms of an AD muon, and 1 s of a showering muon. (These veto periods are constantly being changed with every update to the analysis.) The effect on the IBD efficiency is taken as some fixed probability of missing IBD events due to a muon veto, but rather the muon veto is accounted for in the calculation of the detector livetime. This uncertainty in the livetime is estimated at 0.002% and is correlated among all ADs; i.e. it is not site-dependent.

Stopped Muons

Another possible source of backgrounds from muons involves muons that have lost sufficient energy that they effectively stop in the vicinity of the detector and are then captured on a nucleus. Positively charged muons decay into a positron, while the fate of negatively charged muons is nuclear primarily capture. The excited nucleus emits an Auger electron or undergoes prompt fission [166]. This process may produce a neutron that can then generate a fake IBD event in the same manner as a fast neutron from muon spallation. It has been proposed that Daya Bay can measure the number of neutrons emitted in each capture [167]. Of these, simulations have shown that the expected rate of such neutrons penetrating the target region and being captured are one capture per 170 years, far below the signal rate [168].

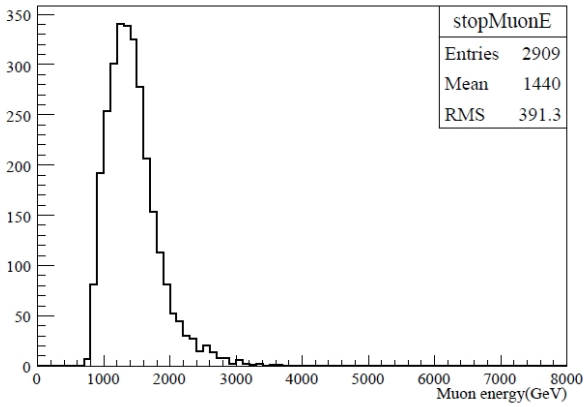

Figure 3.26: Energy distribution of muons stopped in the vicinity of the detector.

3.7 Flashers

We have described triggers due to external backgrounds and due to electronics noise, but some backgrounds may be due to the PMTs themselves. This "instrumental" background is due to spontaneous electric discharge at the PMT base. The light is visible by other PMTs as well as by the generating PMT, and the detector response may often pass the trigger conditions. We call such events "flashers". Many other experiments have observed flashing behavior in PMTs. Time exposure photographs reveal that the flashing arises on the PMT circuit boards [169]. It has been proposed that capacitors in the RC circuits spontaneously discharge with a given period; however, we have seen no evidence for the periodicity of flashing. A given PMT appears to flash at one or two fixed points on the circuit point, but this point differs from one PMT to another.

Although we claim that 5% of the PMTs are flashing PMTs [27], this is really an over-simplification. Tabulation of the flashing rate of each PMT shows that virtually all PMTs exhibit some degree of flashing, and although the flasher rate may vary by an order of magnitude or more, there is no clear line between flashing PMTs and non-flashing PMTs. Fig. 3.28 shows that the flashing PMTs tend to see a larger average charge and fire more often than

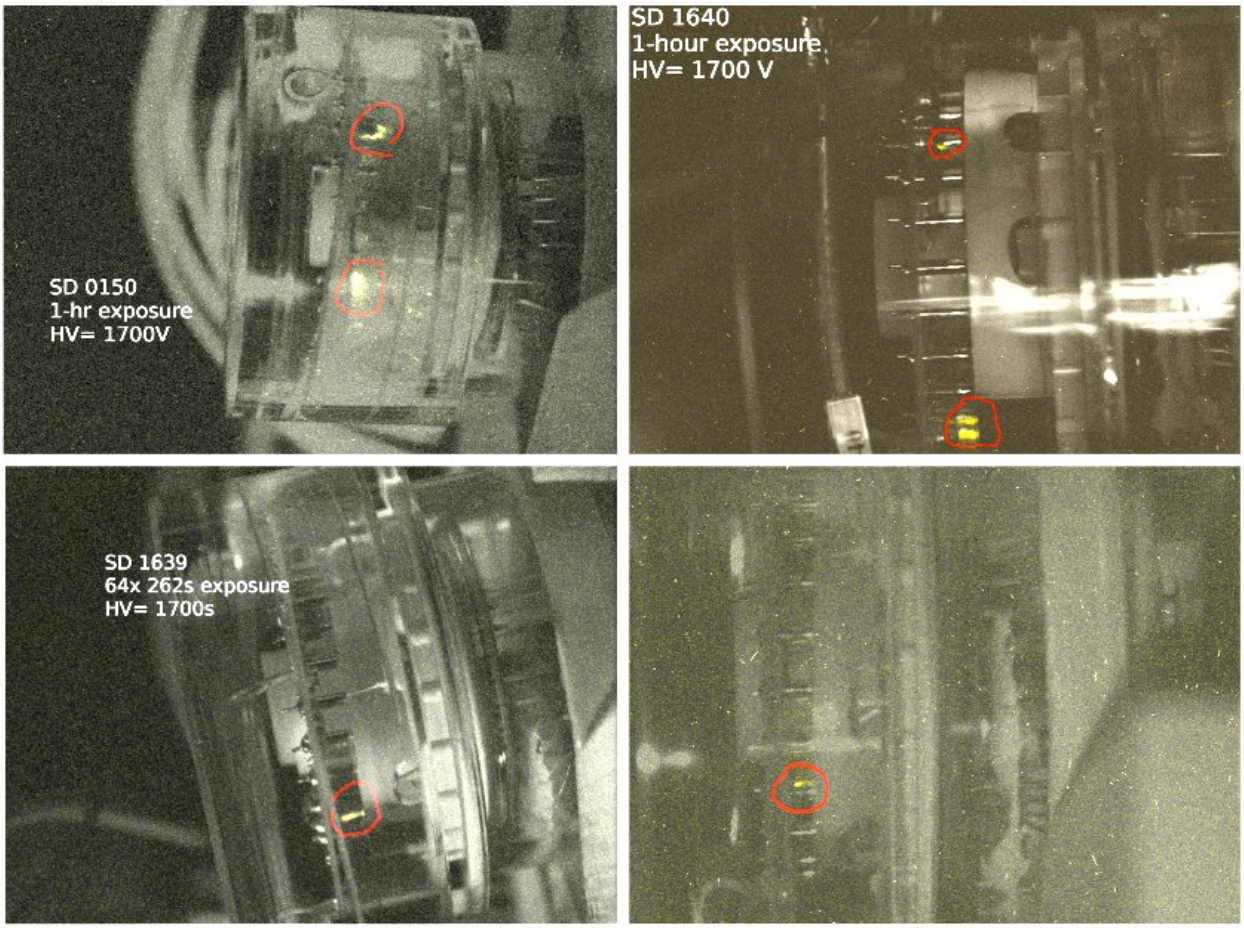

Figure 3.27: Time exposure photographs of PMT circuit boards in which the flashing is clearly seen [169].

nonflashing PMTs.

PMTs with high flashing rates have been studied with an oscilloscope. The PMTs are placed in a dark box with a small reference PMT used to distinguish flashing (visible in both PMTs) from dark noise (visible only in a single PMT). Pulses corresponding to flashes occur with a broad, double-peaked structure having a ragged oscilloscope trace. These pulses are generally larger than 10 photoelectrons (i.e. the integrated charge at the anode is $> 10Ge$, where G is the gain and e is the electron charge). The light intensity, as measured by the reference tube, is highest near the base of the PMT [170].

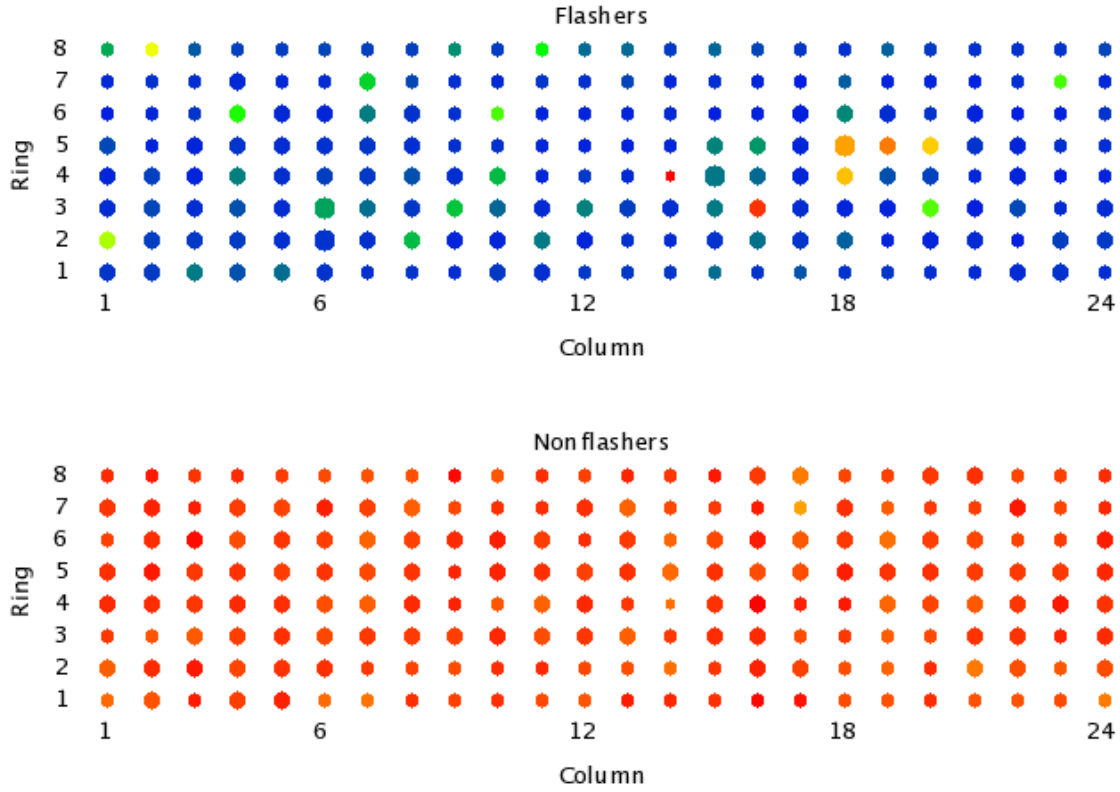

Figure 3.28: Bubble plot of all PMTs in a single AD. Top plot uses triggers tagged as flashers and bottom plot uses only triggers tagged as nonflashers. The size of each bubble indicates the fraction of triggers during which the given PMT fires, while the color represents the mean charge measured at each PMT when it does fire (red indicating higher charge).

The presence of flashers was initially revealed by the existence of regions of high density in the reconstructed vertices, as seen in Figs. 3.29 and 3.30. Because flashing occurs at a point, the corresponding reconstructed vertices are also very close to one another for a given flasher. However, because the vertex reconstruction is optimized for physical events and not these instrumental backgrounds, the vertex is not accurately reconstructed at the point of the actual flashing PMT.

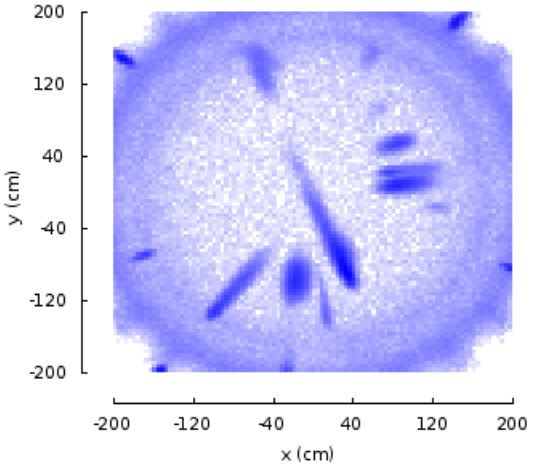

Figure 3.29: Top view of detector showing reconstructed vertices projected onto the horizontal plane. Cuts have been applied to select predominantly flashers, which tend to form vertex clusters.

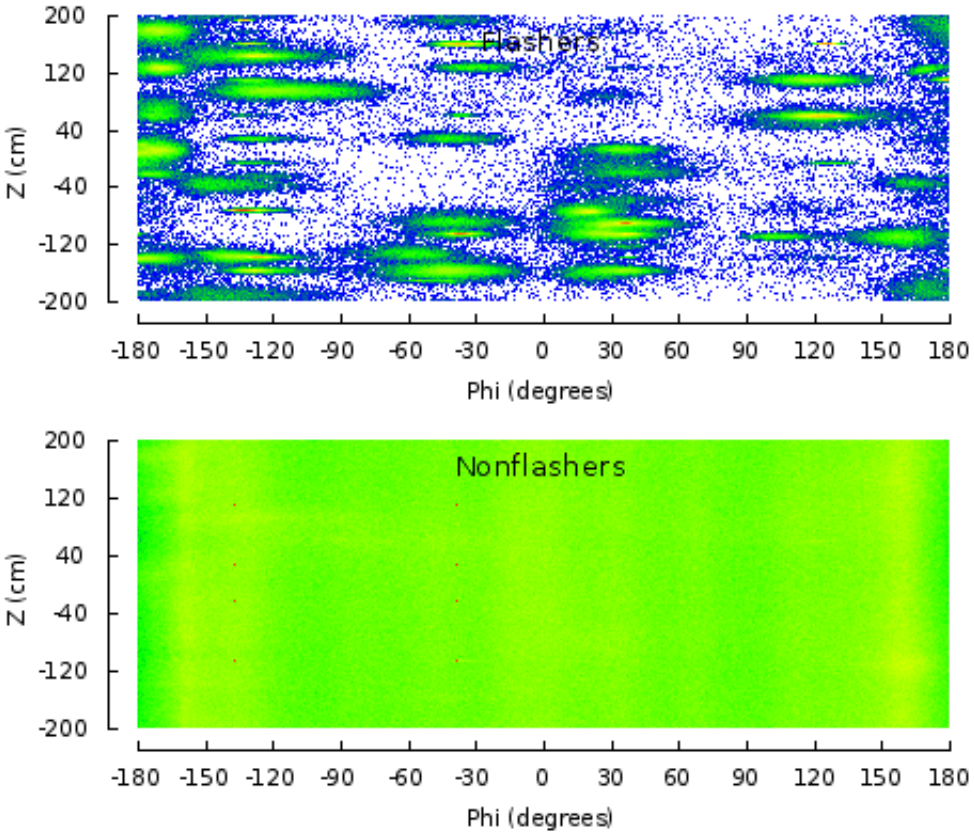

Figure 3.30: Wall view of detector showing reconstructed vertices projected onto the cylindrical wall of the AD. The clustering of the flashers is clearly evident.

Among the experiments also dealing with flashing PMTs, KamLAND observed that flashing PMTs exhibit a particular charge distribution. In a normal physical event, especially one that occurs in the fiducial volume, charge is distributed more or less uniformly. In a flasher, the flashing PMT often sees greater than 90% of the total charge, which may range from just passing threshold all the way up to 100 MeV [27]. By taking the ratio of the maximum PMT charge Q_{max} to the total charge Q_{tot} summed over all firing PMTs, one already finds some power to discriminate flashers from nonflashers. This is not sufficient, however, as the ratio $Q_{\text{ratio}} = Q_{\text{max}}/Q_{\text{tot}}$ does not neatly divide the set of all triggers into two groups (see Fig. 3.31). KamLAND used the Q_{ratio} variable and time information to construct a special event discriminator that effectively removed flasher triggers from their data, but the size and geometry of their detector made this an easier task compared with Daya Bay [171].

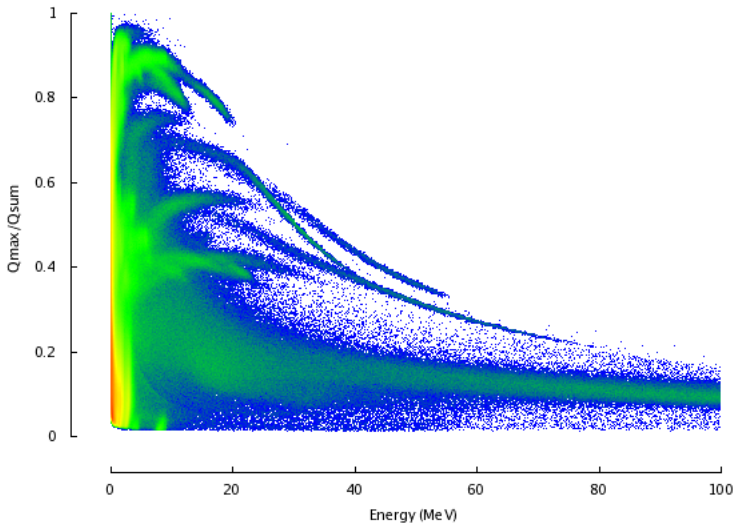

Figure 3.31: Ratio of max charge to total charge in the set of all firing PMTs versus reconstructed trigger energy. The lower-energy, higher fraction events tend to be flashers, while the main band sweeping along the bottom of the plot tends to be physical triggers. Unlike at KamLAND, however, this variable is not sufficient to cleanly separate flashers from nonflashers for Daya Bay.

Another characteristic of flashers that has been found useful in developing a discriminator at Daya Bay has been the particular charge pattern of flashing triggers. Flashing PMTs tend to illuminate a few PMTs in their near vicinity as well as PMTs on the opposite wall of the AD (Fig. 3.32). This suggests the use of a "quadrant variable": if $Q_{1,2,3,4}$ are the summed charges of the four azimuthal quadrants of the AD (each consisting of 48 PMTs) centered at the flashing PMT (identified as the PMT with maximum charge), then the ratio Quadrant $= (Q_1 + Q_3)/(Q_2 + Q_4)$ can be used as a measure of this quadrupole moment.

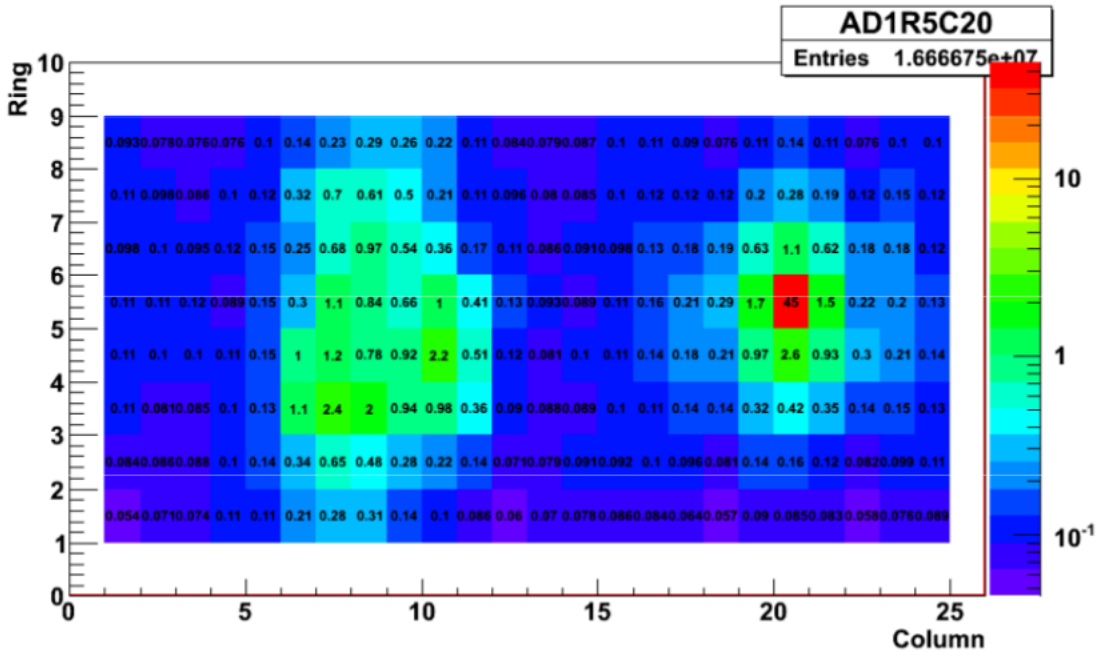

Figure 3.32: Pattern of charge deposit in the AD for a flashing PMT [171].

The need to remove flashers from the data is necessary only to the extent that the IBD efficiency is not significantly affected. That is, we demand that the flasher cuts do not remove true signal events nor contribute false signals (by forming accidental coincidences, for example) [172], but otherwise we are content to leave non-interfering flashers in the raw data. Most flasher studies proceeded by investigating a set of basic variables, making

some cuts on those basic variables, and then arguing that the cuts separated flashers from nonflashers perhaps by plotting the vertex distributions. That a number of variables give some discriminatory power can be seen from Fig. 3.35, which compares the basic distributions of these variables for events passing and failing one particular flasher tag.

We developed a flasher discriminant starting with an unsupervised learning procedure to identify flashing triggers. To be specific, we subdivided the set of all triggers into a tree structure, performing four consecutive binary splits with K-means clustering. This gave 16 final classes, of which several were clearly composed mostly of flashers as judged by their charge and vertex distributions. We then relabeled these classes as flashers and all other classes as nonflashers. The resulting labeled data were then used in a linear discriminant analysis to find an optimal separating hyperplane between the classes. The product of this line of analysis was a single discriminant function that is linear in the input variables and can be used to discriminate between flashers and nonflashers.

The alternative procedure, and the one that has been adopted by all analyses, took the view that low-energy flasher rejection is not important, and that it is sufficient to separate flashers from nonflashers only within a higher energy range where the separation is more clear-cut. Visual inspection of 2D histograms of the $Q_{\max}/Q_{\text{tot}}$ and quadrant ratios suggests the so-called "ellipse cut", defined as:

$$\text{ellipse} = (\text{Quadrant})^2 + (Q_{\text{ratio}}/0.45)^2 < 1$$

Though this approach is more ad hoc, it cleanly separates high-energy triggers into two non-overlapping groups, and so it is argued that the ellipse cut tags the flashers at very high efficiency. Defining FID (Flasher ID) = $\log_{10}(\text{ellipse})$, the plot in Fig. 3.33 illustrates the power of the FID to discriminate flashers from nonflashers. In addition to the ellipse cut, it is found that the 2" calibration PMTs are responsible for many of the flasher triggers. Whenever any of these registers an ESUM greater than 100 PEs, the trigger is also tagged

as a flasher.

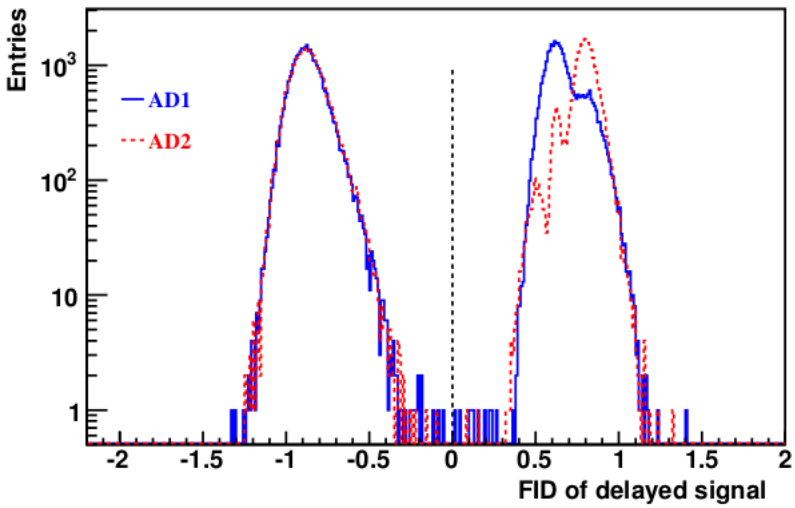

Figure 3.33: Flasher ID (FID) discriminant used to separate flashers from nonflashers. Each entry in the histogram corresponds to the FID of the delayed signal in a set of IBD candidates [27]. Flashers have FID < 0, and vice versa for nonflashers.

From Fig. 3.34 it is apparent that the triggers form multiple groups in the space of these two discriminatory variables. There is no reason to think that all triggers outside the ellipse are indeed flashing PMTs, but it is argued that almost all IBD events should be within the ellipse, and therefore the ellipse cut does no harm to the IBD efficiency. In addition, the distinct groups in Fig. 3.34 merge at lower energies and no clear-cut separation is possible. It has recently been observed that some flashing PMTs survive the ellipse cut, and so the flasher tag has been augmented by new additional criteria.

Monte Carlo studies suggest that we lose 0.02% of the true IBD events as a result of the flasher cuts and introduce a contamination of flasher events into the final IBD rate on the order of about 0.01%. Because of the challenges in identifying and tagging flashers, this figure may be too optimistic. It is more important to ensure that there is no flasher

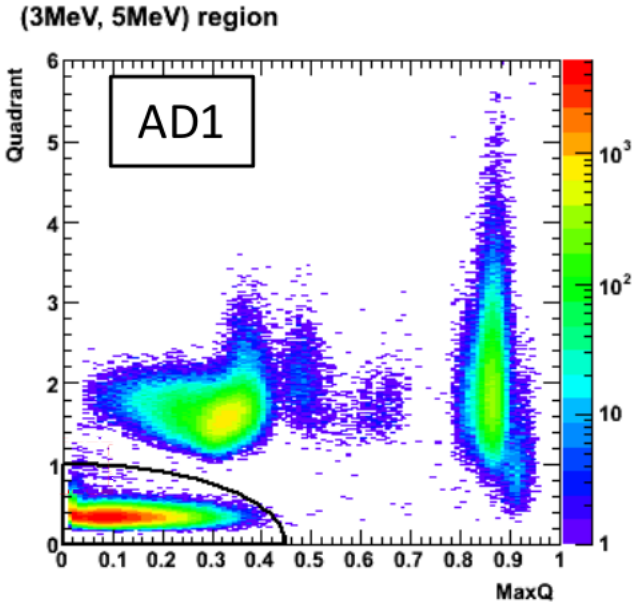

Figure 3.34: Illustration of the ellipse cut for separating flashers from nonflashers in the 3-5 MeV energy range [173].

contamination in the IBD sample than to minimize the IBD inefficiency due to the flasher cut. An IBD inefficiency should largely cancel out in taking the ratio of near and far sites, but excess backgrounds will definitely impact the θ_{13} measurement.

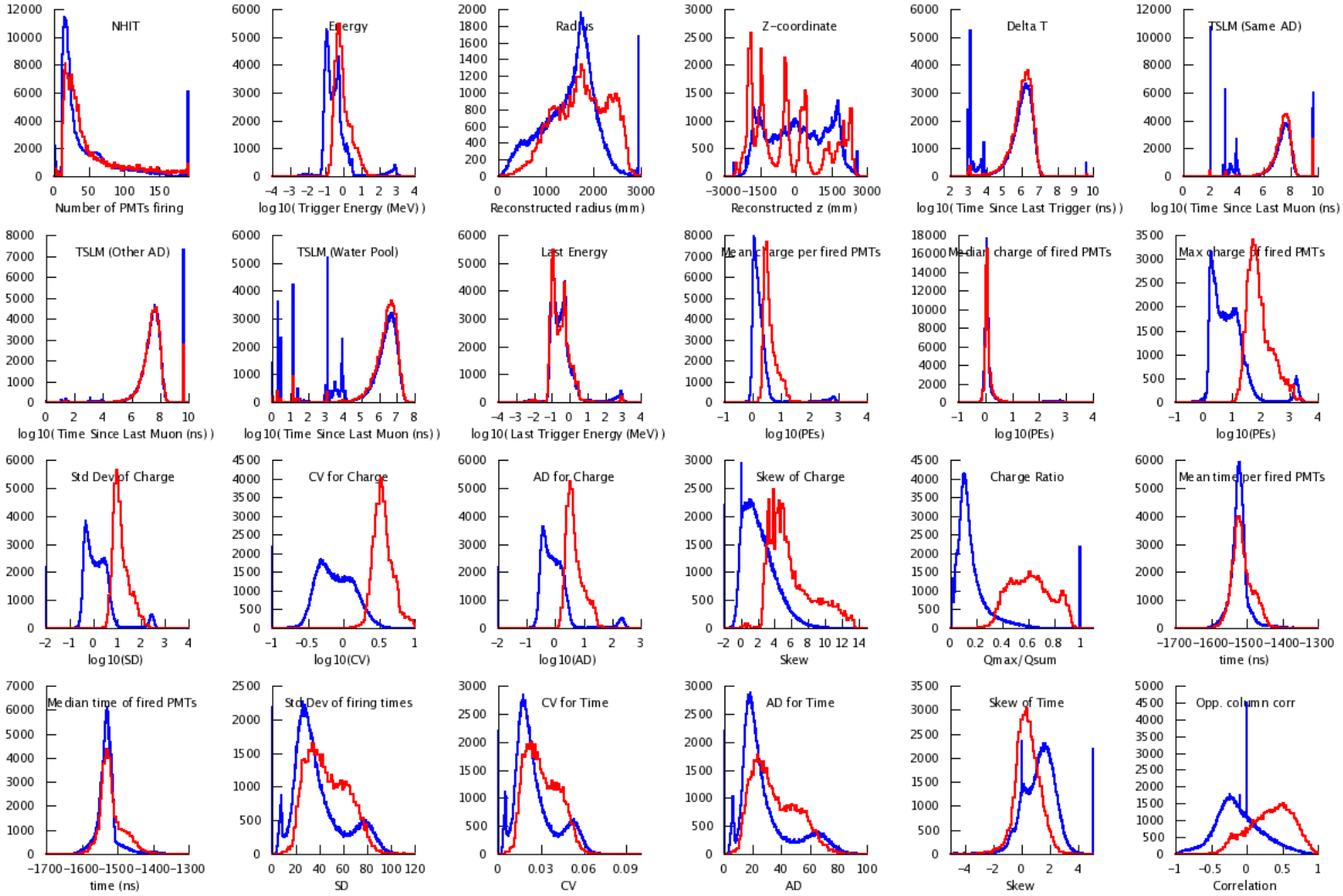

Figure 3.35: Basic distributions of 24 raw variables for triggers passing (failing) a flasher tag in red (blue).

3.8 Antineutrino Candidate Selection

Having removed flashers and enforced a muon veto to clean up the data, we are ready to search for IBD coincidences. In the simplest analysis, we begin by looking for event clusters in which adjacent triggers in the same AD are separated by less than 200 μs. The distribution of cluster multiplicities is shown in Fig. 3.36.

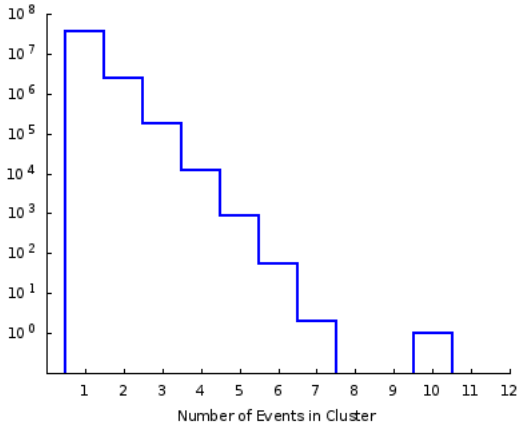

Figure 3.36: Number of triggers per cluster. Adjacent triggers within clusters are separated by < 200 μs.

Many of the triggers within a given cluster are very low energy backgrounds just passing threshold. To uniquely identify the prompt and delayed signal within each cluster, the so-called decoupled multiplicity cuts (DMC) were introduced. The basic idea of these cuts is to veto any trigger groups that do not meet all of the following criteria:

- There is one and only one prompt-like signal (0.7 MeV $< E <$ 12 MeV) within the 200 μs preceding the delayed signal.
- There are no prompt-like signals in the range 200-400 μs before the delayed signal.
- There are no delayed-like signals (6 MeV $< E <$ 12 MeV) in the 200 μs window

following the first.

The DMC cuts are already applied to the KUP data. In every analysis, we demand that the prompt and delayed signals fall within specific energy ranges. These are:

$$0.7 \text{ MeV} < E_{\text{prompt}} < 12 \text{ MeV}$$

$$6 \text{ MeV} < E_{\text{delayed}} < 12 \text{ MeV}$$

These cuts select IBD events where the neutron is captured on gadolinium. From Fig. 3.37 the events of interest are clearly seen to constitute a separate group. Note that IBD events with capture on hydrogen are also visible in the plot. The prompt energy cut is estimated to be 99.9% efficient, and the delayed energy cut is estimated to be 92.2% efficient [44].

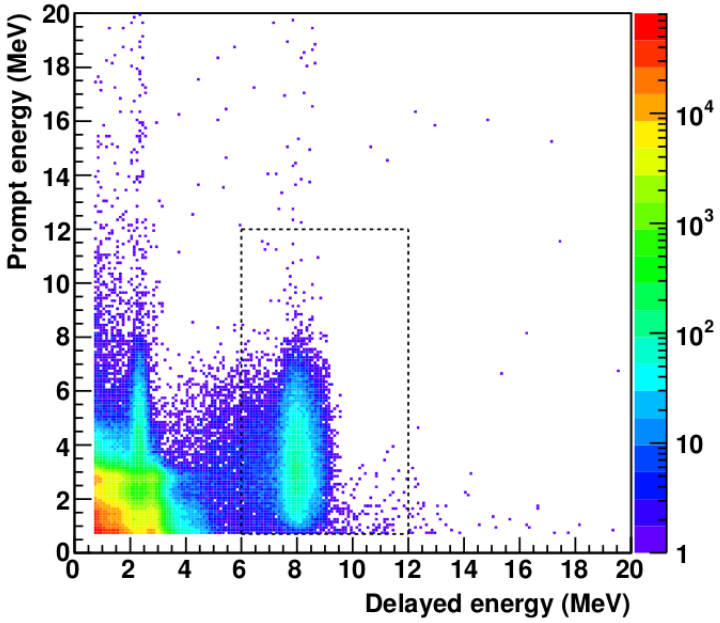

Figure 3.37: Prompt versus delayed energy with energy cuts shown by the dashed line [27].

A final cut is applied to help ensure that the prompt and delayed signals are really correlated. We demand that the prompt and delayed signals are separated by no more than 200 μs. No vertex separation cuts or absolute position ("fiducial" cuts) are employed. Note that the DMC criteria already incorporate the time separation cut. The energy and time separation spectra of IBD candidates from the Daya Bay near site are shown in Fig. 3.38. Except for the muon and flasher cuts, no background removal has yet been performed.

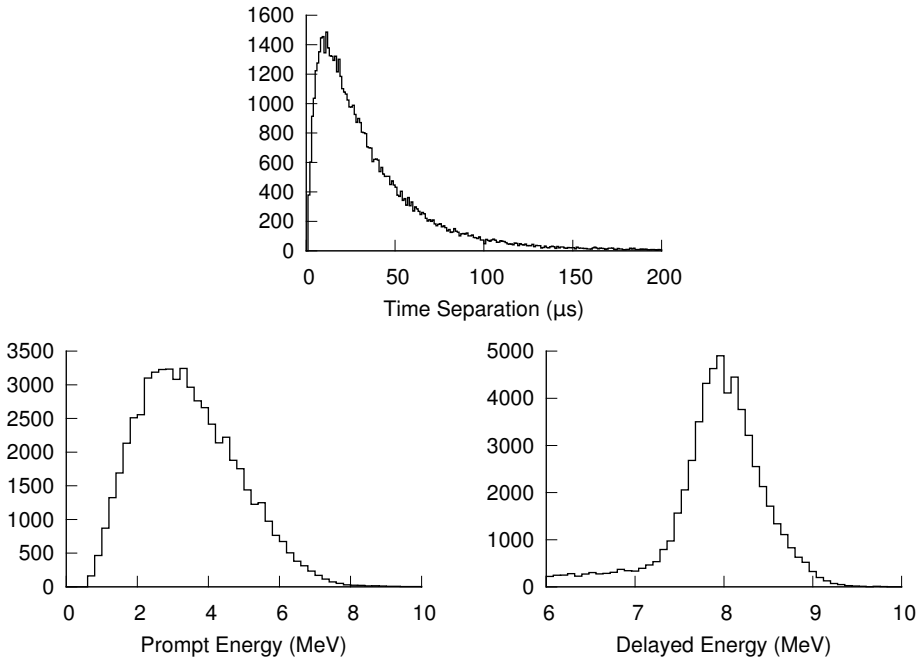

Figure 3.38: Prompt, delayed, and time separation spectra for 57,910 IBD candidates in EH1 collected from December 24, 2011 through February 17, 2012.

3.9 Neutron Backgrounds

3.9.1 Spallation Neutrons

Spallation neutrons arise when high-energy cosmic muons scatter off matter in the detector and cause the target nuclei to break up. Fortunately these are almost wholly removed by the muon veto and so do not interfere with the signal. About 1.5% of these neutrons outlast the muon veto period and therefore contribute to the neutron singles spectrum [28]. Because spallation neutrons are essentially uniformly produced throughout the detector, the signal they create upon nuclear capture can be used to estimate the detector uniformity. In addition, they provide several other useful cross-checks of the analysis.

The neutron multiplicity as a function of the muon energy for simulated spallation events in which the neutron is captured in the target zone or gamma catcher is shown in Fig. 3.39. It is clear from this figure that high-energy muons may generate multiple neutrons. This gives rise to what we call "double neutron" backgrounds: when a pair of neutrons is produced such that the first neutron is captured on hydrogen and the second on gadolinium, the resulting signal is likely to pass the IBD selection criteria. Studies have shown that these backgrounds may be reduced by extending the veto period for muons tagged in the AD modules [174].

By employing fiducial cuts one may measure the neutron capture time in each zone of the detector. This is about 30 μs in the target volume and closer to 200 μs in the outer zones due to the smaller capture cross section on hydrogen. In fact there are many cross-boundary events that are generated in one zone and captured in another, and so the resulting time distribution of all spallation neutrons is a sum of exponentials with differing rates [175].

The spallation neutrons may be used as another source in the energy scale calibration. It has been observed in our detector that there is a slight discrepancy between the mean energy of Gd-captured neutrons from IBD events compared with spallation neutrons. The difference, which is about 0.05 MeV, has been connected with some bias of the neutron energy for spallation neutrons following very high-energy muons [176]. It is not clear whether this

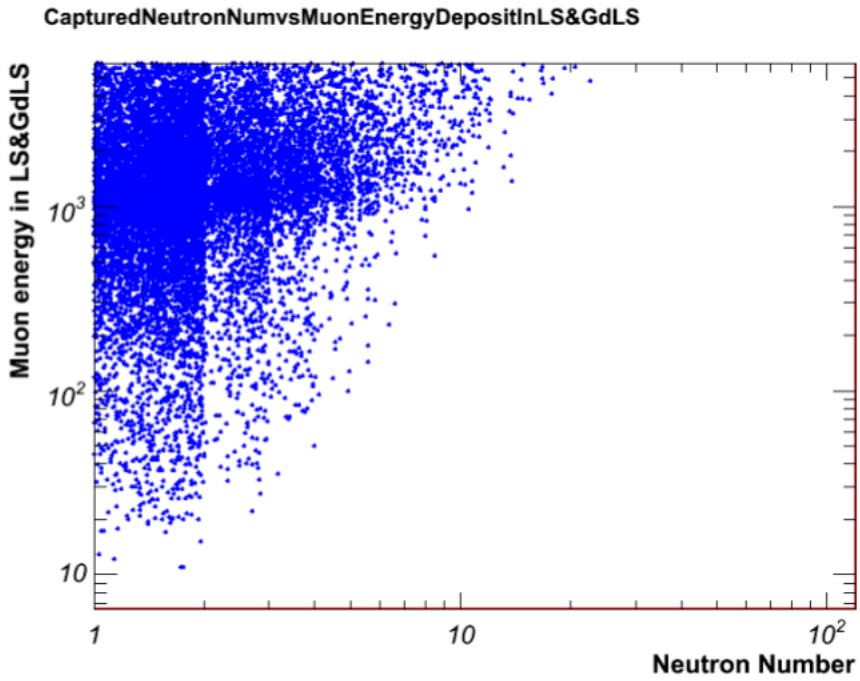

Figure 3.39: Neutron multiplicity from simulated muons. High-energy muons tend to create more spallation neutrons [174]. (The horizontal positions are jittered randomly by the plotting software; neutron multiplicities are of course integer values.)

is due to the finite baseline restoration time or some extra light from other muon products. These events also appear to bias the neutron capture time by 0.5-1 μs [177].

Since the IBD neutrons are required to have energy > 6 MeV, there is some inefficiency due to IBD events with lower energy delayed signals. The inefficiency itself is not an issue, as the IBD rate can be scaled accordingly; it is the uncertainty in the inefficiency that matters. Since there is some uncertainty in the fit parameters that one uses to map the neutron capture peak to reconstructed energy, the absolute uncertainty in the inefficiency is estimated to be 0.17% [178].

Finally, and quite importantly, we note that the IBD rate is dependent on the ratio of gadolinium to hydrogen in the detector. The spallation neutrons can be used to measure

Detector	Gd fraction	Sys Error	Stat Error
DYB AD1	85.8	0.2	0.2
DYB AD2	85.8	0.2	0.2
LA AD1	86.3	0.2	0.2
Far AD1	84.9	0.2	0.9
Far AD2	85.7	0.2	0.9
Far AD3	86.6	0.2	0.9

Table 3.4: Fraction of spallations neutrons in Zone I captured on gadolinium (as opposed to hydrogen) [43].

this quantity by simply comparing the areas of the respective peaks. The resulting ratios from one study are given in Table 3.4.

3.9.2 Fast Neutrons

We consider separately the case of neutrons produced not within the detector itself, but within the surrounding rock. The parent muons of these fast neutrons are not tagged about 30% of the time, typically because they are corner-clippers or miss the water shield altogether [28]. The fast neutrons may be produced singly or may themselves initiate other nuclear reactions that produce neutron daughters. As singles, fast neutrons do not interfere with the IBD signal. However, they may also form several types of coincidences to contribute to the background. First, single neutrons can occur in conjunction with ambient radioactive decays to form accidental coincidences. Next, the neutron may scatter off protons in the detector, and the light generated by proton recoil serves as a prompt signal to produce a correlated event. Spallation neutrons in the detector or water pool may also produce this kind of background. Finally, multiple neutron production can in principle create correlated backgrounds if the first neutron capture happens to fall in the low energy range of the prompt signal (see the discussion on double neutrons above).

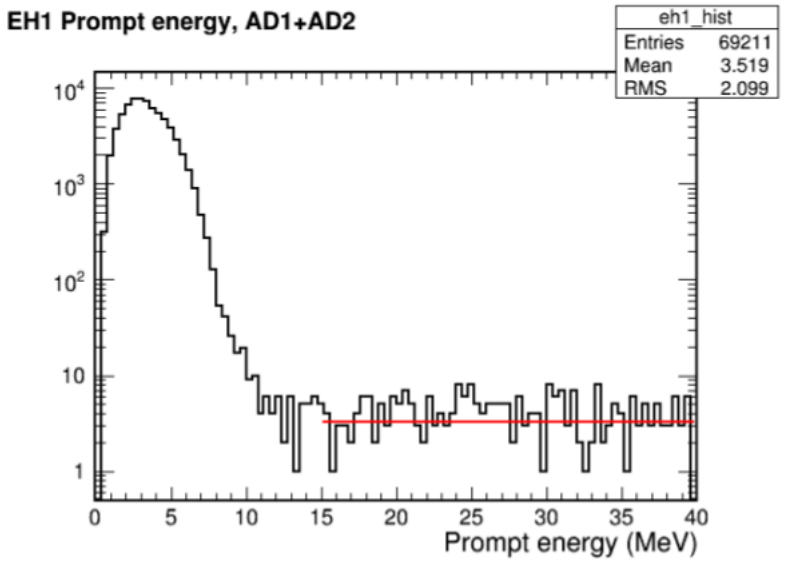

Figure 3.40: Flat background from fast neutron backgrounds measured by relaxing upper cut on the prompt signal in IBD selection [179].

Estimation of the fast neutron background (excluding accidentals for now) indicates that they should contribute roughly one fake IBD event per day at the Daya Bay and Ling Ao detectors. For the far site, where the large overburden reduces the muon flux, the rate is closer to one background per month. Fast neutrons contribute about 0.1-0.2% of the measured IBD candidates at the near sites and 0.06% at the far site.

Two methods are used to estimate this contribution. In one method, a detailed simulation of the muon flux distribution at each detector hall is used to estimate the muon energy spectra at each site. By comparing these Monte Carlo results with real data, one can estimate the muon tagging inefficiency; and by then using the measured fast neutron rate from tagged muons, one can infer the number of fast neutrons from untagged muons [180]. The second method simply uses the IBD candidate spectra without referring to any simulation. From Fig. 3.40 one can see how this is done. By relaxing the upper energy cut of the prompt signal

in each delayed-coincidence pair, a flat high-energy background is observed. Assuming these are due to fast neutrons, once can extrapolate the background into the signal region, and the background level is found to be consistent with the Monte Carlo comparison method [179]. The time spectra (between prompt and delayed) also reveal a second exponential component corresponding to this background.

3.10 Accidental Coincidences

3.10.1 Singles Rate with Trigger Latency

Studies of the accidentals rate typically start from the assumption that the singles are Poisson-distributed. This is accurate to a high degree; however, we note that the finite trigger time actually modifies the distribution. Suppose that the lag time induced by the electronics readout following a trigger is T. With a singles rate of r, the distribution of the time between triggers is a shifted exponential:

$$\Pr(\Delta t) = re^{-r(\Delta t - T)}\Theta(\Delta t - T) \tag{3.26}$$

The probability of the jth trigger time is then just a shifted Erlang distribution:

$$\begin{aligned}\Pr(t_j) &= \frac{r^j \left[t_j - (j-1)T\right]^{(j-1)} e^{-r[t_j-(j-1)T]}}{(j-1)!}, \quad t_j > (j-1)T \\ &= f(t_j - (j-1)T; j, 1/r)\end{aligned} \tag{3.27}$$

where f is the density of the gamma distribution.

We can invert the problem and ask: given a fixed time t, what is the probability distribution of the number of triggers, j? The maximum number of triggers in this time period is $K = \lfloor t/T \rfloor + 1$. This is different from the Poisson distribution, which can in principle realize arbitrarily many triggers. Observe that the probability that there are *no* triggers in

the given time window is equivalent to the probability that the time of the first trigger is greater than t. That is,

$$p_0 = \Pr(j = 0|t) = \Pr(t_1 \geq t) = 1 - \Pr(t_1 < t) = 1 - \gamma(1, rt) = e^{-rt} \tag{3.28}$$

where $\gamma(1, rt)$ is a special value of

$$\frac{\gamma(j, r\,[t_j - (j-1)T])}{(j-1)!} = \gamma_j \tag{3.29}$$

This is the normalized lower incomplete gamma function, which happens to be the c.d.f. of $f(t_j - (j-1)T; j, 1/r)$. Writing γ_j for the value of this function for fixed j, we can continue to calculate the probabilities in this fashion. For example, the probability that $t_2 > t$ is equal to the probability that either there are zero or one triggers in the time t:

$$p_0 + p_1 = \Pr(t_2 \geq t) = 1 - \gamma_2 \tag{3.30}$$

and solving for p_1 gives $p_1 = (1 - \gamma_2) - p_0 = \gamma_1 - \gamma_2$. In general, the probability of k triggers in a finite time period t is

$$p_k = \gamma_k - \gamma_{k+1} \tag{3.31}$$

where we define $\gamma_0 = 1$ and $\gamma_{K+1} = 0$. The mean of this distribution is $E[p_k] = \sum_{n=1}^{K} \gamma_n$.

In Fig. 3.41 the results of simulating a short (10-ms) data acquisition period are shown. With such a short trigger latency period (1 μs), the Poisson probabilities are very close to exact. When the trigger latency approaches $1/r$, the count rates differ from Poisson, as shown in the right plot of Fig. 3.42. For our trigger rates and latencies, the first situation holds and Poisson statistics are entirely appropriate.

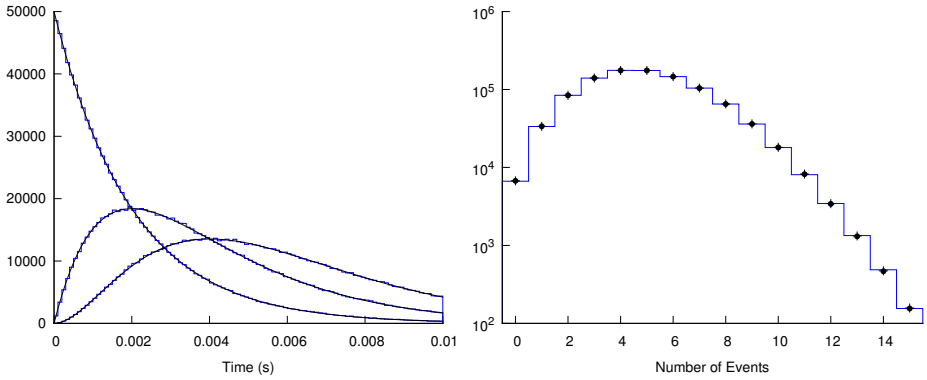

Figure 3.41: Time distributions of the first three triggers (left) and distribution of the number of triggers (right) for a hypothetical situation with $t = 10$ ms, $r = 500$ Hz, and $T = 1$ μs. Blue histogram shows the results of one million simulations. The solid line at left and the black dots at right are the calculated probabilities using the equations above. The crosses in the right plot (overlapping with the black points in this figure) are the corresponding Poisson probabilities for comparison. The expected number of counts is 4.9975 based on this calculation and 5 based on Poisson statistics.

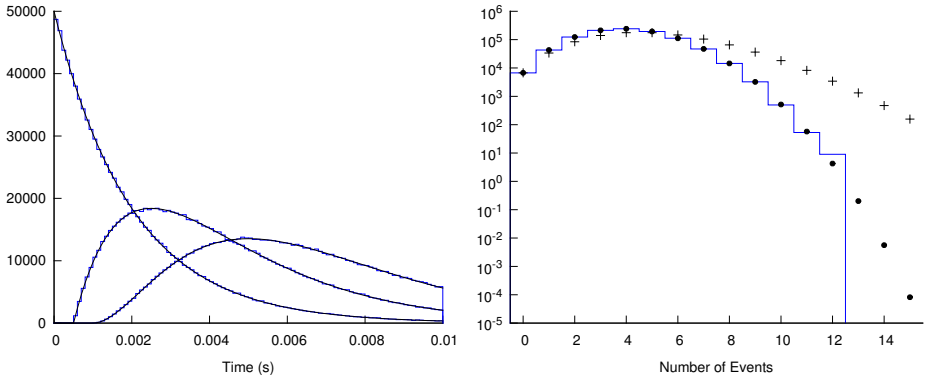

Figure 3.42: As Fig. 3.41 but with latency increased to $T = 500$ μs. The trigger multiplicity is lower than that predicted on the basis of Poisson statistics. The expected number of counts is 4.02 based on this calculation and 5 based on Poisson statistics.

3.10.2 Accidentals Rate Calculation

Calculation of the exact accidentals rate using the IBD selection criteria outlined earlier can become rather involved and depends on the exact way that the DMC cuts are implemented. We sketch a simple derivation of the accidentals rate that is applicable when the delayed rate is small. The idea is just to calculate the probability that a prompt and delayed signal satisify the Δt cut.

In a time t with prompt rate r_p, the number of expected prompt events is $\mu = r_p t$. The distribution of the number of prompt events n is then just a Poisson distribution: $\Pr(n) \sim \mathit{Pois}(\mu)$. The probability that the next delayed event follows the prompt-like signal within a time τ is just the c.d.f. of the exponential distribution with rate r_d: $\Pr(t < \tau) = 1 - e^{-r_d \tau} = p$. Given n prompt events, the probability that k of them are followed within a time τ of a delayed-liked signal is then given by a binomial distribution: $\Pr(k|n) \sim \mathit{Bi}(p, n)$. This is where we assume that the delayed rate is small: we do not worry about the possibility that there may be more than delayed event in the window following a prompt signal. We can now calculate the distribution of accidentals:

$$\begin{aligned} \Pr(k) &= \sum_{n=0}^{\infty} \Pr(k|n)\Pr(n) \\ &= \sum_{n=k}^{\infty} \binom{n}{k} p^k (1-p)^{n-k} \times \frac{\mu^n e^{-\mu}}{n!} \\ &= \frac{(\mu p)^k e^{-\mu p}}{k!} \sim \mathit{Pois}(\mu p) \end{aligned} \tag{3.32}$$

Given the definitions of μ and p, we then have our accidentals rate:

$$r_{\text{acc}} = \frac{\mu p}{t} = r_p(1 - e^{-r_d \tau}) \approx r_p r_d \tau \tag{3.33}$$

which is the usual result.

We now discuss a few of the more subtle assumptions behind this expression. First, we

have assumed a constant probability p for the existence of a delayed signal following each prompt signal. To be precise, for prompt signals occurring in the time range $(t-\tau, t)$, there is less time available for a delayed signal and the probability of forming a coincidence is less than p. In practice the data acquisition time t is long enough to wash out this effect. In our simulations below we allow delayed signals to occur up to time $t+\tau$ to eliminate this annoying artifact.

We have also assumed that, for each prompt event, the existence of a corresponding delayed event is a random binary process that is independent for each trial. If the same delayed event may couple to more than one prompt event to form multiple coincidences, this assumption is violated. To see this, imagine a situation with an extremely high prompt rate. The existence of a delayed signal for one prompt signal means that the next prompt signal is more likely to form a coincidence using the same delayed signal. In our simulations below we allow each delayed event to be used for no more than one coincidence.

Finally, recall that prompt-like events are random triggers with energy between 0.7 and 12 MeV while delayed-like events have energy between 6 and 12 MeV. It follows that all delayed-like events are automatically prompt-like events. Therefore the prompt rate r_p is always greater than the delayed rate r_d, and the prompt and delayed time sequences are not independent after all. Using a delayed event in the construction of one coincidence simultaneously removes a future prompt event for the construction of other potential coincidences. The rate of "prompt-only" signals, i.e. those prompt signals that are not also delayed-like, is $\tilde{r}_p = r_p - r_d$. Fortunately, at sufficiently small values of τ, the approximation of Eq. 3.33 is accurate. This is demonstrated in Fig. 3.43.

To summarize this section, in normal run conditions the accidentals rate can be approximately written as $r_{\text{acc}} = r_p r_d \tau$, but it must be remembered that this is only an approximation and not an exact result. We have considered only a single time-separation cut; the full DMC cuts further complicate the calculation of the exact distribution.

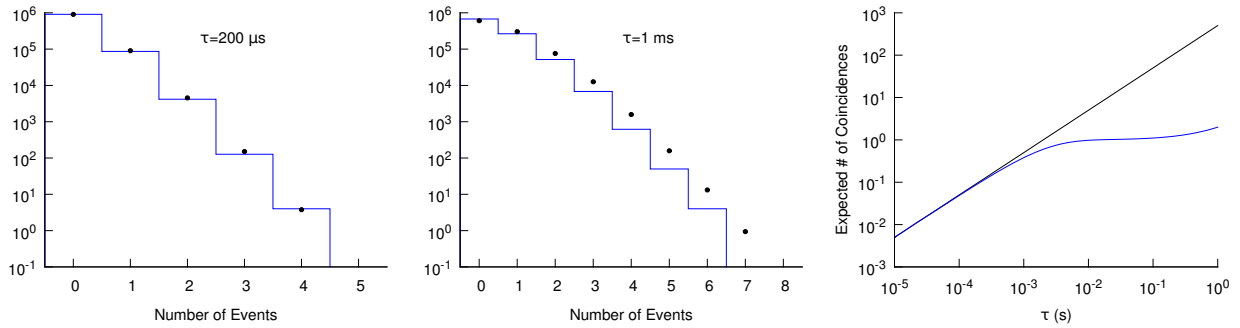

Figure 3.43: The blue histogram on the left shows the distribution of coincidences for 10^6 simulations with $r_p = 500$ Hz, $r_d = 1$ Hz, $t = 1$ s, and $\tau = 200$ μs. The black points show the probabilities based on the rate of Eq. 3.33. The middle plot shows the discrepancy between the real and calculated values when the time cut is extended to $\tau = 1$ ms. The expected number of accidental coincences as a function of τ is shown at right, with black showing the linear scaling and blue showing the results from simulations.

3.10.3 Measured Accidentals Rate

Using the measured singles rates and an approximate formula such as that above, the accidentals rates are have been estimated and are presented in Table 3.5. Because the accidentals are not correlated, the time and spatial distributions are different from IBD events (see Figs. 3.44 and 3.45). These differences can be used to cross-check the accidentals rate calculation. By selecting coincidences with large time separation, the resulting sample is mostly accidental coincidences. The exponential rate is large compared to the time between prompt and delayed events of the IBD signal, and so the resulting time distribution appears flat as in Fig. 3.45. Extrapolating to short Δt, the contribution of the accidentals to the IBD candidates is easily obtained. This is called the "off-window" method. A simple model of the detector geometry shows that 74% of accidentals occur with a spatial separation of greater than two meters, while the IBD rate at this separation is negligible. By counting up the number of events at large separation and then correcting for this efficiency, the accidentals

rate can again be estimated. Both of these methods are in agreement with the calculated rate [181].

	DYB AD1	DYB AD2	LA AD1	Far AD1	Far AD2	Far AD3
Rate	10.00	10.11	7.76	3.37	3.43	3.21
Uncertainty	0.06	0.06	0.05	0.03	0.03	0.03

Table 3.5: Number of accidental coincidences per day in each AD module [44].

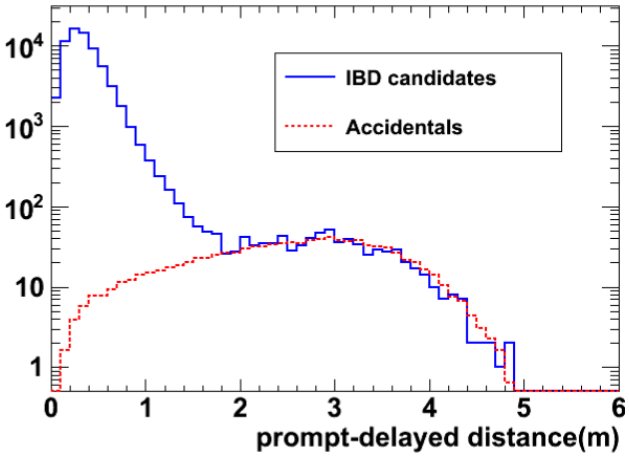

Figure 3.44: Distance between prompt and delayed events for IBD and accidentals in a large data sample [182].

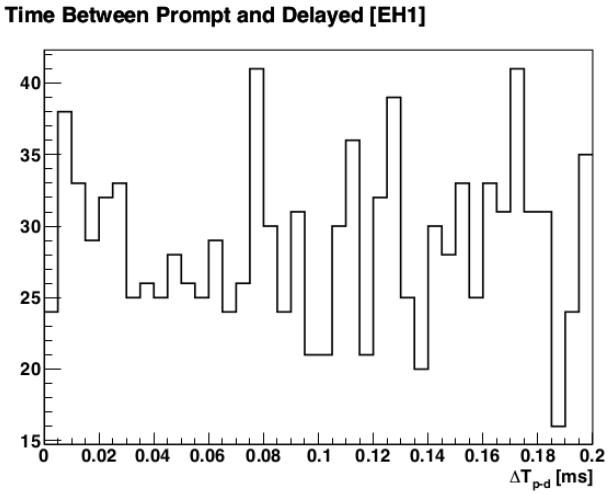

Figure 3.45: Time between prompt and delayed events for accidental coincidences passing the IBD selection criteria [183].

It is of interest to ask what are the sources of the singles that contribute to the accidentals rate. It has been noted that the singles do not appear to be correlated with the reactor power [184]. The prompt events primarily arise from external radiation, while delayed events mostly come from the AmC calibration source and cosmogenic isotopes, two backgrounds that will be discussed later [185].

3.11 Cosmogenic Isotopes

3.11.1 Production

When muons pass through matter in the vicinity of the detector, they may interact to form unstable nuclei. Of particular interest are those isotopes produced by muon spallation on carbon in the liquid scintiallator. Most of these are short-lived, and so by enforcing a short veto following each muon event these backgrounds can be eliminated. Furthermore, the signatures of these decays are often very different from that of the signal of interest. The isotopes ^{8}He and ^{9}Li are exceptions, with half-lives of 119 ms and 178 ms respectively. They mimic the inverse beta signal through beta decay followed by delayed neutron emission. These cosmogenic isotopes are sufficiently long-lived that they cannot be reliably associated with their parent muons. An extension of the veto period long enough to block out the backgrounds due to these isotopes would result in excessive deadtime, and so there is no choice but to live with these backgrounds.

Production of muon-induced cosmogenics has been studied at CERN by impinging a muon beam on a ^{12}C target [34]. The combined cross section for ^{8}He $+^{9}$ Li production was measured to be 2.12 ± 0.35 μb. The two isotopes occur with similar half lives and so are are difficult to separate using timing methods. The cross section is supposed to scale exponentially with muon energy, i.e. $\sigma \sim E_{\mu}^{\alpha}$. Since many of the other isotopes studied were also measured at 100 GeV, the value of α could be extracted for those processes, and the average value is reported to be $\alpha = 0.73 \pm 0.10$.

Other researchers have approached the problem with simulations using GEANT [35]. Bremsstrahlung from slowing muons and muon spallation products generates a spectrum of γs that interact with carbon nuclei through photonuclear processes. As a function of γ energy, they find that the production of ^{8}He and ^{9}Li is unimodal and peaks at around $E_{\gamma} \approx$ 300-400 MeV. Since higher energy muons produce more gammas in this energy range, the total cross section continues to increase with muon energy. The energy scaling factor is

estimated from their simulations to be $\alpha(^9\text{Li}) = 1.06$ and $\alpha(^8\text{He}) = 0.78$. The ratio of ^{9}Li to ^{8}He is reported to be about 3.5 at $E_\mu = 100$ MeV and about 5.4 at $E_\mu = 500$ MeV.

3.11.2 ^{8}He/^{9}Li Generator

To include these important backgrounds in the Daya Bay simulation software, we have developed a code to generate the momenta and vertices for these decays [186, 45, 187]. Decay channels and their branching ratios, Q-values, and widths are obtained from the literature. These are summarized in Table 3.6. We are mainly interested in those pathways involving beta decay followed by delayed neutron or alpha emission. Most decays are to broad levels, which are given a Breit-Wigner form in the simulation.

Parent	Daughter	Width (MeV)	Branching Frac.
^{9}Li	^{9}Be(ground)	0.	0.492
^{9}Li	^{9}Be(2.43 MeV)	0.00077	0.297
^{9}Li	^{9}Be(2.78 MeV)	1.08	0.158
^{9}Li	^{9}Be(7.94 MeV)	1.0	0.015
^{9}Li	^{9}Be(11.28 MeV)	0.575	0.011
^{9}Li	^{9}Be(11.81 MeV)	0.40	0.027
^{8}He	^{8}Li(0.98 MeV)	0.	0.84
^{8}He	^{8}Li(3.21 MeV)	1.0	0.12
^{8}He	^{8}Li(5.4 MeV)	0.65	0.04

Table 3.6: Decay channels taken into account by the ^{8}He/^{9}Li generator [45].

The simplest model of beta decay is the so-called "allowed approximation", in which the electron and neutrino wavefunctions are supposed not to vary over lengths of the order of nuclear dimensions. The unnormalized beta energy spectrum in natural units is then given by

$$\sqrt{E^2 + 2m_e E}(E + m_e)(Q - E)^2 F(Z, E) \tag{3.34}$$

where E is the energy of the electron, m_e is the electron mass, and Q is the total decay

energy. $F(Z, E)$ is the Fermi factor, which accounts for the Coulomb forces between the outgoing electron and the daughter nucleus. The spectra produced by the generator are illustrated in Fig. 3.46.

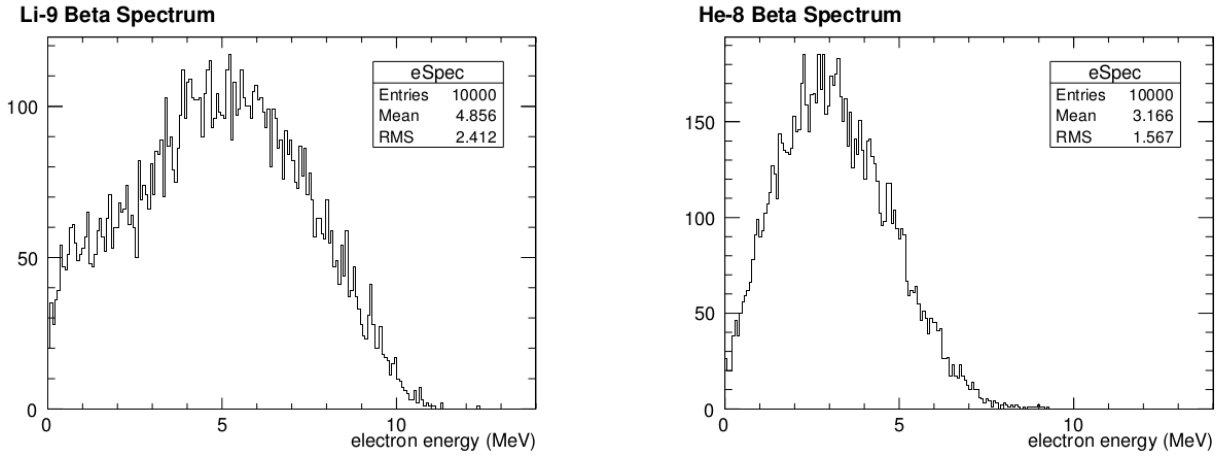

Figure 3.46: Spectra of important cosmogenic isotopes considering only those channels followed by delayed neutron emission [45].

A number of improvements to the generator are possible. Nuclear matrix elements go beyond the allowed approximation, introducing a momentum-dependent factor. Nuclear recoil will reduce the kinetic energy of the outgoing electron, although this is a slight correction. In addition, the parent nuclei produced by the muons may initially be in excited states. Even if all of these effects were properly taken into account and the decay parameters were perfectly known, the uncertainty in the muon flux and the production process itself would complicate any ab initio estimation of the cosmogenic rate.

3.11.3 Measurement

The usual approach in neutrino experiments to measuring cosmogenic background contamination the signal is to plot the time since last muon (or showering muon, since most of these

backgrounds are caused by the light produced in such showers) and fit to a sum of exponentials. True IBD events are not correlated with the muons, and the corresponding exponential rate is simply the IBD rate. Since the coincidences due to cosmogenics are related to the muon background, the rate is much higher. This is evident from Fig. 3.47.

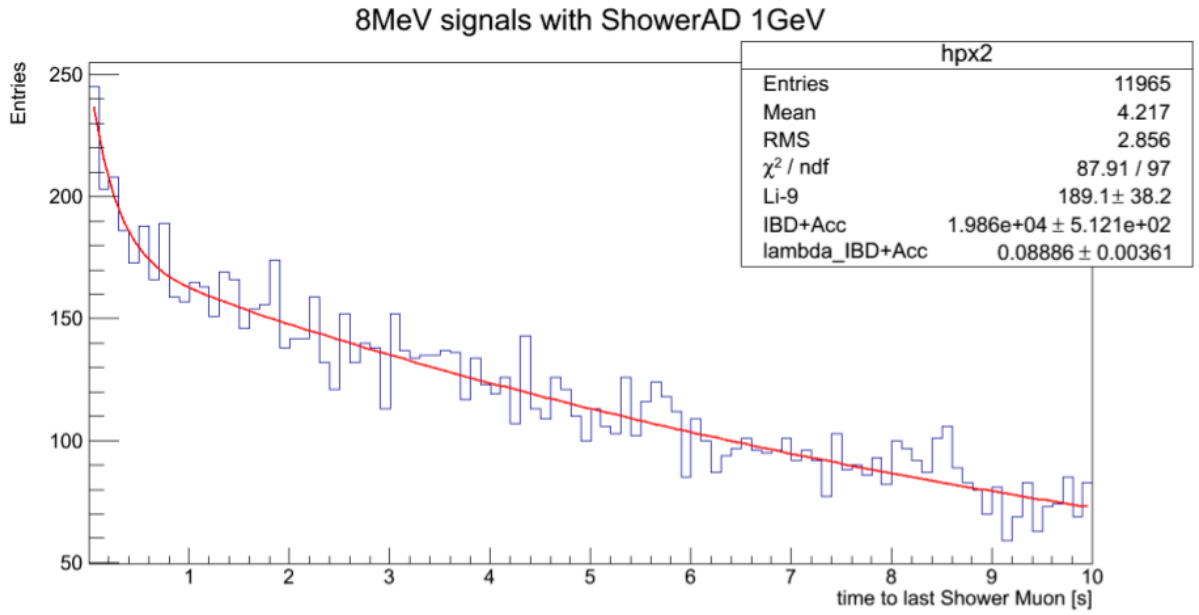

Figure 3.47: Time since last showering muon for a sample of IBD candidates [188]. The showering muon threshold is set at 1 GeV. Cosmogenic backgrounds, which are correlated with their parent muons, show a rapid fall off as the time since muon increases, while true IBD events do not.

Since the rate thus measured depends on the showering muon threshold, the usual approach is to try various values of this cut and extrapolate backward [189]. One cannot just set the cut at a very low value because this increases the number of ^{8}He/^{9}Li events only slightly while the number of IBD events increases at a much faster rate, drowning out the effect of the cosmogenic backgrounds. Other possible modifications to this basic approach include accounting for accidentals in the fit, considering the time since the last n muons, and considering other possible contaminants besides ^{8}He and ^{9}Li. These include ^{11}Be, a cosmo-

genic isotope with a half-life near 30 ms, and ^{210}Po, a product of radon decay. Since there are some discrepancies among the results of these various models, we quote only the PRL estimates: 3.1 ± 1.6 events/module/day (Daya Bay near site), 1.8 ± 1.1 events/module/day (Ling Ao near site), 0.16 ± 0.11 events/module/day (far site).

Other methods for measuring the cosmogenic background may be considered. The Palo Verde experiment noted that the neutron momenta from the inverse beta reaction exhibited a forward-backward asymmetry due to momentum conservation. On the other hand, the cosmogenic backgrounds are completely isotropic [24]. With sufficiently good vertex reconstruction, perhaps this could be used as another means of measuring the background contamination. Double-CHOOZ has proposed another way of measuring this background [36]. The beta-emission daughter of ^{8}He is ^{8}Li, which has a 50% feeding to ^{8}Be via a second beta decay. This signature might be used to measure the production rate of ^{8}He, and in conjunction with knowledge of the combined cross section, an estimate of the cosmogenic production rate can be obtained.

3.12 AmC Background

The AmC neutron source used for energy calibration is actually the source of another background. The source is a mixture of powders of ^{241}Am and ^{13}C. The americium isotope is an α-emitter dominated by the $E_\alpha = 5.5$ MeV line, while the odd-Z carbon isotope is happy to absorb the α and release a neutron ($Q = 2.2$ MeV). The resulting ^{16}O* can be in a couple of excited states, the first releasing an e^+e^- pair upon decay, and the other emitting a 6.13-MeV γ [190].

This mechanism can in principle create two types of backgrounds if the source is not well-contained (and in fact this is the case). The first background is simply due to neutrons leaking into the detector volume and coupling with random singles to produce accidentals. These backgrounds are not separately calculated but are included in the accidentals rate

measurement already discussed. The second type of background are true correlated events, arising from the conjunction of the AmC neutron being captured in the detector and a prompt signal due either to nuclear recoil from neutron scattering or γs from the $^{16}O^{*}$ decay.

The bulk of the neutrons generated by the AmC source are captured on ^{56}Fe in the steel containment vessel of the ACU [191]. This is clear from simulations, which show the neutron capture vertices clearly outlining the ACU structure (Fig. 3.48). Real data show that the neutrons can also spill into the active volume of the detector [192]. These tend to be concentrated toward the top of the AD (Fig. 3.49).

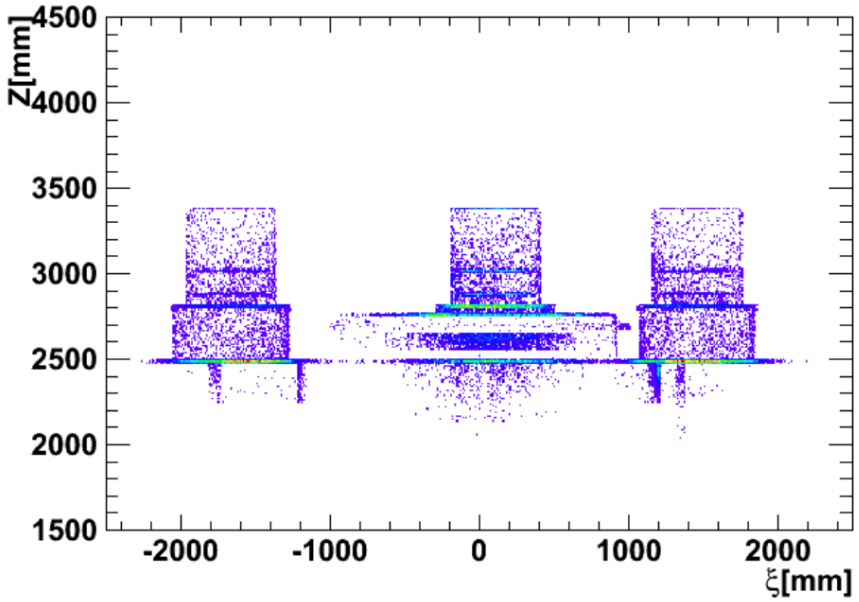

Figure 3.48: Simulated vertices of captured AmC neutrons [193].

The estimates of the AmC coincident background included in Daya Bay's first published results report 0.2 events per day per module with 100% uncertainty. The approximate consistency of the background across sites is reasonable because the prompt singles rate is similar between sites. The source rates of all sources have been measured (3/AD), with an average value of 0.58 ± 0.11 Hz. Using this and other measured data to improve the

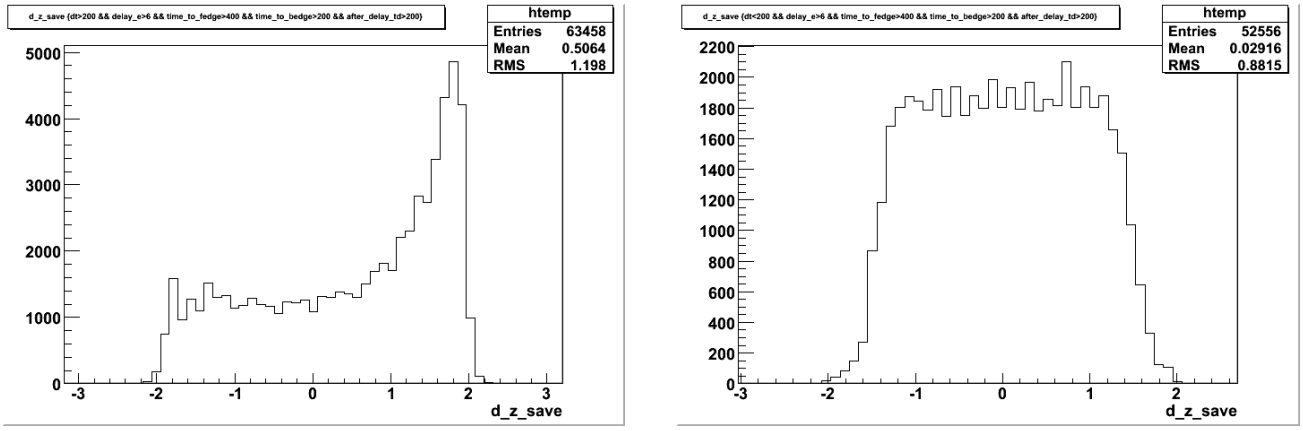

Figure 3.49: Vertical distribution of AmC neutron vertices (left) and IBD neutron vertices (right) for simulated data [194].

simulation of AmC events, the calculated coincidence rates have been updated to the figures in Table 3.7 [193].

DYB AD1	DYB AD2	LA AD1	Far AD1	Far AD2	Far AD3
0.24 ± 0.14	0.24 ± 0.14	0.25 ± 0.14	0.19 ± 0.11	0.18 ± 0.11	0.18 ± 0.10

Table 3.7: Number of coincidences per day due to AmC calibration source.

3.13 Alpha-neutron (α, n) background

We have already discussed the $^{13}\mathrm{C}(\alpha, n)^{16}\mathrm{O}$ reaction in the context of the AmC backgrounds. These backgrounds may also be naturally occurring. The α source in this case is usually from the decays of ^{238}U, ^{232}Th, ^{227}Ac, and ^{210}Po. The latter isotope is a product of ^{222}Rn decay. The alpha interacts on carbon via $\alpha + {}^{13}\mathrm{C} \rightarrow n + {}^{16}\mathrm{O}$. When the oxygen is produced in an excited state, the decay creates a prompt signal and the neutron capture is the delayed signal. As in the discussion of the previous section, the neutron can create its own prompt signal

as it scatters off protons on its way toward thermal equilibrium [195]. The sources of these backgrounds are illustrated in Fig. 3.50 and the rates of each source and the backgrounds they induce are summarized in Table 3.8.

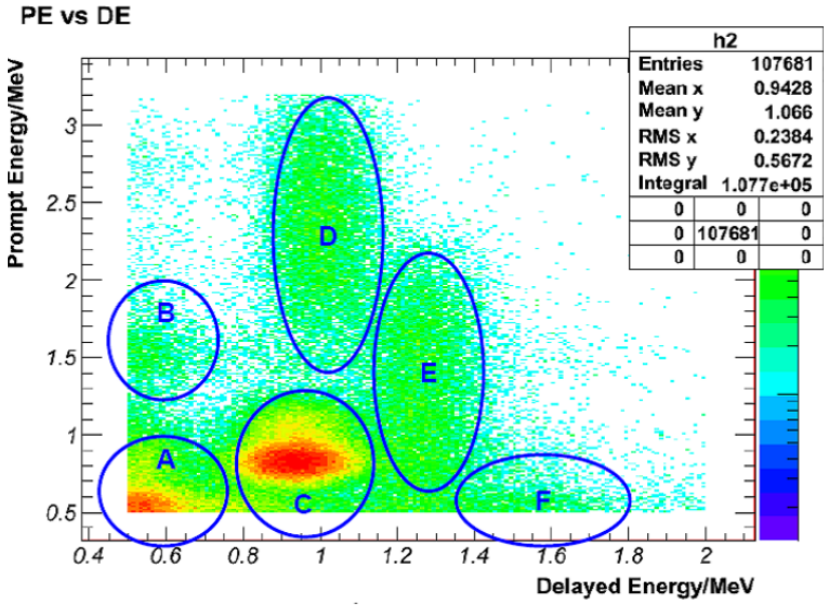

Figure 3.50: Low-energy prompt-delayed coincidences [196]. The sources of each labeled cluster are given in Table 3.8.

Group	Source	α rate	Background rate
C	Cascade decay of ^{227}Ac chain	1.4 Bq	0.01/day
D	Cascade decay of ^{238}U chain	0.07 Bq	0.001/day
E	Cascade decay of ^{232}Th chain	1.2 Bq	0.01/day
A	Acc. Coinc. of ^{210}Po and ^{210}Po	}	Daya Bay: 10 Hz, 0.02/day
B	Acc. Coinc. of ^{210}Po and ^{40}K	}	Ling Ao: 8 Hz, 0.015/day
F	Acc. Coinc. of ^{40}K and ^{210}Po	}	Far: 6 Hz, 0.01/day

Table 3.8: Source of α's in Fig. 3.50 [46].

3.14 Rate Analysis

Having selected IBD candidates and estimated the various backgrounds and detector efficiencies, we are now in a position to estimate the oscillation parameters. First, however, we must estimate the expected rate at each detector site.

3.14.1 Predicted Neutrino Rate

The contribution of reactor j to the integrated neutrino rate of detector i is a combination of many factors:

$$s_i(E) = \sigma(E) M_i T_i \varepsilon_i \sum_j \frac{1}{4\pi L_{ij}^2} f_j(E) p_{ij}^{\text{surv}}(L_{ij}/E) \tag{3.35}$$

$\sigma(E)$ is the energy-dependent total cross section for inverse beta decay. M_i is the target mass of the ith detector (measured in number of protons). T_i is the live time (i.e. the time each detector is able to receive data). ε_i is the detection efficiency, which is treated as a constant but could in a more precise analysis be treated as energy-dependent. L_{ij} is the baseline from the jth reactor core to the ith detector. As mentioned earlier, the finite size of each of these volumes is entirely negligible. The f_j are the neutrino fluxes integrated over 4π steradians. f_j is measured in neutrinos per unit time, and assumes that the neutrinos from the reactor cores are emitted isotropically.

The dependence on $(\Delta m^2, \sin^2 2\theta)$ arises through the survival probability

$$p_{ij}^{\text{surv}}(L_{ij}/E) = 1 - \sin^2 2\theta \sin^2 \left(1.27 \frac{\Delta m^2 L_{ij}}{E} \frac{\text{eV}^2 \cdot \text{MeV}}{\text{m}} \right) \tag{3.36}$$

It is important to note that the mass splitting we use is not exactly the physical mass splitting since the two-neutrino formula is only an approximation to the correct three-neutrino formula. However, to a good approximation, $\Delta m^2 = \Delta m^2_{32}$. For clarity, sometimes the mass splitting in this kind of experiment is denoted Δm^2_{ee}. Fig. 3.51 shows the ratio of the probabilities for these two formulae. The ingredients in this prediction will be treated one

at a time.

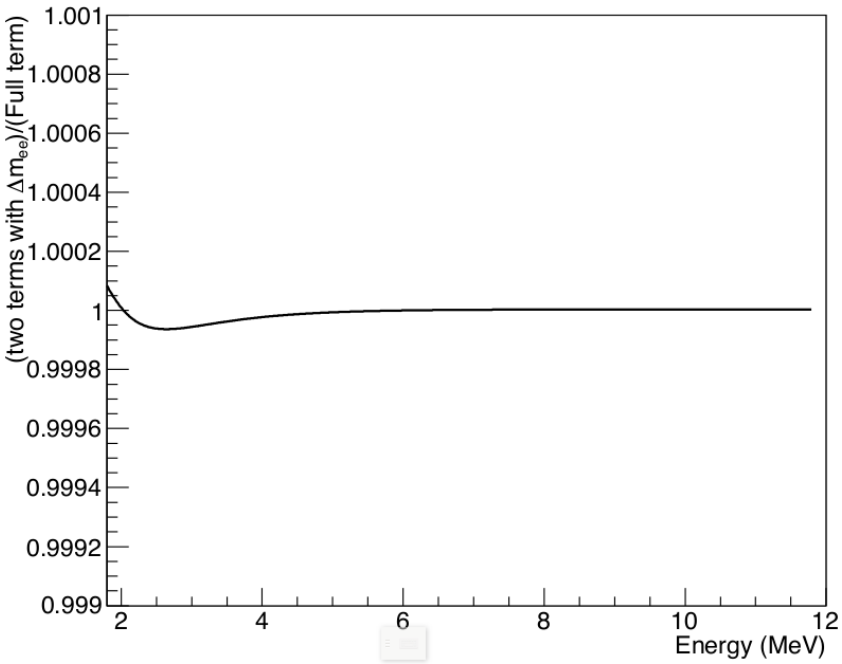

Figure 3.51: Ratio of the three-neutrino oscillation probability to the two-neutrino oscillation probability for $L = 1.6$ km, $\sin^2 2\theta = 0.09$, and $\Delta m^2 = 0.00232$ eV^2. The mass splittings for the three-neutrino expression are obtained from the PDG [197].

Spectral distortion due to imperfect energy resolution may have some effect on shape analyses. This can be modeled as the convolution of the above neutrino rate with a normal distribution, where the width is energy-dependent, i.e.

$$\tilde{s}_i(E) = s_i(E) * \frac{1}{\sqrt{2\pi} r(E)^2} \exp\left(-\frac{E^2}{2r(E)^2}\right), \qquad r(E) = r_0 + r_1\sqrt{E} \tag{3.37}$$

This is not relevant to a rate-only analysis and does not factor into the discussion below.

Reactor Flux

The reactor flux is assumed to be due to the contributions of four fissile isotopes: ^{235}U, ^{238}U, ^{239}Pu, and ^{241}Pu. The spectra of each of these isotopes (in neutrinos fission^{-1}) is given by a simple parametrization [37] given in Table 3.9 and illustrated in Fig. 3.52. The mean fission energy is taken from Ref. [38].

Isotope	Energy per fission	Flux parametrization (neutrinos/fission/MeV)
^{235}U	201.92 MeV	$\exp(3.217 - 3.111E + 1.395E^2 - 0.369E^3 + 0.04445E^4 - 0.002053E^5)$
^{238}U	205.52 MeV	$\exp(0.4833 + 0.1927E - 0.1283E^2 - 0.006762E^3 + 0.002233E^4 - 0.0001536E^5)$
^{239}Pu	209.99 MeV	$\exp(6.413 - 7.432E + 3.535E^2 - 0.882E^3 + 0.1025E^4 - 0.00455E^5)$
^{241}Pu	213.60 MeV	$\exp(3.251 - 3.204E + 1.428E^2 - 0.3675E^3 + 0.04254E^4 - 0.001896E^5)$

Table 3.9: Neutrino spectra from major nuclear fuels.

Let $s_\ell(E)$ be the neutrino yield from each isotope contributing significantly to the reactor fuel, x_ℓ be the fission fraction of the ℓth isotope, e_ℓ be the average energy released per fission, and N_f be the total number of fissions per unit time. The power of the jth reactore core is $P_j = N_f^j \sum_\ell e_\ell^j x_\ell^j$, from which the fission rate for the ℓth isotope is seen to be $x_\ell^j N_f^j = x_\ell^j P_j / \sum_k e_k^j x_k^j$. The reactor flux is a sum over each of the isotopic neutrino yields weighted by this factor:

$$f_j(E) = \sum_\ell \frac{P_j x_\ell^j s_\ell(E)}{\sum_k e_k^j x_k^j} \tag{3.38}$$

Because P_j and x_ℓ^j are varying over the data acquisition period, this expression must be averaged over time. The values of P_j and x_ℓ^j for each reactor core are provided by the Daya Bay Reactor Working Group at weekly intervals for the data acquisition period. The value

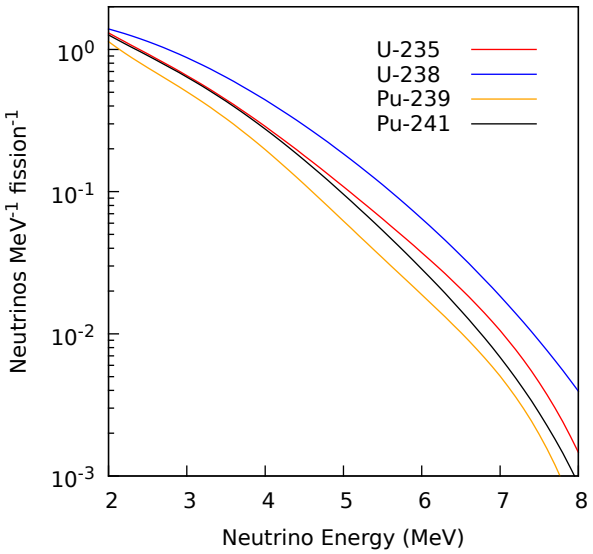

Figure 3.52: Neutrino yield of major fissile isotopes based on parametrization in Ref. [37].

of $f_j(E)$ used in all subsequent calculations is taken as an average at these discrete points in time. With weight $w_\ell^j = \langle x_\ell^j P_j / \sum_k e_k^j x_k^j \rangle$, the reactor flux is $f_j(E) = \sum_\ell w_\ell^j s_\ell(E)$. The fuel history is summarized in Table 3.10, and the weights are given in Table 3.11. The weights are time-averaged influences of the ℓth isotope on the flux of reactor j. The resulting flux from each core is shown in Fig. 3.53.

Core	Mean Power	$\langle x_{^{235}\mathrm{U}} \rangle$	$\langle x_{^{238}\mathrm{U}} \rangle$	$\langle x_{^{239}\mathrm{Pu}} \rangle$	$\langle x_{^{241}\mathrm{Pu}} \rangle$
DB1	2.15 GWth	0.469	0.077	0.372	0.082
DB2	2.87 GWth	0.667	0.075	0.224	0.035
LAI-1	2.39 GWth	0.571	0.076	0.294	0.059
LAI-2	2.44 GWth	0.593	0.076	0.279	0.053
LAII-1	2.82 GWth	0.565	0.077	0.313	0.046
LAII-2	2.28 GWth	0.552	0.078	0.334	0.036

Table 3.10: Time-averaged parameters related to fuel burn-up.

Core	$w(^{235}\mathrm{U})$	$w(^{238}\mathrm{U})$	$w(^{239}\mathrm{Pu})$	$w(^{241}\mathrm{Pu})$
DB1	3.093	0.502	2.403	0.519
DB2	5.845	0.657	1.962	0.304
LAI-1	4.211	0.550	2.089	0.412
LAI-2	4.504	0.561	1.998	0.369
LAII-1	4.837	0.657	2.679	0.393
LAII-2	4.661	0.659	2.822	0.305

Table 3.11: Time-averaged weights ($\times 10^{-19}$) used in the calculation of reactor flux.

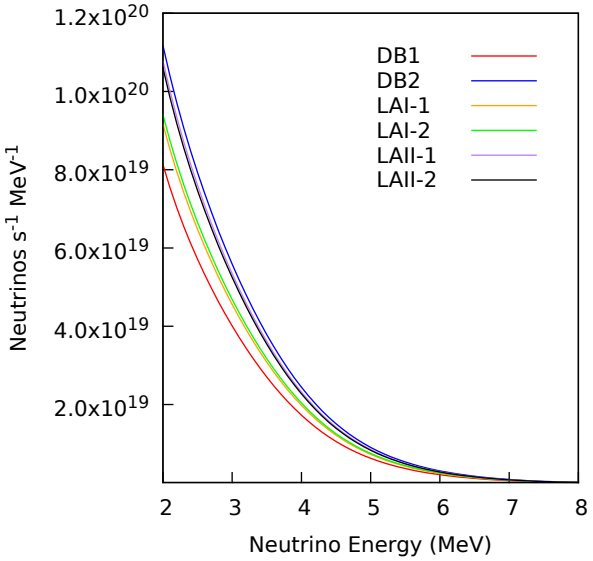

Figure 3.53: Flux of neutrinos from each core.

Cross Section

The lowest order cross section using the most recent neutron lifetime is [21]

$$\sigma(E_{e^+}) = (9.604 \times 10^{-44}\ \mathrm{cm}^2)\left(\frac{E_{e^+}p_{e^+}}{\mathrm{MeV}^2}\right) \tag{3.39}$$

Instead, we use an integrated form of the first-order correction to that cross section, also from [21]. That form is

$$\sigma(E_{e^+}) = (9.604 \times 10^{-44}\ \mathrm{cm}^2)\left(\alpha + \beta\frac{\Delta}{M} + \gamma\frac{E_{e^+}}{M}\right)E_{e^+}^2 \tag{3.40}$$

where M is the mean nucleon mass, Δ is the mass difference between the neutron and proton, and α, β, γ are constants of integration.

The integrated values from 1.8 to 12 MeV are stored in a lookup table [198], which is then interpolated using natural cubic splines. The lookup table speeds the calculation of reactor fluxes also simplifies the process of comparing various groups' analyses. The cross section is shown in Fig. 3.54 along with an example neutrino spectrum from one of the cores.

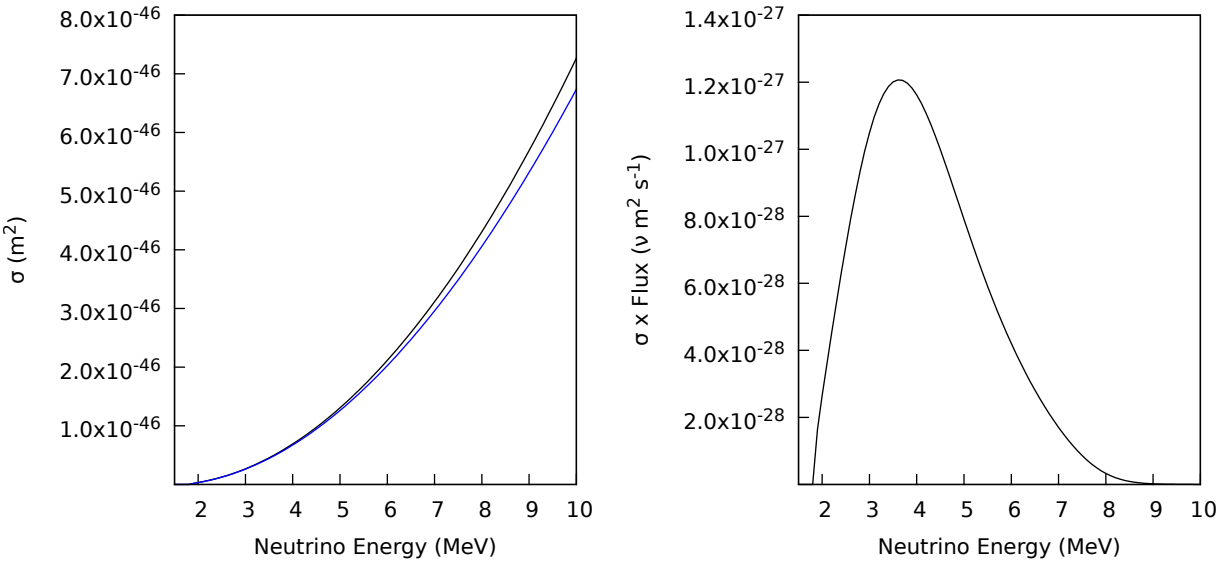

Figure 3.54: The black line in the left plot is the lowest order IBD cross section, while the blue line shows the first-order correction by Vogel & Beacom. Right plot is the product of the cross section and the reactor flux for Daya Bay Core 1.

Baselines

The baselines, shown in Table 3.12, are obtained from precise surveys [40]. In earlier analyses, these were blinded, but the values shown below are the true distances.

	DB1	DB2	LA1	LA2	LA3	LA4
AD1	362.4	371.8	903.5	817.2	1353.6	1265.3
AD2	357.9	368.4	903.4	816.9	1354.2	1265.9
AD3	1332.5	1358.1	467.6	489.6	557.6	499.2
AD4	1919.6	1894.3	1533.2	1533.6	1551.4	1524.9
AD5	1917.5	1892.0	1534.9	1535.0	1554.8	1528.0
AD6	1925.3	1899.9	1538.9	1539.5	1556.3	1530.1

Table 3.12: Baselines of all detectors from all reactor cores to the nearest tenth of a meter. The uncertainty is estimated to be 2.8 cm.

Survival Probability

As discussed in the introduction to this section, we just use the two-neutrino expression

$$p_{ij}^{\text{surv}}(L_{ij}/E) = 1 - \sin^2 2\theta \sin^2\left(1.27\,\frac{\Delta m^2\,L_{ij}}{E}\right) \tag{3.41}$$

where Δm^2 is measured in eV^2, L_{ij} in m, and E in MeV.

Target Masses

Calculation of the target mass is a bit tricky, as there are various objects inside of the detector that displace fluids into the overflow volume. In principle this should be accounted for in the detector efficiency, but in practice we have observed some discrepancies in the way various groups calculate the target volume. Assuming target masses below and 6.16×10^{22} protons/mL and 0.860 g/mL [199, 200, 201] we obtain the target masses in Table 3.13.

	AD1	AD2	AD3
mass(kg)	19941	19966	19891
# protons	1.42833×10^{30}	1.43191×10^{30}	1.42482×10^{30}
	AD4	AD5	AD6
mass(kg)	19913	19991	19892
# protons	1.42632×10^{30}	1.43191×10^{30}	1.42482×10^{30}

Table 3.13: Target masses [199].

Live Times & IBD Efficiency

The live times are taken from the CPC article and already account for the muon veto period. The multiplicity cuts described in Section 3.8 induce some inefficiency in the detection of neutrino candidates. Since the accidentals rate and the IBD rate are assumed independent Poisson processes, the probability of an IBD event satisfying the multiplicity cut can be calculated from first principles. The accidentals rate is tied to the muon rate, which is in turn related to the DAQ live time. Thus it is easiest to measure the net live time accounting for both the IBD detection effiency as well as the muon-induced dead time. These values are given in Table 3.14.

AD1	102.23 days
AD2	101.86 days
AD3	106.54 days
AD4	120.65 days
AD5	120.61 days
AD6	120.54 days

Table 3.14: Live times adjusted for ε_m and ε_μ.

Detection Efficiencies

The prompt and delayed energy cuts are chosen with the aid of Monte Carlo simulations. The prompt energy cut is nearly 100% efficient, but the delayed neutron spectrum is broad, and so some compromise to the efficiency must be made to keep the signal to noise ratio within reason. The IBD time cut is also obtained from simulations. The neutron capture time spectrum is measured with the AmC source, allowing us to estimate the ratio of gadolinium to hydrogen. With this information and knowledge of the cross sections and isotopic abundances, we may compute the gadolinium capture efficiency seen below. The spill-in and flasher cuts have already been discussed. Again, for consistency with other analysese we use the same detection efficiencies as the recent CPC article. These are listed in Table 3.15.

Flasher cut	99.98%
Delayed energy cut	90.9%
Prompt energy cut	99.88%
Capture time cut	98.6%
Gd capture ratio	83.8%
Spill-in	105.0%

Table 3.15: IBD detection efficiency factors.

The net detection efficiency after all these factors is considered is 0.78753.

Predicted Rates

Using the above ingredients, the estimated neutrino rates at each detector are obtained by numerically integrating the right-hand side of Eq. 3.35. The small discrepancy between the values computed for this study and the values computed for the CPC article are most likely due to the different parametrization of reactor flux. In any case the predicted values are very similar, and were obtained using only information that is publicly available.

	My Expectation	CPC Expecation	CPC/This study
AD1	69315.1	68613	0.990
AD2	70322.3	69595	0.990
AD3	67322.8	66402	0.986
AD4	10054.1	9922.9	0.987
AD5	10071.3	9940.2	0.987
AD6	9966.7	9837.7	0.987

Table 3.16: Predicted rates compared to CPC expectations.

3.14.2 Parameter Estimation

The usual analysis of neutrino oscillation experiments involves minimizing a chi-square expression with so-called "pull terms". This type of analysis is equivalent to a maximum a posterior (MAP) estimate. Let M_d is the measured counts in detector d, and let $T_d(\sin^2 2\theta, \Delta^2_m)$ be the corresponding estimated counts as calculated in the previous section. Let N be an overall normalization correction, ε_d be the uncorrelated detection uncertainty, and B_d be the backgrounds in detector d. Then the actual expectation of the number of counts, considering the aforementioned factors, is $\tilde{T}_d = N\, T_d\, \varepsilon_d + B_d$.

Given that M_d is large and Poisson distributed, we may to a good approximation take the distribution of M_d to be gaussian:

$$\Pr\left(M_d \,|\, N,\, \sin^2 2\theta,\, \Delta m^2,\, B_d,\, \varepsilon_d\right) = \frac{1}{\sqrt{2\pi\tilde{T}_d}} \exp\left(-\frac{(M_d - \tilde{T}_d)^2}{2\tilde{T}_d}\right) \tag{3.42}$$

Assuming the counts are independent, the negative log-likelihood (i.e. "chi-square") is

$$-\ln L = \sum_{d=1}^{6} \left[\ln \tilde{T}_d + \frac{(M_d - \tilde{T}_d)^2}{\tilde{T}_d}\right] \tag{3.43}$$

after dropping constant factors and multiplying by 2. Ordinary maximum likelihood estimation seeks to estimate all parameters by finding the minimum of this expression.

We have not yet accounted for any prior knowledge of the parameters. For example,

we have some idea of the backgrounds in each detector, and so these parameters should be constrained in some way. MAP estimation maximizes the posterior probability for the data. Assuming each of these priors is gaussian, we construct the full a posteriori likelihood:

$$\begin{aligned} L_{\text{post}} = & \frac{1}{\sqrt{2\pi}\sigma_{\Delta m^2}} \exp\left(-\frac{(\Delta m^2 - \mu_{\Delta m^2})^2}{2\sigma^2_{\Delta m^2}}\right) \\ & \times \prod_{d=1}^{6} \frac{1}{\sqrt{2\pi\tilde{T}_d}} \exp\left(-\frac{(M_d - \tilde{T}_d)^2}{2\tilde{T}_d}\right) \\ & \times \frac{1}{\sqrt{2\pi}\sigma_{B_d}} \exp\left(-\frac{(B_d - \mu_{B_d})^2}{2\sigma^2_{B_d}}\right) \\ & \times \frac{1}{\sqrt{2\pi}\sigma_{\varepsilon_d}} \exp\left(-\frac{(\varepsilon_d - 1)^2}{2\sigma^2_{\varepsilon_d}}\right) \end{aligned}$$

This gives the following expression to be minimized:

$$-\ln L_{\text{post}} = \sum_{d=1}^{6} \left[\ln \tilde{T}_d + \frac{(M_d - \tilde{T}_d)^2}{\tilde{T}_d} + \frac{(B_d - \mu_{B_d})^2}{\sigma^2_{B_d}} + \frac{(\varepsilon_d - 1)^2}{\sigma^2_{\varepsilon_d}}\right] + \frac{(\Delta m^2 - \mu_{\Delta m^2})^2}{\sigma^2_{\Delta m^2}} \quad (3.44)$$

Again we have dropped constants and multiplied through by 2. Note that the normalization N and the mixing angle expression $\sin^2 2\theta$ are not constrained.

The posterior likelihood above differs in several ways from the chi-squared with pulls given in the CPC. First, we have assumed that the data M_d contain all backgrounds. The first is largely cosmetic. Defining $\eta_d = B_d - \mu_{B_d}$, $\epsilon_d = \varepsilon_d - 1$, and $M'_d = M_d - \mu_{B_d}$, the quadratic terms inside the square brackets above reduce to

$$\frac{(M'_d - N\,T_d\,(1+\epsilon_d) - \eta_d)^2}{N\,T_d\,(1+\epsilon_d) + \eta_d + \mu_{B_d}} + \frac{\eta_d^2}{\sigma^2_{B_d}} + \frac{\epsilon_d^2}{\sigma^2_{\varepsilon_d}} \quad (3.45)$$

where the last two terms are called "pull terms" and represent the deviation of the uncorrelated detection efficiencies and the backgrounds from their expectations. In addition, we treat the normalization as a constant prefactor after efficiencies have been applied. In the CPC article, the normalization is considered a correlation alongside the uncorrelated

detection efficiency, whence $N\,T_d\,(1+\epsilon_d) \rightarrow T_d\,(1+\epsilon+\epsilon_d)$. Note that the correlated detector uncertainty ϵ is absorbed into our overall normalization factor N. This may be preferable in that normalization shifts may be due to more than just detection efficiency; errors in the neutrino flux model would also contribute to this factor. Also, the CPC prefers the Neyman version of the chi-square rather than the Pearson version. Since $\mathrm{Exp}\,[M'_d] = \mathrm{Exp}\,[N\,T_d\,(1+\epsilon_d)+\eta_d] = N\,T_d\,(1+\epsilon_d)$, this substitution is made in the denominator. Including these two changes finally gives a typical "pull chi-square" expression:

$$\frac{(M'_d - T_d\,(1+\epsilon+\epsilon_d) - \eta_d)^2}{M'_d + \mu_{B_d}} + \frac{\eta_d^2}{\sigma_{B_d}^2} + \frac{\epsilon_d^2}{\sigma_{\varepsilon_d}^2} \tag{3.46}$$

The pulls η_d and ϵ_d are to be interpreted as corrections to the corresponding parameters. They are taken to be normally distributed with expectation 0, so that each term on the right is a stardard normal variable representing a penalty on the discrepancy of each fit parameter from its expectation.

The CPC version of the chi-square also includes a reactor-uncorrelated uncertainty, which we have neglected in our analysis. This amounts to introducing six new pull terms. On the other hand, we have two additional terms that are not taken into account in that analysis. One is the constraint on Δm^2, which introduces another term on the right hand side. The other is the presence of the $\ln \tilde{T}_d$ term. Our experience suggests that this term does not significantly affect the location of the minimum, and so in order to compare our chi-squared values with other studies, we omit this term when performing the minimization. Excluding this term, the negative log-likelihood should follow a chi-square distribution with 19 degrees of freedom, with 15 parameters being estimated from the data, for a net total of four degrees of freedom.

As Neyman showed in 1949 on his discussion of best asymptotically normal estimates, the (unpenalized) Neyman chi-square as well as the usual Pearson chi-square all converge to the usual maximum likelihood estimate [39]. We conjecture that the MAP estimate we present

as well as the various forms of the pulls analysis should also be asymptotically equivalent.

We use the value of Δm^2 from the PDG, averaging the upper and lower error bars: $\mu_{\Delta m^2} = 0.00232\ \mathrm{eV}^2$ and $\sigma_{\Delta m^2} = 0.0001\ \mathrm{eV}^2$. The other uncertainties are listed in the previous section. The minimum is obtained by a simplex method. Each variable is rescaled so that a typical value is around unity, and a 15-dimensional polytope contracts around the minimum until the vertices are within a prescribed tolerance. The fitted values of three parameters are given in Table 3.17, with $\chi^2/\mathrm{NDF} = 3.4/4$. The backgrounds fitted to each detector are within their respective 1-σ intervals, as shown in Table 3.18. These are incorporated into an estimate of the overall neutrino rate at each site in Table 3.19. None of the detector efficiencies vary from unity by more than 0.00055, probably suggesting the insignificance of these parameters to the fit quality.

Parameter	Fit Value
N	0.9889
$\sin^2 2\theta$	0.09264
Δm^2	0.0023204

Table 3.17: MAP estimate of three parameters.

Detector	Expected BG	Uncertainty	Fit
AD1	1398.5	157.0	1449.1
AD2	1380.2	156.5	1346.1
AD3	1105.9	124.5	1095.5
AD4	429.51	28.75	439.04
AD5	428.17	28.74	427.52
AD6	414.66	28.55	405.92

Table 3.18: Fitted backgrounds compared to expectation.

Detector	Expected Rate	Fitted Rate	Measured
AD1	70752	68979.7	69121
AD2	71675.7	69811.4	69714
AD3	68416.8	66517.8	66473
AD4	10487.9	9677.0	9788
AD5	10499.2	9676.6	9669
AD6	10377.5	9555.0	9452

Table 3.19: The first column is the sum of the expected IBD rate in Table 3.16 (no oscillation) and the expected backgrounds. The second column gives the sum of the expected IBD rate with the fitted oscillation parameters and the fitted background rates, which should be compared with the final column of measured rates.

Explorations of the likelihood surface

A critical point of a function is a non-degenerate local minimum only if the Hessian matrix evaluated at the point is nonsingular. Otherwise the problem is under-determined and some parameters are not estimable. A simple example is the function $f(x, y) = (x + y - 1)^2$. The minimum is degenerate in that all points on the line $x + y = 1$ achieve the same value of the function. We compute the matrix elements (second derivatives) numerically evaluated at the MAP estimate. The elements are rescaled by the estimated "curvature scale" of each parameter: $H_{ij} \to \sigma_i \sigma_j H_{ij}$, and the resulting matrix is shown in Fig. 3.55.

The eigenvalues of this matrix may be lumped into three groups. A single large eigenvalue (30) corresponds to an eigenvector dominated by the normalization. There are seven intermediate eigenvalues (5-8), and seven small eigenvalues (< 1.5). The loadings of the eigenvectors corresponding to the small eigenvalues are dominated by the background parameters. When these parameters are fixed at their expected values, the estimates of N, $\sin^2 2\theta$, and Δm^2 do not change by more than 0.03%. The fit quality does worsen, however, with $\chi^2/\text{NDF} = 3.8/4$. With the uncorrelated detector efficiencies fixed instead, the $\chi^2/\text{NDF} = 3.6/4$. In summary, there appears to be a degree of approximate degeneracy in the minimum of the χ^2.

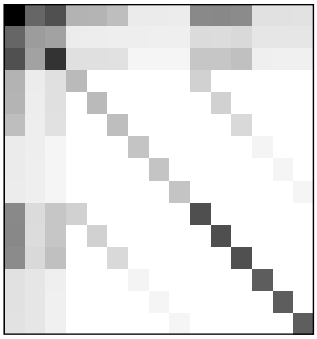

Figure 3.55: Hessian matrix for the negative log-likelihood function evaluated at the minimum. The 15×15 matrix is represented with elements coded as grayscale pixels, with black being higher. The plot is log scale, so that we actually plot $\log_{10}(|H_{ij}| + 1)$. From indices are numbered from left to right, top to bottom, with each index corresponding to $(N, \sin^2 2\theta, \Delta m^2, B_1, \ldots, B_6, \varepsilon_1, \ldots, \varepsilon_6)$.

For the remainder of this section, when quoting point estimates with errors, we use the full 15-dimensional optimization, but when we show any two-dimensional raster scan plots, we fix both the backgrounds and the detector uncertainties to speed the computation.

Fixed Parameters	N	$\sin^2 2\theta$	Δm^2 (eV^2)	χ^2	Time (s)
None	0.988863	0.092635	0.00232036	3.41	96.8
B_d	0.988902	0.092668	0.00232046	3.83	12.4
ε_d	0.988857	0.092631	0.00232047	3.64	21.8
B_d & ε_d	0.988905	0.092673	0.00232064	4.19	2.4
(CPC Result)	–	0.089	–	3.4	–

Table 3.20: Fit results with various inputs fixed.

With B_d and ε_d held fixed, the likelihood surface is illustrated in Figs. 3.56 and 3.57. The first plot is a slice through the $(N, \sin^2 2\theta, \Delta m^2)$ space where N is fixed at its fitted value, and the second plot shows a projection of $\max_N L_{\text{post}}$. It is this second plot that is most relevant to determining the confidence intervals.

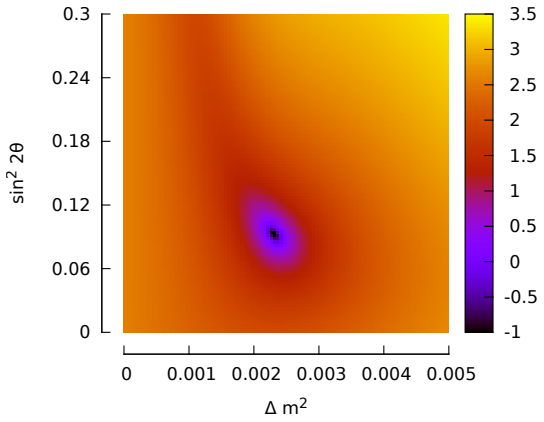

Figure 3.56: Likelihood in the plane $N = \hat{N}$ (N is fixed at its fitted value). The backgrounds and detector efficiencies are fixed.

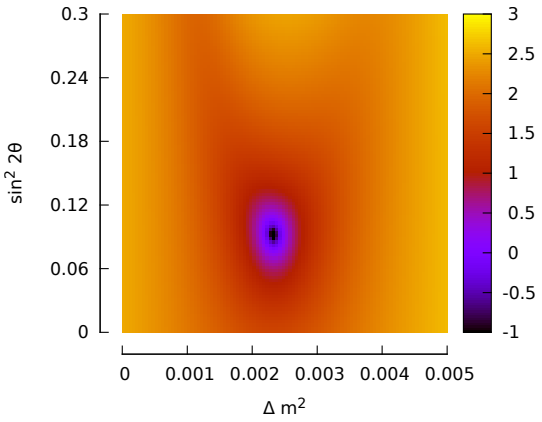

Figure 3.57: Likelihood map in which, for each value of $(\sin^2 2\theta, \Delta m^2)$, the likelihood is maximized over N. The backgrounds and detector efficiencies are fixed.

Fit for $\sin^2 2\theta$ *and* Δm^2

Without the constraint on the mass splitting, the 1-, 2-, and 3-σ confidence regions for $\sin^2 2\theta$ and Δm^2 are as shown in Fig. 3.58. Note that there is a slight amount of tension between the fitted best value of Δm^2 from our data compared with the known value of Δm^2 from the PDG. In fact, given the shape of these levels, it is remarkable that the best fit value is as close as it is. While the PDG reports asymmetric error bars on the mass splitting ($\Delta m^2_{32} = 2.32^{+0.12}_{-0.08} \times 10^{-3}$ eV^2), except in Fig. 3.58, we have symmetrized the errors to ± 0.0001 eV^2. We also note that the Δm^2 in the two-neutrino formula that we use is not exactly equivalent to Δm^2_{32}, but for the sake of this work we treat them as the same (which is approximately true). In this fit, the resulting parameter estimates are

$$\sin^2 2\theta = 0.0939$$

$$\Delta m^2 = 0.002695$$

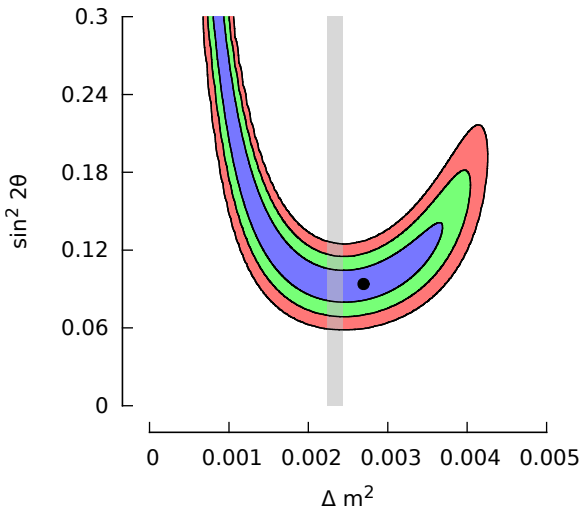

Figure 3.58: Simultaneous confidence regions for $\sin^2 2\theta$ and Δm^2 without the constraint on Δm^2. The vertical gray band shows the 1-σ region allowable from MINOS (as reported by the PDG).

Fig. 3.59 shows the effect of incorporating this constraint. The correlation between $\sin^2 2\theta$ and Δm^2 is slight. We compute confidence regions using the likelihood ratio test. The 1-σ confidence intervals turn out to be very nearly symmetric for both parameters, and so we report errors as $\pm 1\sigma$. We make no attempt to separate "systematic" from "statistical" uncertainties, as recent Daya Bay publications have done. The mass splitting results are

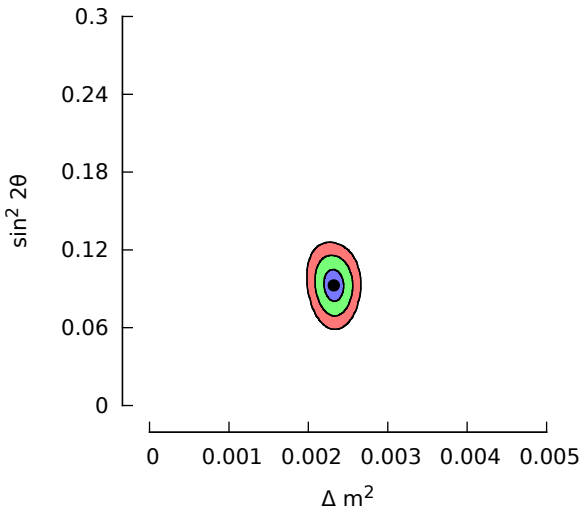

Figure 3.59: Simultaneous confidence regions for $\sin^2 2\theta$ and Δm^2 when the constraint on Δm^2 is taken into account.n The bands represent 1-, 2- and 3-σ confidence levels.

exactly consistent to what we have put into our code from the PDG:

$$\Delta m^2 = 0.002320 \pm 0.000100 \tag{3.47}$$

This is just an expression of the fact that our data are not sufficient to inform this measurement in any way. On the other hand, future shape analyses may have the ability to resolve the mass splitting with higher precision. Our fit for the mixing angle gives

$$\boxed{\sin^2 2\theta = 0.0926 \pm 0.0109} \tag{3.48}$$

a full 8.5 standard deviations from 0.

Pull Terms

In Table 3.20 above we showed the fits to the most interesting parameters with several combinations of the inputs fixed rather than allowed to vary in the minimization. We observed that fixing these numbers does not significantly impact the results for the parameters of interest Δm^2 or $\sin^2 2\theta$ nor for the normalization N. Along with the fitted backgrounds discussed above and listed in Table 3.18, the fitted efficiencies are listed in Table 3.21. We observe in all cases that the fitted value of the pull terms varies less than the nominal uncertainties. This suggests that the nominal uncertainties are overestimated.

Detector	Expected ε	Uncertainty	Fitted ε
AD1	1	0.002	1.0005
AD2	1	0.002	0.9996
AD3	1	0.002	0.9999
AD4	1	0.002	1.0004
AD5	1	0.002	1.0000
AD6	1	0.002	0.9996

Table 3.21: Fitted uncorrelated detector efficiencies.

To demonstrate the effect of these corrections, we fix the pull terms at their expected values rather than fitting for them. This corresponds to assuming that the backgrounds and efficiencies are known quantities, rather than having the distributions in Eq. 3.44. In this case, the error bars on $\sin^2 2\theta$ drop from ± 0.0109 to $^{+0.0100}_{-0.0101}$. This shows that the pull terms are a relatively small component of the overall uncertainty on $\sin^2 2\theta$.

In Table 3.22 we try to show the effect of changing these uncertainties. Increasing the uncertainties of the pulls brings down the χ^2, as one might predict since these uncertainties appear in the denominators of the various terms of Eq. 3.44. The effect is not as simple as decreasing the importance of the pulls while leaving the statistical component unchanged, however. Instead, smaller values of the uncertainties mean that greater weight is attached to the statistical component of the likelihood.

	Statistical	Pulls	Total χ^2
$\sigma/2$	3.72	0.22	3.94
σ	2.84	0.57	3.41
2σ	1.46	0.90	2.37

Table 3.22: Breakdown of the χ^2 into pulls and statistical components when the uncertainties σ_{B_d} and σ_{ε_d} are halved, kept at their nominal values, and doubled.

3.15 Conclusions

The current global picture of θ_{13} measurements is shown in Fig. 3.60. In the span of just one year, θ_{13} has gone from being the least known mixing angle to the best known mixing angle (in absolute terms). We have promised as a motivation for this work that it can help inform theoretical models such as supersymmetry and grand unified theories, and indeed already one sees a good deal of work from phenomenologists in response to the Daya Bay, RENO, and Double CHOOZ results.

Daya Bay has measured the last of the neutrino mixing angles, but several neutrino-related parameters still remain in the Standard Model. Of these, the CP phase can be probed by future long baseline experiments. The mass hierarchy remains an important unsolved problem, which long baseline reactor experiments may be able to address. The Daya Bay Collaboration has begun investigating a future Daya Bay II phase with much longer baselines and much larger target masses to address this question.

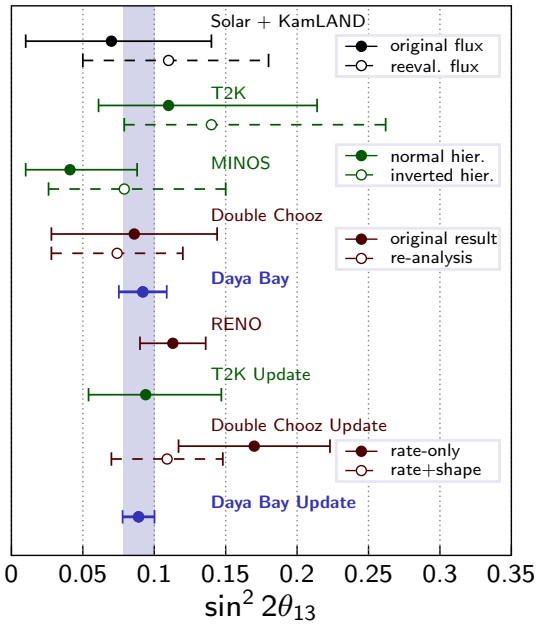

Figure 3.60: Results of numerous recent experiments for the θ_{13} neutrino mixing angle with the recently published Daya Bay result shown as the gray band [202].

References

[1] Daya Bay Technical Design Report.

[2] An, F. P., et al. "Observation of electron-antineutrino disappearance at Daya Bay." Physical Review Letters 108.17 (2012): 171803.

[3] Cowan Jr, C. L., et al. "Detection of the Free Neutrino: a Confirmation." Science (New York, NY) 124.3212 (1956): 103.

[4] Lee, T. D. "Parity Nonconservation and a Two-Component Theory of the Neutrino." Physical Review 105.5 (1957).

[5] Wu, C. S., et al. "Experimental test of parity conservation in beta decay." Phys. Rev 104 (1956): 1315.

[6] Danby, Gaillard, et al. "Observation of high-energy neutrino reactions and the existence of two kinds of neutrinos." Physical Review Letters 9.1 (1962): 36-44.

[7] Goldhaber, M., L. Grodzins, and A. W. Sunyar. "Helicity of neutrinos." Physical Review (US) Superseded in part by Phys. Rev. A, Phys. Rev. B: Solid State, Phys. Rev. C, and Phys. Rev. D 109 (1958).

[8] Litvinov, Yu A., et al. "Observation of non-exponential orbital electron capture decays of hydrogen-like¡ sup¿ 140¡/sup¿ Pr and¡ sup¿ 142¡/sup¿ Pm ions." Physics Letters B 664.3 (2008): 162-168.

[9] Kayser, Boris. "On the quantum mechanics of neutrino oscillation." Physical Review D 24.1 (1981): 110.

[10] Giunti, Carlo, Chung W. Kim, and U. W. Lee. "When do neutrinos really oscillate? Quantum mechanics of neutrino oscillations." Physical Review D 44.11 (1991): 3635.

[11] Grimus, W., and P. Stockinger. "Real oscillations of virtual neutrinos." Physical Review D 54.5 (1996): 3414.

[12] Hagiwara, Kaoru. "Review of particle physics." Physical Review D 66 (2002): 010001-974.

[13] Huang, Melin, et al. "Dependence of Neutrino Mixing Angles and CP-violating Phase on Mixing Matrix Parametrizations." arXiv preprint arXiv:1108.3906 (2011).

[14] Wolfenstein, Lincoln. "Neutrino oscillations in matter." Physical Review D 17.9 (1978): 2369.

[15] Abe, K., and T2K Collaboration. "Indication of Electron Neutrino Appearance from an Accelerator-produced Off-axis Muon Neutrino Beam,(2011)." arXiv preprint arXiv:1106.2822.

[16] Wingerter, Akın, C. Luhn, and K. Mohan Parattu. "A minimal model of neutrino flavor." Rencontres de Physique des Particules (RPP2012). 2012.

[17] Michael McFarlane. Email. July 15, 2012.

[18] Holzschuh, E., M. Fritschi, and W. Kündig. "Measurement of the electron neutrino mass from tritium beta-decay." Physics Letters B 287.4 (1992): 381-388.

[19] Franco, D., G. Consolati, and D. Trezzi. "Positronium signature in organic liquid scintillators for neutrino experiments." Physical Review C 83.1 (2011): 015504.

[20] Sears, Varley F. "Neutron scattering lengths and cross sections." Neutron news 3.3 (1992): 26-37.

[21] Vogel, P., and John F. Beacom. "Angular distribution of neutron inverse beta decay, $\nu_e^- + p \to e^+ + n$." Physical Review D 60.5 (1999): 053003.

[22] Lazauskas, R., P. Vogel, and C. Volpe. "Charged current cross section for massive cosmological neutrinos impinging on radioactive nuclei." Journal of Physics G: Nuclear and Particle Physics 35.2 (2007): 025001.

[23] Mention, G., et al. "Reactor antineutrino anomaly." Physical Review D 83.7 (2011): 073006.

[24] Boehm, F., et al. "Results from the Palo Verde neutrino oscillation experiment." Physical Review D 62.7 (2000): 072002.

[25] Michael, D. G., et al. "Observation of muon neutrino disappearance with the MINOS detectors in the NuMI neutrino beam." Physical review letters 97.19 (2006): 191801.

[26] Wang, Zhimin, et al. "Study of a prototype detector for the Daya Bay neutrino experiment." Nuclear Instruments and Methods in Physics Research Section A: Accelerators, Spectrometers, Detectors and Associated Equipment 602.2 (2009): 489-493.

[27] Collaboration, Daya Bay, et al. "A side-by-side comparison of Daya Bay antineutrino detectors." arXiv preprint arXiv:1202.6181 (2012).

[28] Guo, Xinheng. "A precision measurement of the neutrino mixing angle θ_{13} using reactor antineutrinos at Daya Bay." arXiv preprint hep-ex/0701029 61 (2007).

[29] Koblesky, T., et al. "Cathode position response of large-area photomultipliers under a magnetic field." Nuclear Instruments and Methods in Physics Research Section A: Accelerators, Spectrometers, Detectors and Associated Equipment (2011).

[30] Barrand, G., et al. "GAUDI—A software architecture and framework for building HEP data processing applications." Computer physics communications 140.1 (2001): 45-55.

[31] Bellamy, E. H., et al. "Absolute calibration and monitoring of a spectrometric channel using a photomultiplier." Nuclear Instruments and Methods in Physics Research Section A: Accelerators, Spectrometers, Detectors and Associated Equipment 339.3 (1994): 468-476.

[32] Birks, J.B. (1951). Proc. Phys. Soc. A64: 874.

[33] Wen, Liangjian, et al. "Maximum likelihood reconstruction of a detector with reflective panels." Nuclear Instruments and Methods in Physics Research Section A: Accelerators, Spectrometers, Detectors and Associated Equipment 629.1 (2011): 296-302.

[34] Hagner, Tanja, et al. "Muon-induced production of radioactive isotopes in scintillation detectors." Astroparticle Physics 14.1 (2000): 33-47.

[35] Zbiri, Karim. "Physics process of cosmogenics Li-9 and He-8 production on muons interactions with carbon target in liquid scintillator." arXiv preprint hep-ph/0607179 (2006).

[36] Mention, G. "Double-Chooz: a search for θ_{13}." Nuclear Physics B-Proceedings Supplements 145 (2005): 182-185.

[37] Mention, G., et al. "Reactor antineutrino anomaly." Physical Review D 83.7 (2011): 073006.

[38] Kopeikin, V. I., L. A. Mikaelyan, and V. V. Sinev. "Reactor as a source of antineutrinos: Thermal fission energy." Physics of Atomic Nuclei 67.10 (2004): 1892-1899.

[39] Neyman, Jerzy. "Contribution to the Theory of the χ^2 Test." Proceedings of the First Berkeley Symposium on Mathematical Statistics and Probability. August 13-18, 1945 and January 27-29, 1946. Statistical Laboratory of the University of California, Berkeley. Berkeley, Calif.: University of California Press, 1949. 501 pp. Editor: Jerzy Neyman, p. 239-273. Vol. 1. 1949.

[40] Jun Cao. DocDB 7637-1. Unblind the coordinates of ADs and cores.

[41] Fengpeng An. DocDB 7580-5. Reactor Neutrino Flux Prediction and Uncertainties.

[42] Zhe Wang. DocDB 4787-1. A few measurements about PMT and electronics.

[43] Feihong Zhang. DocDB 7554-3. H-Gd ratio study with spallation neutron.

[44] Chao Zhang. DocDB 7621-11. BCW Theta13 Oscillation Analysis (TechNote).

[45] Qing He. DocDB 4552-4. Li9, He8 generator.

[46] Karsten M. Heeger. DocDB 7212-2. Reactor Experiments and Future Neutrino Oscillation Measurements.

[47] Jun Cao. DocDB 181-1. Daya Bay Rock Analysis by P. Dobson.

[48] Wei Wang. DocDB 7809-3. Geometric effect due to finite-sized reactors and detectors.

[49] Lisa Whitehead. DocDB 3759-1. LS Attenuation Length and PE Yield.

[50] Ming Qi. DocDB 4128-1. Study of the UV-Vis light absorption and quality control of Linear Alkyl Benzene.

[51] Minfang Yeh. DocDB 3833-1. Densities of LAB, LS and GdLS.

[52] Jun Cao. DocDB 3728-1. PPO Purification and Mineral Oil Update.

[53] Yayun Ding. DocDB 3342-1. Gd-LS Dry Run.

[54] Jun Cao. DocDB 3790-1. Liquid Scintillator Status.

[55] Yayun Ding. DocDB 3284-1. Influence of Fe on Gd-LAB.

[56] Minfang Yeh. DocDB 3766-1. Radio-purification of GdCl3 for Daya Bay.

[57] Xiaobo Li. DocDB 4158-1. backgrounds due to radon in GdLS/LS and requriements of radon level.

[58] Beda Roskovec. DocDB 8141-1. Uniformity of Gd concentration.

[59] Dongmei Xia. DocDB 8033-3. preliminary study on the attenuation length monitoring for GdLS and LS.

[60] Michael McFarlane. DocDB 4382-1. AD Montoring Camera.

[61] Karsten M. Heeger. DocDB 443-4. Design of the Daya Bay Antineutrino Detector.

[62] Yifang Wang. DocDB 66-1. A detector design for the DayaBay reactor neutrino experiment.

[63] Liang Zhan. DocDB 22-1. Cylindrical Detector Concepts for Theta13 by S. Freedman.

[64] Ruiguang Wang. DocDB 7115-1. Fluorocarbon Paint on Daya Bay Antineutrino Detectors.

[65] Bryce Littlejohn. DocDB 2936-2. Degradation of Optical Properties of UVT Acrylic Optical Properties With UV Exposure.

[66] Bryce Littlejohn. DocDB 3533-1. Acrylic Density Measurement.

[67] Bryce Littlejohn. DocDB 3777-2. Acrylic Optical Properties and Simulations.

[68] Liang Zhan. DocDB 1010-1. Impact of Acrylic Vessel Thickness.

[69] Steve Virostek. DocDB 4168-8. Procedure of Installation of AD PMT Ladder.

[70] Steve Virostek. DocDB 4416-1. Error Analysis of AD PMT Positioning.

[71] Steve Virostek. DocDB 3075-1. AD PMT Radial Light Shield.

[72] Cheng-Ju Lin. DocDB 2267-1. Pros and Cons of implementing a diffuse radial reflector.

[73] Liangjian Wen. DocDB 2426-1. DayaBay Reflector Fabrication Plan.

[74] Wei Wang. DocDB 4678-2. AD lid sensor mounting schemes, cables and feedthroughs.

[75] Karsten M. Heeger. DocDB 3038-2. Introduction to calibration tubes & overflow tanks.

[76] David Jaffe. DocDB 1094-2. On the orientation of the near site antineutrino detectors.

[77] Robert D. McKeown. DocDB 270-1. A liquid scintillator veto system.

[78] Changgen Yang. DocDB 269-1. Water pool.

[79] Christopher White. DocDB 350-1. Specifications of PMT for the antineutrino detector.

[80] David Jaffe. DocDB 391-1. GEANT4 validation: Cherenkov photons in water.

[81] Vahe Ghazikhanian. DocDB 1620-1. PMT Test stand and procedures.

[82] Mary Stuart. DocDB 3592-1. Macro Potting Plan Update.

[83] Weili Zhong. DocDB 4752-1. Status of Macro PMT Potting at IHEP.

[84] Vahe Ghazikhanian. DocDB 1129-1. Earth's Magnetic field at Daya Bay.

[85] Kirk McDonald. DocDB 1298-2. Magnetic Fields Near the Welds of the MiniBooNE PMT Frames.

[86] Dawei Liu. DocDB 799-1. Earth Field Effects On PMT.

[87] KamBiu Luk. DocDB 794-1. Effect of Earth's Magnetic Field on Hamamatsu R5912 and ET 9353KB.

[88] Vahe Ghazikhanian. DocDB 1302-1. Calculation of Magnetic Field and Procedures to align PMTs to cancel the Transverse B field effects in AD.

[89] Dawei Liu. DocDB 1678-1. The Effects of Magnetic Field on PMT.

[90] Karsten M. Heeger. DocDB 2996-1. proposal for AD PMT magnetic shields.

[91] KamBiu Luk. DocDB 2004-3. Radial reflector and magnetic shield.

[92] S. Ryland Ely. DocDB 1168-4. 8" vs. 10" PMTs.

[93] Chris Polly. DocDB 2859-1. Scanner spot-size and 2d scans of DB5912 with Finemet.

[94] John Joseph. DocDB 2227-3. PMT High Voltage Decoupler Pulse Signal Splitter Specification.

[95] Dan Dwyer. DocDB 3081-1. Simulations of PMT and Electronics Effects.

[96] Zheng Wang. DocDB 1571-3. PMT FEE Board TDR version 2.

[97] Kirk McDonald. DocDB 1891-2. Comments on PMT Mounts.

[98] Jen-Chieh Peng. DocDB 2561-1. Some thoughts on PMT sample tests and sorting criteria.

[99] Cheng-Ju Lin. DocDB 2653-1. PMT sorting study.

[100] S. Ryland Ely. DocDB 4173-1. PMT Sorting.

[101] Jen-Chieh Peng. DocDB 2673-1. Minutes of PMT sorting phone discussion 9/10/08.

[102] Zheng Wang. DocDB 3652-2. FEE Design and Performance.

[103] John K.C. Leung. DocDB 2394-3. PDR Mineral oil monitoring.

[104] Xingtao Huang. DocDB 2367. DayaBay Framework and infrastructure.

[105] Ralph Brown. DocDB 801. Draft Engineering Drawing Control System.

[106] Charles Leggett. DocDB 1967. Re-introduction to Gaudi.

[107] Xingtao Huang. DocDB 3087. The Gaudi Framework.

[108] Brett Viren. DocDB 2942. Detector Simulation Lesson.

[109] Maxim Gonchar. DocDB 6062. Volume based photon weighting.

[110] Guofu Cao. DocDB 6580. IBD generator.

[111] Raymond Hei-Man Tsang. DocDB 5750. Generator for Gd Capture Gamma

[112] Liang Zhan. DocDB 1644. Orientation of sites for muon flux.

[113] Qun Wu. DocDB 1957. C++ wrapping of legacy fortran generators.

[114] Brett Viren. DocDB 3700. GenDecay: Data Driven, General Radioactive Decay Generator and GenTool.

[115] S. Ryland Ely. DocDB 1067. Progress on the He-8/Li-9 Generator.

[116] Viktor Pec. DocDB 3566. GtLiHeGen - Helium and Lithium generator.

[117] Qing He. DocDB 4074. Li9, He8 generator.

[118] Qing He. DocDB 4552. Li9, He8 generator.

[119] Soeren Jetter. DocDB 3239. Non-linear pmt effect in the electronics simulation.

[120] Dan Dwyer. DocDB 1775. Notes on Electronics and Trigger Simulation.

[121] Meng Wang. DocDB 2046. MC Mixing.

[122] Liang Zhan. DocDB 5962. Event rate for mixing.

[123] Mei Ye. DocDB 4035. DCS Draft List of Global Database Table.

[124] Meng Wang. DocDB 1564. A proposal for a realistic MC sample.

[125] Haoqi Lu. DocDB 5711. The proposal of Fast MC Production(FMCP).

[126] Jiaheng Zou. DocDB 7151. NtupleAna - a Lightweight Analysis Framework.

[127] Zhimin Wang. DocDB 6971. Configuration for 3halls stable data taking.

[128] Jianglai Liu. DocDB 7222. EH1 production good files: version 2.

[129] Fei Li. DocDB 2841. The raw event format in the Daya Bay DAQ.

[130] Fei Li. DocDB 3442. The raw data file format in the Daya Bay DAQ.

[131] Simon Patton. DocDB 2696. SPADE - An Introduction.

[132] Craig E. Tull. DocDB 3031. Data Movement Model.

[133] Zeyuan Yu. DocDB 6926. What Hits to utilize?

[134] Zhe Wang. DocDB 5063. A Heads-up for Dry Run Data Analysis.

[135] J. Pedro Ochoa. DocDB 5091. Pedestal stability.

[136] Soeren Jetter. DocDB 5374. Baseline Distortion: Impact on IBD Events.

[137] Zhe Wang. DocDB 5958. 5kHz noise and impact on PreAdc (pedestal)

[138] Cheng-Ju Lin. DocDB 5728. Preliminary ADC Charge Bias Studies.

[139] S. Ryland Ely. DocDB 5967. Correction of Pre-ADC Bias.

[140] Cheng-Ju Lin. DocDB 6006. FEE Shaped Pulse Parametrization.

[141] Qing He. DocDB 5361. Fitting single photo-electron peak.

[142] Qing He. DocDB 5323. Rolling Gain & Dark noise.

[143] Qing He. DocDB 6039. Dark hit vs. Low intensity LED run.

[144] Jen-Chieh Peng. DocDB 5429. How well do we need to calibrate the PMT gains?

[145] Jen-Chieh Peng. DocDB 5448. PMT threshold and linearity of energy response.

[146] Jiajie Ling. DocDB 5746. Relative Timing Calibration.

[147] S. Ryland Ely. DocDB 3525. A Deterministic Code for Calculating the AD Light Response.

[148] Kirk McDonald. DocDB 3829. RPC Module Signal and HV Connections.

[149] Weili Zhong. DocDB 1999. Measurement of quenching factor of liquid scintillator.

[150] Patrick K.V. Tsang. DocDB 7240. Energy Scale from Spallation Neutron.

[151] Dan Dwyer. DocDB 7390. Comments on Current AD Energy Reconstruction.

[152] Liang Zhan. DocDB 7314. Anti-neutrino Detector Energy Response (TechNote).

[153] Zeyuan Yu. DocDB 7418. Energy calibration and reconstruction (AdScaled).

[154] Yasuhiro Nakajima. DocDB 7239. Vertex reconstruction using charge templates.

[155] Yasuhiro Nakajima. DocDB 7423. Vertex reconstruction using charge template.

[156] Raymond Hei-Man Tsang. DocDB 6991-4. Modeling AD singles spectrum.

[157] Zhimin Wang. DocDB 6491-1. EH#1 300kHz noise source and AD#1 light tight check.

[158] Fenfang Wu. DocDB 7552-2. Estimatation of Uncertainties for Singles Rate, DMC efficiency, Accidental Rate.

[159] Fenfang Wu. DocDB 7336-1. EH1 Single Rate Investigation.

[160] Dawei Liu. DocDB 6347-2. Understanding EH-1 Muon Pool PMT Singles Rates.

[161] Dawei Liu. DocDB 6526-2. Understanding EH-1 Muon Pool PMT Singles Rates (II).

[162] Wah-Kai Ngai. DocDB 7457-2. EH1 Analysis: Muon Lifetime Measurement.

[163] Meng Wang. DocDB 2326-2. The muon in ADs.

[164] Haoqi Lu. DocDB 7641-1. WaterPool-Efficiency.pdf.

[165] Lingyu Wang. DocDB 7838-9. Muon Track Reconstruction(TechNote).

[166] Jilei Xu. DocDB 4649. Propose a method to measure muon charge ratio.

[167] David Jaffe. DocDB 2232. Physics with stopping muons in Daya Bay.

[168] Viktor Pec. DocDB 1767. Simulation of Stopping Muons.

[169] DocDB 8142.

[170] Herb Steiner. DocDB 6968-1. Lab Study of Flasher PMTs: SD-0150, SD-0191, SD-1639, SD-1640.

[171] Miao He. DocDB 6956-2. Production discussion.

[172] Xin Qian. DocDB 6976-1. A second look of flashers.

[173] Liangjian Wen. DocDB 7143-3. Full control of the flashers.

[174] Zeyuan Yu. DocDB 5939-3. Research on Double Neutron Backgrounds .

[175] S. Ryland Ely. DocDB 4928-1. Neutron Capture Time.

[176] Yasuhiro Nakajima. DocDB 7522-1. Study of energy scale difference between IBD and spallation neutron samples.

[177] Xin Qian. DocDB 7526-3. Investigation of Shoulder in Spallation Neutron capture time.

[178] Yasuhiro Nakajima. DocDB 7661-1. 6MeV cut uncertainties for IBD and spallation neutrons.

[179] Xin Qian. DocDB 7290-4. Quick Study of Fast Neutrons.

[180] Haoqi Lu. DocDB 7605-5. Fast nentron background(TechNote).

[181] Liangjian Wen. DocDB 7616-2. Anti-neutrinos detection for theta13 analysis (TechNote).

[182] Miao He. DocDB 7622-5. Determine accidental background by off-window method.

[183] Chao Zhang. DocDB 7309-3. Accidentals Distribution In IBD Candidates.

[184] Wei Wang. DocDB 7673-1. Accidental rates and reactor power.

[185] Chao Zhang. DocDB 7947-1. Updates On Accidentals.

[186] S. Ryland Ely. DocDB 1067-2. Progress on the He-8/Li-9 Generator.

[187] Viktor Pec. DocDB 5285-4. 9Li/8He genrator updates.

[188] Yiming Zhang. DocDB 7970-2. Summary on Li-9 Daily Yield Calculation with 2.2MeV Signal.

[189] Yiming Zhang. DocDB 7903-1. Li-9 Daily Yield Calculation with 2.2MeV Signal.

[190] Wenqiang Gu. DocDB 6779-3. AmC background note.

[191] Wenqiang Gu. DocDB 6291-4. AmC Neutron Background Simulation Update.

[192] Wenqiang Gu. DocDB 8059-3. ACUC AmC Run Quick Look.

[193] Xiaohui Chen. DocDB 7978-4. AmC Background Study.

[194] Fenfang Wu. DocDB 7568-1. Estimation of Correlated Bg from ACUs.

[195] Zeyuan Yu. DocDB 7971-1. Update alpha-n background.

[196] Zeyuan Yu. DocDB 7509-4. Alpha-n background study.

[197] Yasuhiro Nakajima. DocDB 8727-2. How to define Delta m$\hat{2}$_ee.

[198] Wei Wang. DocDB 7654-3. Cross check the IBD cross sections used by different groups.

[199] David Webber. DocDB 7081. Target Protons Uncertainties Slides.

[200] Christine Lewis. DocDB 7714. Unblinded AD1-6 Target Masses.

[201] Minfang Yeh. DocDB 6615-3. Daya_Bay_Liquid analysis_V3.

[202] Steve Kettell. DocDB 8718-2. Global Comparison of theta_13 Measurements.